PL-TR-92-3043 AD-A262 785 PL-TR-92-3043 (2)

ENGINEERING CONSIDERATION FOR THE SELF-ENERGIZING MAGNETOPLASMADYNAMIC (MPD)-TYPE FUSION PLASMA THRUSTER

DTIC
S ELECTE D
MAR 1 2 1993
C

Professor Chan K. Choi
Glen T. Nakafuji

Purdue University
School of Nuclear Engineering
West Lafayette, IN 47907-1290

February 1993

Annual Report

APPROVED FOR PUBLIC RELEASE; DISTRIBUTION UNLIMITED.

93-05215

93 3 11 046

PHILLIPS LABORATORY
Propulsion Directorate
AIR FORCE MATERIEL COMMAND
EDWARDS AIR FORCE BASE CA 93524-7001

NOTICE

When U.S. Government drawings, specifications, or other data are used for any purpose other than a definitely related Government procurement operation, the fact that the Government may have formulated, furnished, or in any way supplied the said drawings, specifications, or other data, is not to be regarded by implication or otherwise, or in any way licensing the holder or any other person or corporation, or conveying any rights or permission to manufacture, use or sell any patented invention that may be related thereto.

FOREWORD

This report was prepared by School of Nuclear Engineering, Purdue University, under contract F04611-90-K-0054, for Operating Location AC, Phillips Laboratory, Edwards AFB, CA. 93524-7001. Project Manager for Phillips Laboratory was Frank Mead.

This report has been reviewed and is approved for release and distribution in accordance with the distribution statement on the cover and on the SF Form 298.

Franklin B. Mead
FRANK B. MEAD
Project Manager

Stephen L. Rodgers
STEPHEN L. RODGERS
Chief, Emerging Technologies Branch

LEONARD C. BROLINE, Lt Col, USAF
Director,
Fundamental Technologies Division

RANNEY G. ADAMS
Public Affairs Director

Accesion For
NTIS CRA&I ☑
DTIC TAB ☐
Unannounced ☐
Justification
By
Distribution /
Availability Codes
Dist | Avail and / or Special
A-1

REPORT DOCUMENTATION PAGE

Form Approved
OMB No. 0704-0188

Public reporting burden for this collection of information is estimated to average 1 hour per response, including the time for reviewing instructions, searching existing data sources, gathering and maintaining the data needed, and completing and reviewing the collection of information. Send comments regarding this burden estimate or any other aspect of this collection of information, including suggestions for reducing this burden, to Washington Headquarters Services, Directorate for Information Operations and Reports, 1215 Jefferson Davis Highway, Suite 1204, Arlington, VA 22202-4302, and to the Office of Management and Budget, Paperwork Reduction Project (0704-0188), Washington, DC 20503.

1. AGENCY USE ONLY (Leave blank)	2. REPORT DATE	3. REPORT TYPE AND DATES COVERED
	February 1993	Annual July 1991 - June 1992

4. TITLE AND SUBTITLE
Engineering Consideration for the Self-Energizing Magnetoplasmadynamic (MPD) - Type Fusion Plasma Thruster

5. FUNDING NUMBERS
C: F04611-90-K0054
PE: 62302F
PR: 3058
TA: 00AF

6. AUTHOR(S)
Professor Chan K. Choi
Glen T. Nakafuji

7. PERFORMING ORGANIZATION NAME(S) AND ADDRESS(ES)
Purdue University
School of Nuclear Engineering
West Lafayette, IN 47907-1290

8. PERFORMING ORGANIZATION REPORT NUMBER
PL-PU/92003

9. SPONSORING/MONITORING AGENCY NAME(S) AND ADDRESS(ES)
Phillips Laboratory
OLAC-pL/RKFE
Edwards AFB, CA 93524-7680

10. SPONSORING/MONITORING AGENCY REPORT NUMBER
PL-TR-92-3043

11. SUPPLEMENTARY NOTES
COSATI CODE: 21/03

12a. DISTRIBUTION/AVAILABILITY STATEMENT
Approved for Public Release, Distribution is Unlimited

12b. DISTRIBUTION CODE

13. ABSTRACT (Maximum 200 words)

The major objective of the present study is to perform parametric studies of various DPF electrode configurations using an equivalent circuit model. The operation of the DPF device in the current-rise state is modelled using a transient code simulation of the equivalent circuit. Parametric studies of four DPF electrode configurations which include the tapered, cylindrical anode tip of the Livermore-I experiment, the anode tip with an equilateral triangular shape, the extended triangular anode tip, and the untapered cylindrical anode tip have all been performed. Besides the various geometrical shapes, the electrode configurations also depend very sensitively on the dimension of the anode length. The parametric studies indicated that both the equilateral triangular tip and the cylindrical tip configurations generated high sheath currents and F/W values while maintaining relatively similar values of I_{sp} for all electrode configurations. The extended triangular tip geometry, however, performed less favorably to F/W values and the sheath currents, though the differences compared to the values of other geometries were not very significant. It is thus noted that adequate operating currents can be reached by optimizing the electrode geometry and the charging circuit voltage and that the equivalent circuit modelling provides a realistic basis for analyzing plasma focus pinch dynamics.

14. SUBJECT TERMS
Fusion Propulsion, Dense Plasma Focus, Magnetoplasmadynamic Thruster, Equivalent Circuit Model, Advanced Fuel ($D-^3He$) Fusion

15. NUMBER OF PAGES

16. PRICE CODE

17. SECURITY CLASSIFICATION OF REPORT	18. SECURITY CLASSIFICATION OF THIS PAGE	19. SECURITY CLASSIFICATION OF ABSTRACT	20. LIMITATION OF ABSTRACT
Unclassified	Unclassified	Unclassified	SAR

NSN 7540-01-280-5500

Standard Form 298 (Rev. 2-89)
Prescribed by ANSI Std. Z39-18
298-102

TABLE OF CONTENTS

SECTION Page

INTRODUCTION 1

MODELING OF THE DENSE PLASMA FOCUS (DPF) 9

Equivalent Circuit 9
Companion Circuit Model 10
Development of Transient Circuit Code 12
Initial Testing of Transient Circuit Code 15
Plasma Dynamics 22
Simulation of the Livermore-I Experiment 28

PARAMETRIC STUDY OF THE DPF ELECTRODES 34

Introduction 34
Radial Variation of Anode 34
Variations of Electrode Length and Charging Voltage 35

DENSE PLASMA FOCUS PROPULSION SYSTEM 42

Introduction 42
Rocket Dynamics 42
Fusion Principles 43
Brief Description of DPF Propulsion System 45
Performance Results with Modified Electrode Configurations 49

CONCLUSION AND RECOMMENDATIONS 58

LIST OF REFERENCES 62

APPENDIX A 65

APPENDIX B 83

LIST OF FIGURES

Figure Page

1. Diagram of Dense Plasma Focus Device 2
2. Operational Phases of Dense Plasma Focus 4
3. Equivalent Circuit Model for Dense Plasma Focus 9
4. Trapezoidal Approximation of Waveform 11
5. Equivalent Companion Circuits 11
6. Equivalent Circuit for $0 < t < t_{max}$ 13
7. Equivalent Circuit for $t > t_{max}$ 14
8. The 7x7 System of Equations for Equivalent Circuit at $0 < t < t_{max}$ 16
9. The 9x9 System of Equations for Equivalent Circuit at $t > t_{max}$ 17
10. Flow Chart of Transient Code 18
11. Current Plot for Test Circuit using SPICE and LU Solver 20
12. Percent Error between SPICE and LU Solutions 20
13. Percent Error between LU and Analytical Solutions 21
14. Calculated Load Currents for Circuit with, and without Crowbar 21
15. The Anode Profile for the Livermore-I Device 30
16. Experimental and Calculated Current Histories for the Livermore-I Experiment 30
17. Calculated Plasma Sheath Inductance for the Livermore-I Experiment 31
18. Calculated Axial Rundown Velocity for the Livermore-I Experiment 32
19. Calculated Node Voltage Across the Plasma Sheath 33

Figure Page

20. The Anode Variation Profiles 36

21. Sheath Current Histories for Anode Variation Tests 37

22. Inductance Curves for Anode Variation Tests 38

23. Anode/Cathode Gap Voltages for Anode Variation Tests 39

24. Axial Rundown Velocities for Anode Variation Tests 40

25. System Diagram for Dense Plasma Focus Thruster 47

26. Specific Impulse vs. Propellant Mass Flow Rate (Δv = 5 km/s) 52

27. Thrust-to-Weight Ratio vs. Propellant Mass Flow Rate (Δv = 5 km/s) 53

28. Specific Impulse vs. Propellant Mass Flow Rate (Δv = 20 km/s) 54

29. Thrust-to-Weight Ratio vs. Propellant Mass Flow Rate (Δv = 20 km/s) 55

30. Specific Impulse vs. Propellant Mass Flow Rate (Δv = 40 km/s) 56

31. Thrust-to-Weight Ratio vs. Propellant Mass Flow Rate (Δv = 40 km/s) 57

A.1. Livermore-I Plasma Focus Electrode Geometry 66

A.2. Sheath Current Histories for Anode Variation Tests (same as Figure 3.2) 67

A.3. Thrust-to-Weight Ratios for Enhanced and Livermore-I Electrode (Δv=5km/s) (same as Figure 4.3) 68

A.4. Specific Impulse for Enhanced and Livermore-I Electrode (Δv=5km/s) (same as Figure 4.2) 69

A.5. Equilateral Anode Tip 70

A.6. Optimized Current Histories for Equilateral Anode Tip 71

A.7. Thrust-to-Weight Ratios for Equilateral Anode Tip and Livermore-I Electrode (Δv=5km/s) 72

Figure Page

A.8. Specific Impulse for Equilateral Anode Tip and Livermore-I Electrode (Δv=5km/s) 73

A.9. Cylindrical Anode Tip 74

A.10. Optimized Current Histories for Cylindrical Anode Tip 75

A.11. Thrust-to-Weight Ratios for Cylindrical Anode Tip and Livermore-I Electrode (Δv=5km/s) 76

A.12. Specific Impulse for Cylindrical Anode Tip and Livermore-I Electrode (Δv=5km/s) 77

A.13. Extended Triangular Anode Tip 78

A.14. Optimized Current Histories for Extended Triangular Tip Anode 79

A.15. Thrust-to-Weight Ratios for Extended Triangular Anode and Livermore-I Electrode (Δv=5km/s) 80

A.16. Specific Impulse for Extended Triangular Anode Tip and Livermore-I Electrode (Δv=5km/s) 81

A.17. Capacitor Energy Discharge Curve 82

LIST OF TABLES

Table Page

1. Comparison of Parameters between Static Testing Circuit and the Livermore-I Experiment 15

2. Input Parameters for the Livermore-I Plasma Focus Experiment 29

3. Optimized Parameters for High Current Delivery 41

4. Propulsion Parameters for Base Case (Δv=10km/s, I=20MA) 51

INTRODUCTION

The purpose of this research is to investigate the effects of various electrode configurations on the performance of the DPF. These studies focus on the sensitivity of the current, density and temperature of the plasma to different electrode geometries. A modularized version of a DPF code[1] previously used to evaluate the system performance of a D-^{3}He fueled device will be utilized for parametric studies in this work.

The dense plasma focus is composed of a coaxial electrode set connected to a high voltage, high current switching circuit (Figure 1). The electrodes consist of a cylindrical cathode surrounding a rod shaped anode which forms an annular gap between the oppositely polarized surfaces. One end of the device is blocked off by the fuel injection apparatus and insulating material needed to isolate the cathode from the anode. This axial type of coaxial geometry is referred to as the Mather-type electrode configuration, while another type of DPF electrode geometry is known as the Fillipov configuration. The Mather device accelerates a plasma sheath axially down the annular region of the electrodes while a Fillipov device accelerates a plasma sheath in a radial direction[2]. This research will be limited to studying the Mather type of electrode configuration for space propulsion applications.

The DPF's coaxial geometry is similar to other advanced propulsion devices like the magnetoplasmadynamic(MPD) and arcjet thrusters. However, the MPD and arcjet do not utilize fusion power to generate thrust, and they rely instead on expanding gas for propulsive power. The DPF's dependence on fusion power requires operational currents that are far in excess of the current required by the MPD or arcjet. Another difference is that the DPF is not operated in a steady state mode, rather it is a pulsed power device.

The principal operation of the DPF is fairly straightforward; fusion fuel is first injected into the annulus between both electrodes and an arc is established across the fuel filled gap. This arc ionizes the fuel and forms a plasma sheath which propagates down the annulus and runs out the end of the device. As the outer rim of the sheath detaches from the cylindrical cathode, magnetohydrodynamic instabilities cause the sheath to collapse in on itself thereby forming a small, hot, highly dense volume of plasma. It is in this region that the fusion reactions occur, which liberate the necessary energy used for thrust.

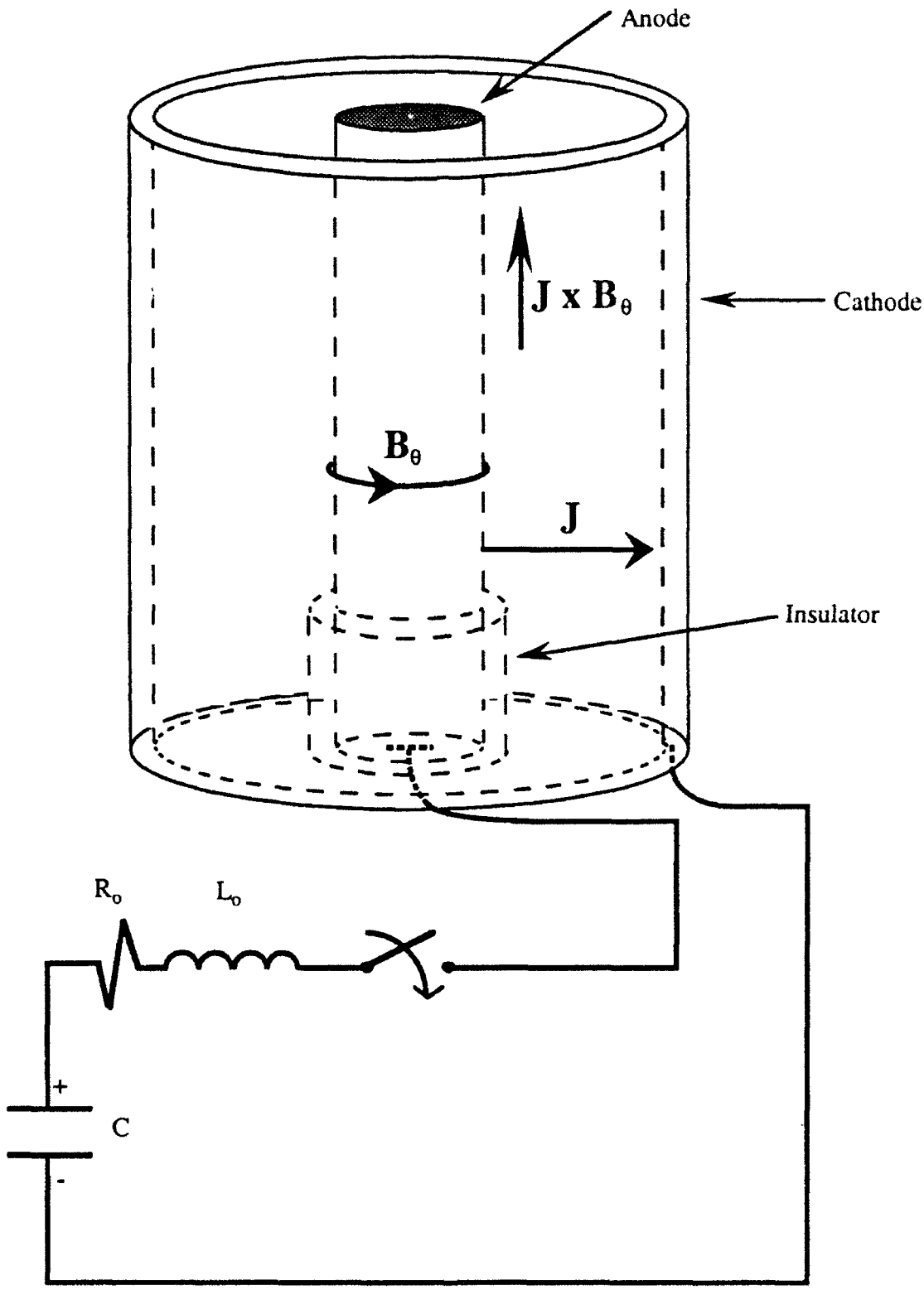

Figure 1
Diagram of Dense Plasma Focus Device

The operational cycle of the DPF can be broken down into several distinct phases as illustrated in Figure 2.

1. Breakdown phase - Gaseous fuel is injected into the annular region prior to arc initiation. Capacitor bank is discharged across electrodes and initiates symmetrical arc between cathode cylinder and anode bar. Fill gas is ionized during breakdown and plasma sheath is formed.
2. Rundown phase - Arc current induces azimuthal magnetic field B_θ around the anode bar. The J x B_θ force accelerates plasma sheath down the length of the anode. A fraction of the fill gas is entrained by the propagating plasma sheath.
3. Pinch phase - Plasma sheath reaches the end of the electrodes and the J x B_θ force initiates the radial compression of the sheath. Collapsing sheath focuses towards the central axis of the anode forming a hot, high density plasma where fusion reactions are to take place.

After the pinch is formed, it is vulnerable to various types of plasma instabilities which will distort and eventually disrupt the pinch region due to MHD instabilities. These instabilities include both the m = 0 "sausage" and m = 1 "kink" instabilities. The disruption of the pinch region marks the end of one cycle of the DPF operation, and this cycle is designed to be repeated providing a "continuous" mode of firing.

Advanced propulsion technology development began in the 1950's with the development of nuclear and ion propulsion systems. These concepts came under scrutiny because of the potential advantages over chemical rocket concepts[3,4]. Advanced concepts relying on nuclear, ion, and magnetoplasmadynamic schemes could provide the increase in thrust and specific impulse necessary for manned interplanetary travel.

Nuclear propulsion offers much more energy per unit mass than conventional chemical rocket concepts. Chemical rockets are limited by the chemical bond energy of the fuel, whereas nuclear rockets rely on fission energy. This available nuclear energy far exceeds that produced by even the most energetic chemical rocket fuels. Project Rover[5] was one of the first studies to examine the feasibility of nuclear rocket propulsion. Thrust for the nuclear rocket is produced by heating propellant in a heat-exchanger reactor and exhausting the hot gas through a nozzle. Generally, hydrogen is the propellant of choice because of it's low molecular weight. The rocket itself consists of a solid core reactor with numerous flow channels to accommodate the passage of propellant through the core. The Rover project was concerned with producing roughly twice the specific impulse of the most efficient chemical rocket, as well as providing greater thrust for an increased payload. Open air tests were conducted with the Kiwi-A device in 1959-60, and it concluded with

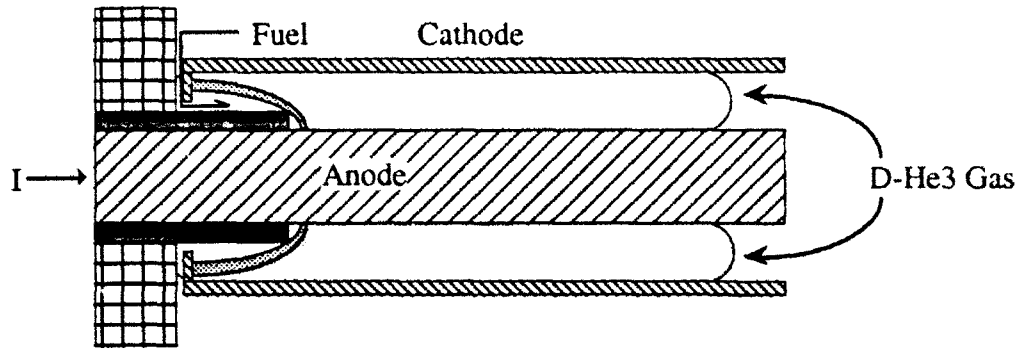

Breakdown Phase

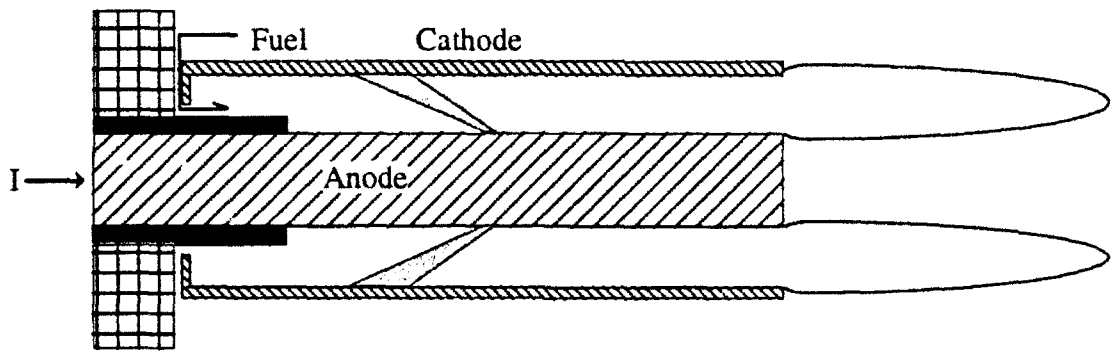

Rundown Phase

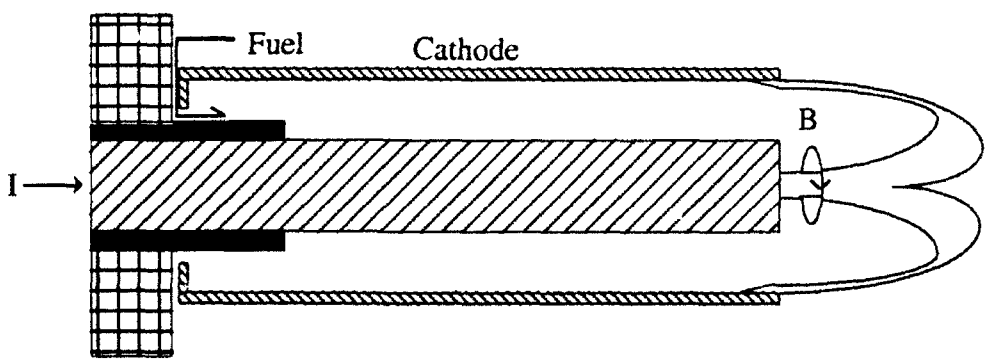

Pinch Phase

Figure 2
Operational Phases of Dense Plasma Focus

the recommendation of further study into nuclear propulsion. Another nuclear rocket project that followed in the footsteps of the Rover project was the NERVA project. The goal of the NERVA project was to produce a solid core powered nuclear propulsion system that would be capable of the high specific impulse needed for interplanetary travel. The NERVA research began in the 1960's, but fell victim to funding cuts in the early 1970's.

Ion propulsion is another advanced concept that was theoretically predicted to be superior to chemical propulsion. Ion rockets rely on the electrostatic acceleration of ions for thrust[4]. An ion rocket is a form of electric propulsion and therefore requires a power source to produce ions and generate the electrostatic field used to accelerate them. Ion propulsion performance exceeds that of the nuclear rocket in terms of travel time and specific impulse, but it lacks the thrust to weight capacity of nuclear and chemical systems. Consequently, an ion propulsion system must first be placed in orbit before it can engaged.

Magneto-plasmadynamic(MPD) thrusters are a form of electrical propulsion that can provide performance similar to ion powered devices. MPD type thrusters utilize a current and magnetic field to produce an electromagnetic(JxB) force that is used to accelerate a highly ionized fuel. These thrusters basically consist of an cathode and anode, either in a parallel rail or coaxial electrode configuration, and a power supply. Operation of this type of thruster is similar to that of the DPF which is described in the previous section. One of the major differences between the MPD and the DPF is that the DPF electrode polarity is reversed from the MPD electrode polarity. The arcjet which is currently under research at the NASA Lewis Center belongs to this family of electric thruster.

One alternative concept that has not been examined as extensively as the previously mentioned schemes is fusion propulsion. Fusion propulsion relies on the enormous amounts of energy produced in thermonuclear reactions to produce thrust. Theoretical studies have been conducted on different fusion propulsion schemes based on inertial and magnetic confinement concepts[6,7]. The Air Force has undertaken a study involving the dense plasma focus device and its application to space propulsion. The feasibility of designing and operating such a system is being researched at the Phillips Laboratory in New Mexico and Purdue University. The adaptation of the dense plasma focus device for space propulsion involves an increased current and material requirement that is essential for operation. Operating currents on the order of tens of mega amperes must be applied in order to achieve a fusion reaction with a D-^{3}He fueled device. The current capability of the source circuit as well as the durability of electrode and insulator material represent major engineering limitations. The physics of the pinch dynamics, and the scaling laws relating plasma temperature and capacitor mass to external current are

additional problems which require further research, but are beyond the scope of the current study.

Several plasma focus devices have been constructed and tested at various research institutions around the world[8]. The Livermore-I experiment which forms the basis of this study is a 1.2 MA device that was used to conduct studies into the rundown, collapse and pinch phases of operation. Other devices include the Frascati plasma focus in Italy which operated at a peak current of 2.8 MA, and the Poseidon plasma focus device in Stuttgart Germany which reached a maximum current of 4.9 MA[9]. These devices used annealed copper electrodes and pyrex or ceramic insulators. These materials help determine a failure limit for the current generation of devices. In order to achieve ignition, a D-^{3}He fueled device should be supplied with a total input current in the 10-20 MA range[1]. This limit far exceeds the capacity of any existing plasma focus device. However, the SHIVA implosion experiment at the Air Force Weapons research lab[10] reached a peak operating current of approximately 12.3 MA. This experiment establishes a precedent for very high current capability for a pulsed power system application. The SHIVA experiment relied on a 120 kV, 9.4-MJ capacitor bank to supply the necessary current to drive a dynamic coaxial vacuum inductive store. This system was used to supply a current pulse to a cylindrical implosion load.

The dense plasma focus has been the subject of numerous studies since its inception in the 1960's, and the majority of these studies have been conducted on the plasma pinch phenomena and neutron production mechanisms[11,12]. Parametric studies have been conducted with the goal of optimizing the circuit parameters and filling pressure to maximize the temperature and density of the pinch region[13]. Variation of electrode configuration and the consequent effect on the pinch have not been as extensively studied as other plasma focus phenomena.

The electrode configuration plays a key role in the formation of the plasma pinch region. Geometry and sizing of the electrodes affect the density, dynamic inductance, and therefore the current of the propagating plasma sheath. The characteristics of the current pulse can be used to determine the electrode length in order to ensure that maximum current is reached at the end of the acceleration phase[13]. Experimentation with various plasma focus devices such as the Livermore-I experiment has yielded information about the current history of the propagating plasma sheath. Subsequent studies have dealt with the presence of a leakage current that occurs over the surface of the insulator during operation[8]. This leakage current degrades the performance of the focus for operating currents in the MA range. The high operating current range also has an effect on the

insulator surface over which the initial breakdown arc occurs[14]. In a 22 kV, 1-kJ Mather-type plasma focus, the pyrex insulator used suffered surface alterations and metallic deposition due to the temperature in the plasma sheath. The device utilized brass electrodes and reached a peak current of approximately 0.1 MA. After successive firings of the device, varying stages of insulator erosion were observed. This degradation is indicative of the susceptibility of the insulator to very high operating currents and is a key factor in determining the limiting performance of upscaled models of very high current devices.

Various models have been used to predict current histories and sheath velocities in the rundown phase of operation. Different studies have utilized various modeling techniques for the plasma focus rundown, including an equivalent circuit representation[8,15], and two-dimensional MHD calculations. The equivalent circuit models provide a simpler model which couples electrical circuit equations to dynamic sheath parameters while the MHD codes use a two-fluid model with two dimensional effects included[16,17]. Both methods can be used to predict the behavior of the rundown phase up to the collapse region, but MHD theory breaks down after the collapse since it cannot predict the pinch formation, dimension and the current behavior in the pinch region.

This work is being conducted in order to establish the feasibility of the dense plasma focus as a viable space propulsion concept. The enormous potential of fusion power in this application is explored for the dense plasma focus device. To achieve a good fusion burn during the pinch phase, currents on the order of 20 MA must be supplied to the device. Present plasma focus experiments deal with sheath currents that are only in the 1 - 4 MA range. Therefore, a realistic model must be developed for the upscaled parameters of a dense plasma focus system that operates in the very high current regime.

In order to accurately account for the physics of the breakdown and the rundown phases of operation, a one-dimensional transient simulator code will be developed for integration with a previously developed code for the pinch phase of the plasma focus[1]. This model will be based on an equivalent circuit representation of the dense plasma focus device. Various features will be incorporated into the code to account for certain phenomena that have been experimentally observed. A leakage current branch in the equivalent circuit is used to provide a realistic loss component to the transient code. The current of the plasma sheath prior to the pinch phase ideally should be at a maximum in order to optimize conditions for a fusion reaction to take place. In order to reduce the current damping during operation, a crowbar switch was also added to the equivalent circuit. The equivalent circuit is reduced to a system of equations which is solved using LU decomposition. An objective will be to link the electrical performance of the device to

the plasma modeling of the sheath. The Snowplow model is utilized to calculate rundown velocity and the mass of fill gas entrained in the propagating sheath. The dynamic sheath inductance and resistance predicted by the Snowplow model is coupled to the equivalent circuit system of equations. This approach provides a realistic means of predicting plasma focus performance in the 20 MA current range. Calculations will then be carried out on different electrode geometries with the goal of obtaining a more accurate representation of the performance envelope of the dense plasma focus.

MODELING OF THE DENSE PLASMA FOCUS (DPF)

Equivalent Circuit

The dense plasma focus device can be modeled using an equivalent circuit representation. The model shown in Figure 3 displays the circuit parameters for the discharge circuit and the plasma sheath. The values C, L_O and R_O are the external capacitance, inductance and resistance, respectively. The dynamic inductance and resistance of the plasma sheath are represented by L_{PF} and R_{PF}.

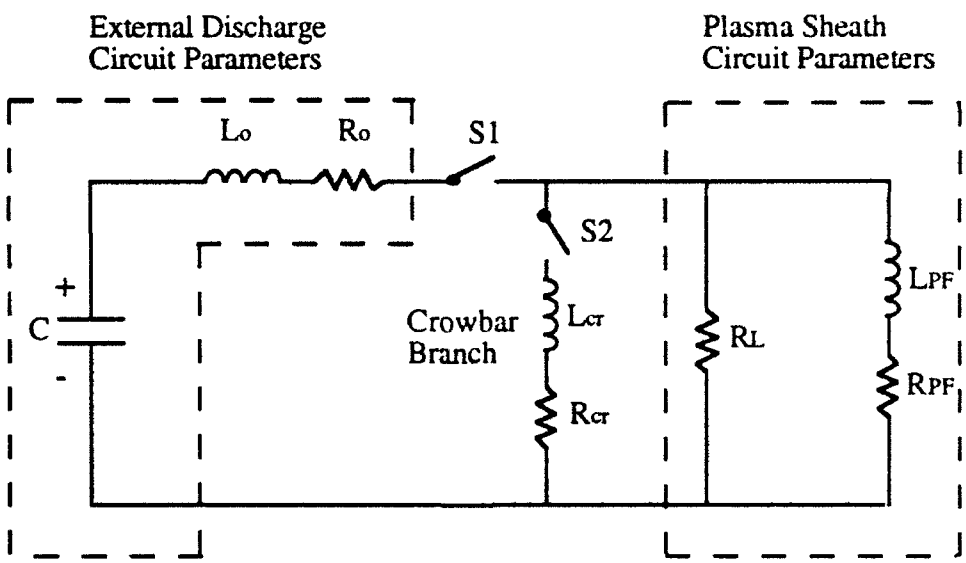

Figure 3
Equivalent Circuit Model for Dense Plasma Focus

The resistance R_L that is included in the sheath parameters depicts the leakage current around the insulator that occurs during the rundown phase. The leakage current results from the formation of an arc across the insulator surface, and is responsible for reducing the actual current delivered to the plasma sheath. R_{cr} and L_{cr} are the components of the

crowbar switch of the circuit. The crowbar switch is designed to reduce the fast damping of the current that occurs during the capacitor discharge.

At time $t = 0^-$, switches S1 and S2 are open, then S1 is closed at $t = 0$ and the capacitor begins discharging. When the current reaches its maximum value at $t = t_{max}$, S2 is closed to reduce the damping effect. The values of the circuit parameters can be chosen to provide either an underdamped, overdamped, or critically damped transient response. For this work, the external circuit parameters will remain fixed while the crowbar values and the sheath values will be optimized in order to provide maximum current delivery to the sheath.

Companion Circuit Model

The modeling of the reactive elements in the circuit is done using the companion circuit model. In the companion circuit model, both the inductors and capacitors in a circuit can be reduced to an equivalent or "companion" representation. This is accomplished by making use of the basic voltage and current relations for the inductor and capacitor.

$$V = L\frac{dI}{dt}, \tag{1}$$

and

$$I = C\frac{dV}{dt}. \tag{2}$$

Both relations are evaluated as integrals with respect to time.

$$I = \frac{1}{L}\int_{t1}^{t2} V\,dt\ , \tag{3}$$

and

$$V = \frac{1}{C}\int_{t1}^{t2} I\,dt\ . \tag{4}$$

The solution to these integral equations can be obtained by using a trapezoidal approximation for either the voltage or current waveform as illustrated in Figure 4.

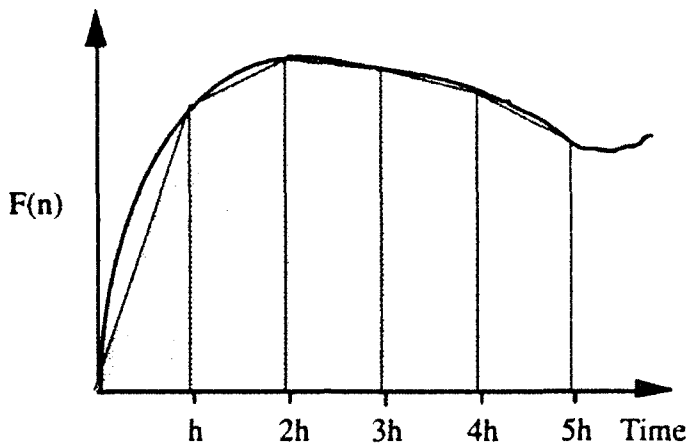

Figure 4
Trapezoidal Approximation of Waveform

The value of the function F(n) can be ascertained by summing the values of each trapezoidal panel over a specified number of time steps(n). Equation 5 denotes the value of a single trapezoidal panel for a single time step h.

$$\Delta I = 0.5\ h\ (F(n) + F(n+1)). \tag{5}$$

Usage of the trapezoidal rule allows the inductor and capacitor to be reduced to the companion models[18] shown in Figure 5.

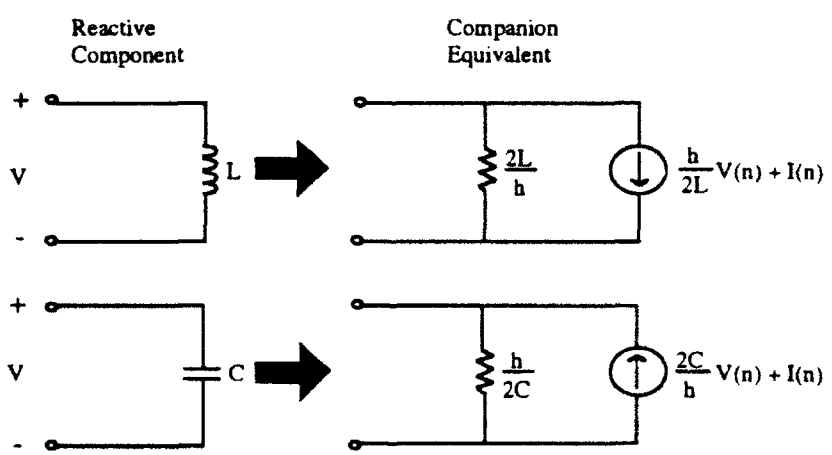

Figure 5
Equivalent Companion Circuits

These models form the basis of the governing equations for the inductor and capacitor, with the (n+1) terms representing the new time values and the (n) terms representing the old time forcing function values.

and
$$I(n+1) = \frac{h}{2L} V(n+1) + \frac{h}{2L} V(n) + I(n) \ , \tag{6}$$

$$V(n+1) = \frac{h}{2C} I(n+1) + \frac{h}{2C} I(n) + V(n) \ . \tag{7}$$

Development of Transient Circuit Code

Development of a transient code was deemed necessary in order to model the electrical and plasma dynamic characteristics of the dense plasma focus. In the transient code, the dynamic physics of the sheath are coupled with the plasma inductance and current response of the equivalent circuit. This coupling allows the device to be modeled by a modified transient circuit solver.

The equivalent circuit can be reduced to a system of equations represented by

$$\mathbf{I} = \mathbf{YV}, \tag{8}$$

where **I** is the current vector, **Y** is the conductance matrix and **V** is the voltage vector. The Y matrix is formed using the conductances of the resistors and the trapezoidal approximation to model the reactive elements of the circuit. Once the Y matrix is formed, the initial conditions are input into the I vector, then the system is solved using LU decomposition. The Y matrix and I vector are updated every time step to account for the dynamically changing inductance and resistance of the sheath. Each new time current is used to calculate a new rundown velocity as well as a new sheath inductance, resistance and temperature. This calculation is marched through time until the sheath reaches the end of the device, then the end values of the current, rundown velocity and plasma temperature are passed to another code which calculates the pinch phase dynamics.

The operational cycle of the rundown phase can be described by two distinct circuits, one without the crowbar for $0 < t < t_{max}$(Figure 6), and the other with the crowbar

switched in for time $t > t_{max}$(Figure 7) These two circuits will yield conductance matrices of differing sizes and it is desirable to keep them segregated to allow for ease of calculation.

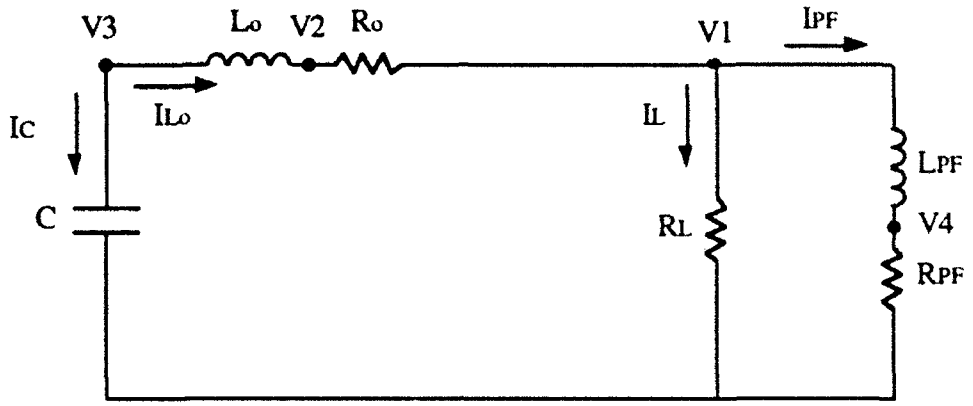

Figure 6
Equivalent Circuit for $0 < t < t_{max}$

The circuit for $0 < t < t_{max}$ is reduced to a system of equations by summing the currents into each node.

$$\frac{V_1 - V_2}{R_o} + \frac{V_1}{R_L} + I_{PF} = 0 , \tag{9}$$

$$-I_{Lo} + \frac{V_2 - V_1}{R_o} = 0 , \tag{10}$$

$$I_C + I_{Lo} = 0 , \tag{11}$$

and

$$-I_{PF} + \frac{V_4}{R_{PF}} = 0 . \tag{12}$$

This system is augmented by an additional number of equations, each representing the companion circuit model of a reactive element.

$$I_C(n) + \frac{2C}{h} V_3(n) = \frac{2C}{h} V_3(n+1) - I_C(n+1) , \tag{13}$$

and $$-\frac{h}{2L_o}(V_3(n)-V_2(n)) - I_{Lo}(n) = \frac{h}{2L_o}(V_3(n+1) - V_2(n+1)) - I_{Lo}(n+1) . \quad (14)$$

The resultant matrix that is formed by both these sets of equations is used for calculating the new time currents and voltages in the circuit by LU decomposition.

Once the crowbar branch of the circuit is switched in at $t > t_{max}$, a new conductance matrix must be formed to account for the modified circuit. The equivalent circuit with the crowbar switched in is displayed in Figure 7.

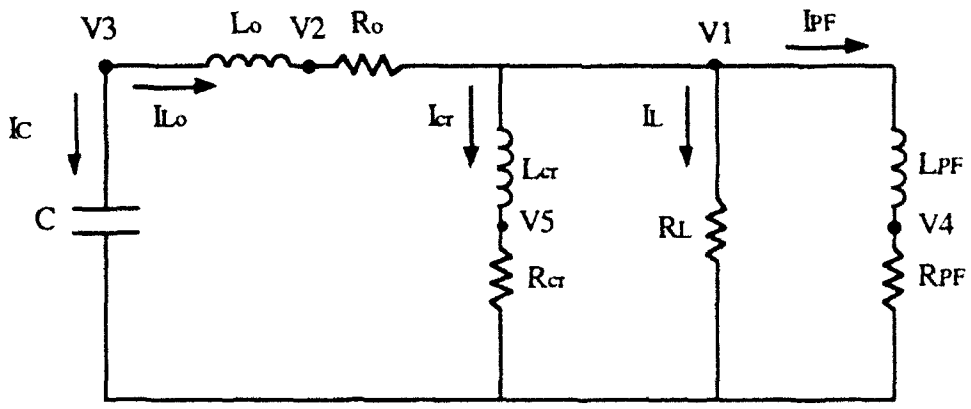

Figure 7
Equivalent Circuit for $t > t_{max}$

Switching the crowbar into the circuit introduces one extra node and 2 extra elements to the basic equivalent circuit. Two extra nodal equations and the additional crowbar current are added to the previous set formulated for the basic equivalent circuit without the crowbar.

$$-I_{Lcr} + \frac{V_5}{R_c} = 0 , \quad (15)$$

and $$I_{Lcr}(n+1) = \frac{h}{2L_{cr}}(V_1(n+1) - V_5(n+1)) + \frac{h}{2L_{cr}}(V_1(n) - V_5(n)) + I_{Lcr}(n) . \quad (16)$$

These additional nodal equations allow the previous 7x7 system (Figure 8) of equations to be increased to a 9x9 system (Figure 9).

These matrices were integrated into a transient code developed specifically for the rundown phase of the dense plasma focus. Initial conditions are read from an input deck and the appropriate arrays are initialized. The code is first run through the problem with the mode flag set equal to 3. This indicates that the code is checking for the time that peak pinch current is reached in the equivalent circuit without the crowbar. Once the code cycles through this check mode, the time that peak current is reached (t_{max}) is stored and the flag is reset to 1 and the problem is restarted. The flag remains set at 1 until t_{max} is reached, then the crowbar is switched in and the flag is set to 2. The calculation is now marched through time until the propagating plasma sheath reaches the end of the anode.

This code tracks the electrical and plasma parameters of the device through the duration of the rundown phase. As mentioned earlier, the 7x7 matrix is used before the plasma current has reached its peak, and the 9x9 matrix is used after peak current has been reached and the crowbar has been switched in. During each time step the matrix is initialized and solved by LU decomposition, and the new time values are used to calculate a new sheath inductance, rundown velocity, plasma temperature and plasma resistance. These values are recycled back to initialize the matrix for the next time step and the process repeats itself until the sheath runs off the tip of the anode. A flow chart depicting the order of operation in the transient code is displayed in Figure 10.

Initial Testing of Transient Circuit Code

The validity of the transient LU solver was established by running a test case for a circuit with static parameters and contrasting the calculated results with the analytical solution and output from SPICE. The SPICE (Simulation Program with Integrated Circuit Emphasis) program[19] is a circuit simulator that was developed for various types of circuit analysis, including linear ac, nonlinear transient and nonlinear dc analysis.

The test circuit was patterned after the equivalent circuit displayed in Figure 6. Circuit parameter values were set to provide as close a resemblance to the Livermore I parameters as possible. Table 1 shows the various parameters for Livermore I and the static test circuit used.

Table 1. Comparison of Parameters between Static Testing Circuit and the Livermore-I Experiment

DEVICE	C (F)	V_0 (V)	R_0 (Ω)	L_0 (H)	R_L (Ω)	R_{PF} (Ω)	L_{PF} (H)
Livermore-I	3.55E-4	27000	.005	2.5E-8	.12	dynamic	dynamic
Testing Circuit	3.55E-4	27000	.005	2.5E-8	.12	1.0E-7	1.0E-8

$$
\begin{vmatrix}
0 \\
0 \\
0 \\
0 \\
I_C(n) + \frac{2C}{h} V_3(n) \\
-\frac{h}{2L_o}(V_3(n) - V_2(n)) - I_{L,o}(n) \\
-\frac{h}{2L_{pf}}(V_1(n) - V_4(n)) - I_{L,pf}(n)
\end{vmatrix}
=
\begin{vmatrix}
\frac{1}{R_o} + \frac{1}{R_L} & -\frac{1}{R_o} & 0 & 0 & 0 & 0 & 1 \\
-\frac{1}{R_o} & \frac{1}{R_o} & 0 & 0 & 0 & -1 & 0 \\
0 & 0 & 0 & 0 & 1 & 1 & 0 \\
0 & 0 & 0 & \frac{1}{R_{PF}} & 0 & 0 & -1 \\
0 & 0 & \frac{2C}{h} & 0 & -1 & 0 & 0 \\
0 & -\frac{h}{2L_o} & \frac{h}{2L_o} & 0 & 0 & -1 & 0 \\
\frac{h}{2L_{pf}} & 0 & 0 & -\frac{h}{2L_{pf}} & 0 & 0 & -1
\end{vmatrix}
\begin{vmatrix}
V_1 \\
V_2 \\
V_3 \\
V_4 \\
I_C \\
I_{Lo} \\
I_{Lpf}
\end{vmatrix}
$$

Figure 8
The 7x7 System of Equations for the Equivalent Circuit at $0 < t < t_{max}$

$$
\begin{vmatrix} 0 \\ 0 \\ 0 \\ 0 \\ 0 \\ I_C(n) + \frac{2C}{h} V_3(n) \\ -\frac{h}{2L_o}(V_3(n) - V_2(n)) - I_{Lo}(n) \\ -\frac{h}{2L_c}(V_1(n) - V_5(n)) - I_{Lc}(n) \\ -\frac{h}{2L_{pf}}(V_1(n) - V_4(n)) - I_{Lpf}(n) \end{vmatrix}
=
\begin{vmatrix}
\frac{1}{R_o} + \frac{1}{R_L} & -\frac{1}{R_o} & 0 & 0 & 0 & 0 & 0 & 1 & 1 \\
-\frac{1}{R_o} & \frac{1}{R_o} & 0 & 0 & 0 & 0 & -1 & 0 & 0 \\
0 & 0 & 0 & 0 & 0 & 1 & 1 & 0 & 0 \\
0 & 0 & 0 & \frac{1}{R_{PF}} & 0 & 0 & 0 & 0 & -1 \\
0 & 0 & 0 & 0 & \frac{1}{R_c} & 0 & 0 & -1 & 0 \\
0 & 0 & \frac{2C}{h} & 0 & 0 & -1 & 0 & 0 & 0 \\
0 & -\frac{h}{2L_o} & \frac{h}{2L_o} & 0 & 0 & 0 & -1 & 0 & 0 \\
\frac{h}{2L_c} & 0 & 0 & 0 & -\frac{h}{2L_c} & 0 & 0 & -1 & 0 \\
\frac{h}{2L_{pf}} & 0 & 0 & -\frac{h}{2L_{pf}} & 0 & 0 & 0 & 0 & -1
\end{vmatrix}
\begin{vmatrix} V_1 \\ V_2 \\ V_3 \\ V_4 \\ V_5 \\ I_C \\ I_{Lo} \\ I_{Lc} \\ I_{Lpf} \end{vmatrix}
$$

Figure 9
The 9x9 System of Equations for the Equivalent Circuit at $t > t_{max}$

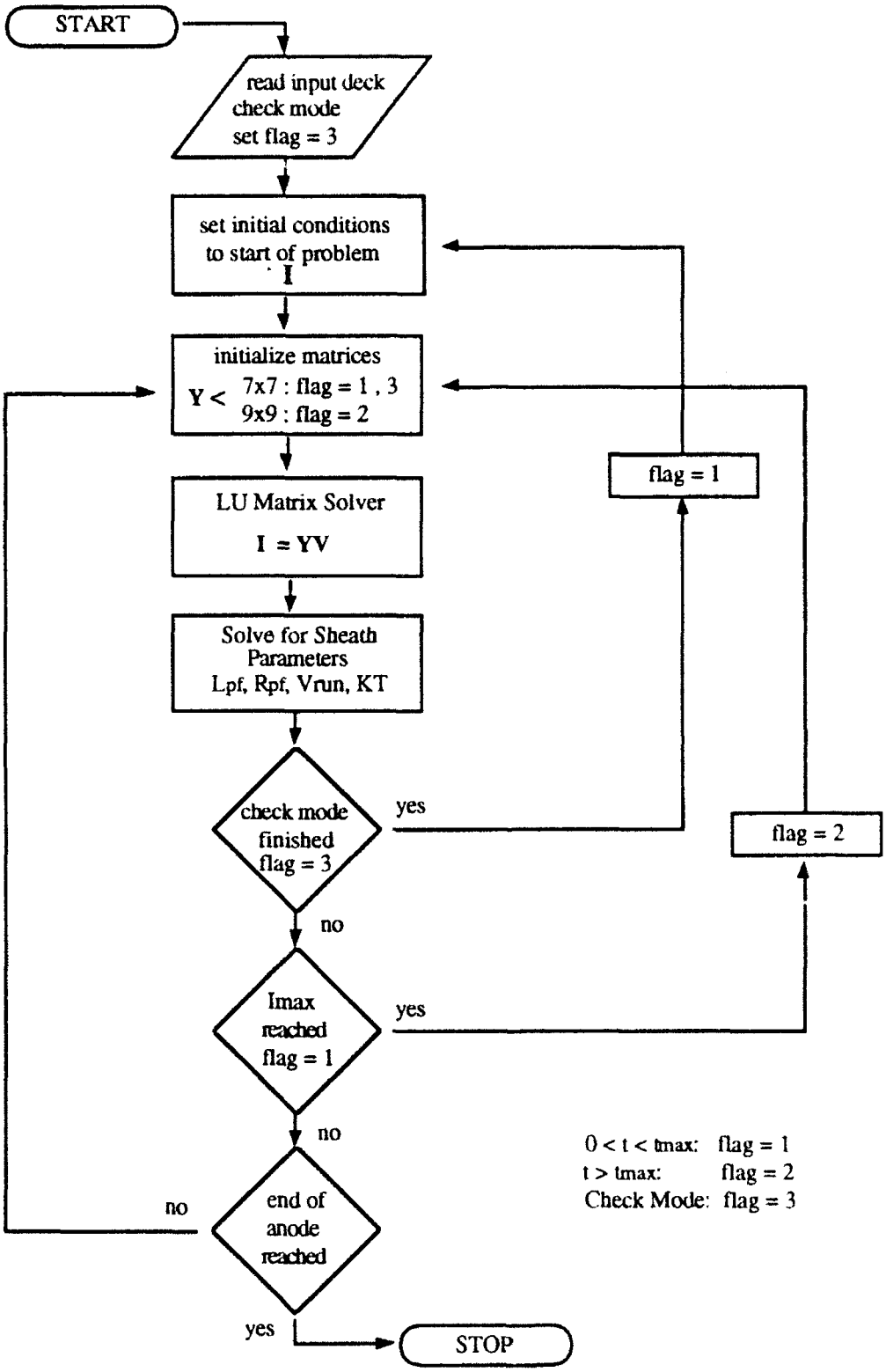

Figure 10
Flow Chart of Transient Code

The results from the test runs on the static circuit are displayed in the following graphs. Figure 11 shows the dual plot of load current for both SPICE and LU calculated solutions. It is apparent that the overlay of both plots make them virtually indistinguishable from each other. The relative error between the two calculations is shown in Figure 12. There is excellent agreement between SPICE and the LU calculated solutions (note that the percent error is normalized for the SPICE calculation). The oscillating nature of the relative error is thought to be due to perturbations in the SPICE calculated result. The next graph (Figure 13) shows the relative error between the LU calculation and an analytical solution that was derived using Laplace Transformations and Kirchoff's Voltage Law. Again there is excellent agreement between the LU calculation and the analytical solution and there is no evidence of the oscillation present in the Figure 12. An actual graph between the analytical value and the LU solution was omitted since the curves cannot be distinguished from each other.

The crowbar switch was a feature that was added to the transient code in order to reduce the damping of current in the response. The switching in of the crowbar branch increases the effective decay constant of the current response, thus keeping the current as high as possible for as long as possible. The effectiveness of the crowbar is determined by the choice of crowbar inductance and resistance. The maximum effect can be achieved when the crowbar parameters are of the same order of magnitude as the sheath parameters. A test case with the crowbar switched in was run and contrasted with the results from a case run without the crowbar. Figure 14 displays both plots and it should be noted that the curve for the crowbar is for the median case when the crowbar and load impedances are identical.

The effect of the crowbar that is evident in Figure 14 suggests that the addition of a crowbar switch would be beneficial to the maximization of current delivered to a load. There are however some engineering concerns that may limit the usage of the crowbar for plasma driven devices. One concern is that in order to maximize the effect of the crowbar, the crowbar resistance and inductance must be of the same order of magnitude as that of the load. In devices that utilize a body of plasma as the load, the resistance and inductance are typically very small values, and it may be hard to produce an adequate crowbar switch which would significantly decrease damping. This switch would also have to be durable enough to withstand flow currents in the 10^6 ampere range. Assuming that these problems can be resolved, the crowbar switch could prove to be very beneficial to peak current stabilization in the dense plasma focus.

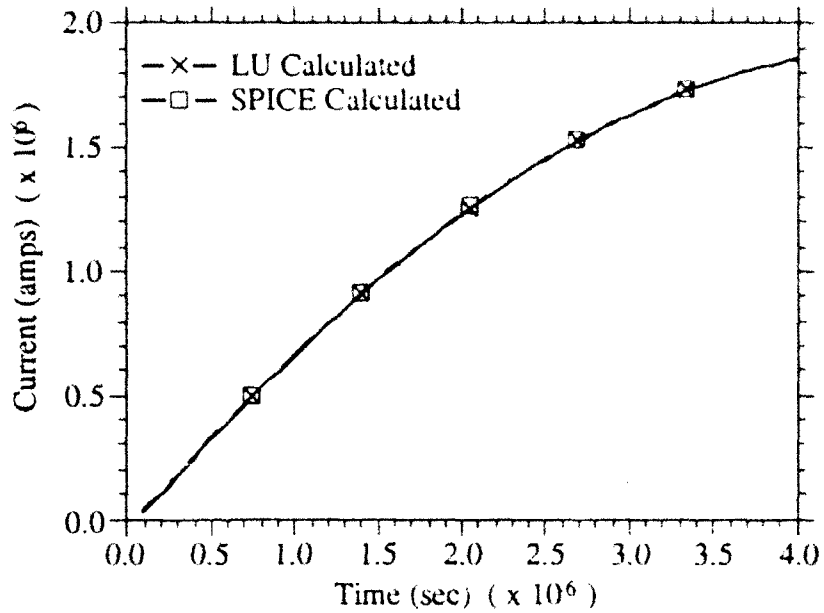

Figure 11
Current Plot for Test Circuit using SPICE and LU Solver

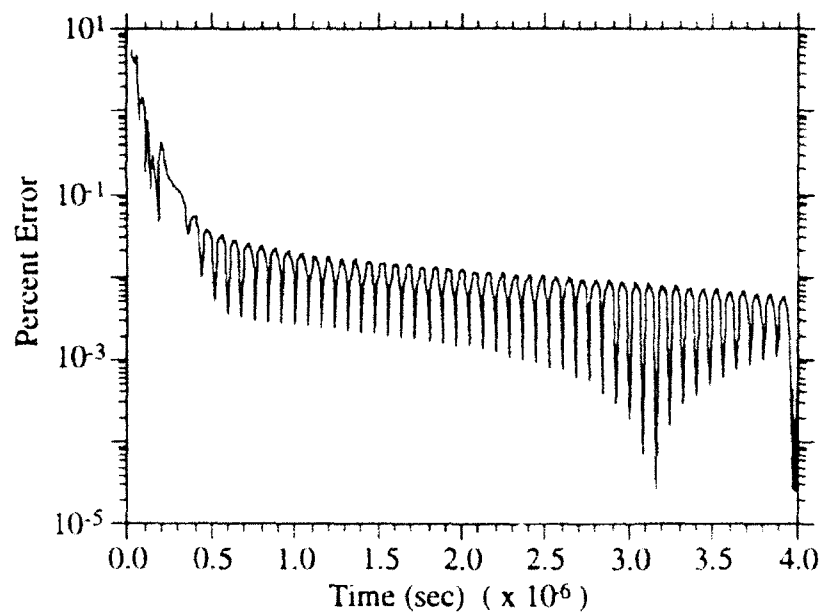

Figure 12
Percent Error between SPICE and LU Solutions

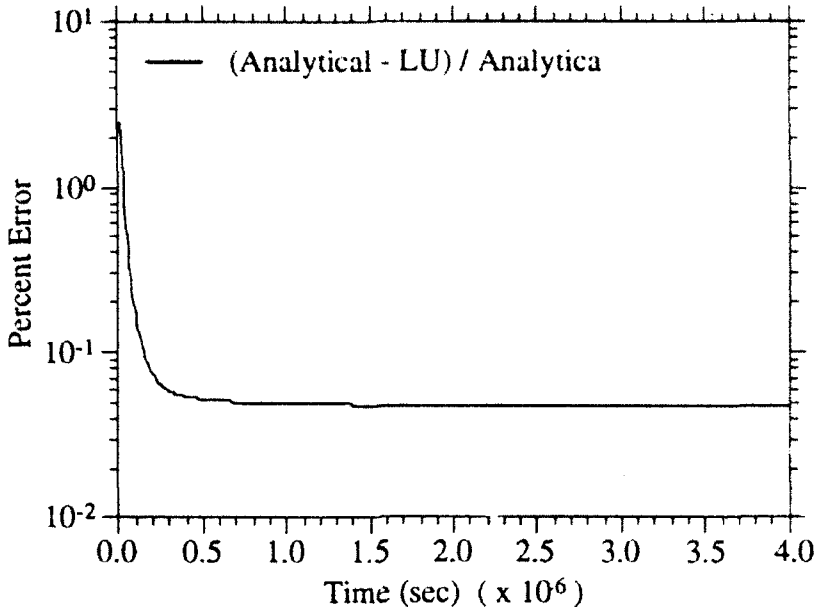

Figure 13
Percent Error between LU and Analytical Solutions

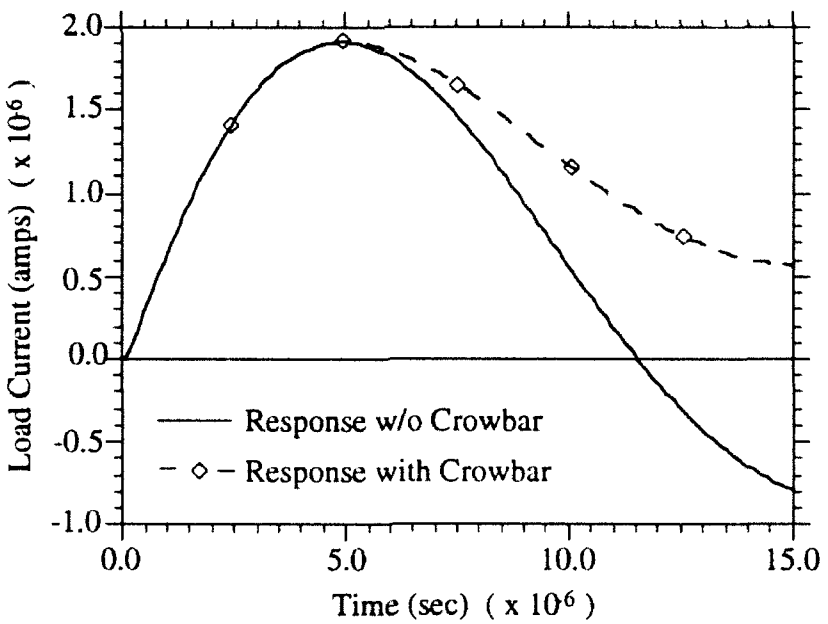

Figure 14
Calculated Load Currents for Circuit with, and without Crowbar.

Plasma Dynamics

The dynamic quantities associated with the propagating plasma sheath in the DPF device are the sheath inductance, resistance, temperature and rundown velocity. Relations for these quantities allow the dynamics of the plasma sheath to be coupled to the equivalent circuit model. The snowplow model [20] is used to calculate rundown velocity in the transient code. This model is used to account for the mass entrainment of the fill gas as the plasma sheath propagates down the anode. The simple MHD model does not take this entrainment effect into account and is perhaps too ideal for a realistic calculation.

The snowplow model assumes that the plasma sheath is an impermeable surface that absorbs fill gas as it propagates down the electrode annulus. Any mass that the arc surface encounters as it sweeps down the anode is absorbed into the sheath. The snowplow model can be expressed using Newton's law of motion in which the time rate change of momentum is equal to the sum of forces acting on a body. The limitation of the snowplow model is that it assumes total mass entrainment which does not totally reflect the physical nature of the sheath during rundown. One expects that while the majority of the fill gas is swept into the sheath, there is a certain fraction that is not entrained during rundown. This difference does not provide a significant discrepancy in the calculated results for the Livermore-I plasma focus test case that is shown later in this text. Starting with the general momentum equation:

$$\frac{\partial \rho \vec{v}}{\partial t} + \nabla \cdot (\rho \vec{v} \vec{v}) = -\nabla p - \nabla \cdot \tau + \rho g, \tag{17}$$

where ρ is the initial fill gas density and v is the velocity. The wall shear and body force terms are neglected under the assumption that the magnetic pressure is the primary driving force. By taking only the axial components and integrating over the constant volume of the sheath during rundown, a general expression for the momentum balance can be obtained

$$\frac{d}{dt}(m \dot{z}) = F_{total} \tag{18}$$

where the left hand side of the equation is the total derivative representation of the time dependent and convective momentum terms. The total force term on the right hand side of Equation (18) includes magnetic force on the sheath, particle pressure of the plasma and the frictional force on the plasma mass. The frictional force is negligible in comparison to the

magnetic force and particle pressure. The particle pressure will be treated later in the text when the liftoff current is calculated. The magnetic force is expressed by the equation of the electromagnetic force density integrated over the volume of the sheath,

$$\vec{F}_{mag} = \int_{Vol} \vec{j} \times \vec{B} \, d\tau \, . \tag{19}$$

The work done by the propagating plasma sheath as it advances a distance z down the anode is expressed by the next equation,

$$W = \int_0^z \vec{F}_{mag} \, d\vec{z} \, . \tag{20}$$

Assuming that all of the inductive energy (including energy stored in the field) of the plasma sheath is going into driving the plasma, the following expressions can be obtained:

$$W_{ind} = \frac{1}{2} L I^2 \, , \tag{21}$$

$$W = W_{ind} \, , \tag{22}$$

$$F_{mag} = \frac{1}{2} \frac{L I^2}{z} \, . \tag{23}$$

Expanding the left hand side of Newton's law (Equation (18)) and substituting the force term with Equation (21) gives the following relation.

$$m\ddot{z} + \dot{m}\dot{z} = \frac{1}{2} \frac{L}{z} I^2 \tag{24}$$

In this expression the first term on the left hand side of the equation is the conventional acceleration term, while the second term designates the mass accumulation of the sheath.

The plasma sheath initially has some small mass m_0 associated with it at the beginning of the breakdown phase. The initial mass quantity is dependent on the sheath thickness and length at the initiation of the arc sheet. Once the sheath starts propagating down the device, the mass accumulation rate is determined by the rundown velocity, gas

density and the dimensions of the annular channel. An assumption is made that the gas density is uniform throughout the transient. The total mass term m can be expressed as follows:

$$m = m_o + \text{Area} \int_0^t \rho \frac{dz}{dt} dt \,. \tag{25}$$

where $$\text{Area} = \pi \left(r_c^2 - r_a^2\right) . \tag{26}$$

The area is calculated for the annular dimensions of the electrodes with the final mass expression with ρ being constant

$$m = m_o + \pi \left(r_c^2 - r_a^2\right) \rho \, z(t) \tag{27}$$

Newton's law can be also be expressed in the following reduced form

$$\frac{d}{dt}\left[m(t)\, \dot{z}(t)\right] = \frac{1}{2} \frac{L(t)}{z} \, I^2(t) \,. \tag{28}$$

Integrating with respect to time gives

$$m\dot{z} = \frac{1}{2} \int_0^t \frac{L(t)\, I^2(t)\, dt}{z(t)} \,. \tag{29}$$

Now we have an expression for the rundown velocity which accounts for mass entrainment in the sheath.

$$\dot{z} = \frac{1}{2\,m} \int_0^t \frac{L(t)\, I^2(t)\, dt}{z(t)} \,. \tag{30}$$

This expression is implemented numerically in the transient code using the trapezoidal rule to approximate the product of L and I^2 at each discrete time step. This gives a new time rundown velocity which is used to calculate the axial position of the sheath during the rundown phase. The dynamic inductance of the sheath is dependent on the positional tracking of the arc.

This dynamic inductance expressed as L_{PF} in the equivalent circuit is dependent on the axial position z as well as the distance between cathode and anode. Utilizing Faraday's law of induction for a single-turn current carrying coil, one obtains the following expressions:

$$\Phi = L\,I\,, \tag{31}$$

where

$$\Phi = \int_{r_a}^{r_c} B_\theta\, z\, dr\,, \tag{32}$$

and

$$B_\theta = \frac{\mu_o\, I}{2\pi r} \tag{33}$$

Combining the previous equations will give a general solution of the sheath inductance for the device.

$$L(t) = \frac{\mu_o\, z}{2\,\pi} \ln\left(\frac{r_c}{r_a}\right) \tag{34}$$

This general inductance is adjusted by adding an extra term that accounts for the inductance due to the radial liftoff of the plasma sheath from the insulator.

$$L_{PF}(t) = \frac{\mu_o}{2\,\pi} \ln\left(\frac{r_c}{r_a}\right)\left[z(t) + z_{lo}\right]. \tag{35}$$

The time dependent z(t) term in the brackets represents the inductance over the anode, while the z_{lo} term is the contribution of the sheath inductance over the insulator region during the radial liftoff of the plasma sheath. The term z(t) is the time dependent location of the

leading edge of the current sheath while the term z_{lo} is the length of the insulator and thus a fixed quantity. The z_{lo} contribution to the inductance describes the initial inductance before the plasma sheath lifts off from the insulator and starts to propagate down the device. From this total expression for the sheath inductance, the initial sheath inductance $L_{PF}(t = 0)$ can be found as

$$L_{PF}(t = 0) = \frac{\mu_o}{2\pi} \ln\left(\frac{r_c}{r_a}\right)[\Delta + z_{lo}] . \tag{36}$$

At time zero the time dependent expression z(t) can be replaced by the sheath thickness Δ which is assumed to be 0.2 cm in the transient code.

The plasma resistance, R_{PF}, is dependent on the temperature as well as the density of the sheath. The resistance is derived by finding the electric field between the anode and cathode surfaces using Gauss's law:

$$\int \vec{E} \cdot \vec{dS} = \frac{Q}{\varepsilon_o} , \tag{37}$$

with

$$|\vec{E}| = \frac{Q}{2\pi\, r\, z\, \varepsilon_o} . \tag{38}$$

The next step is to utilize Ohm's law and the expression for the current through the plasma sheath

$$R = \frac{V}{I} , \tag{39}$$

where

$$V = \int |\vec{E}|\, dr = |\vec{E}|\, r \ln\left(\frac{r_c}{r_a}\right) , \tag{40}$$

$$I = \int j \cdot dS = j\, 2\pi\, r\, \Delta . \tag{41}$$

Combining these three equations and solving for the resistance give the final expression for resistance as

$$R_{PF} = \frac{\eta \ln\left(\frac{r_c}{r_a}\right)}{2 \pi \Delta} . \tag{42}$$

The resistivity η is taken to be the Spitzer resistivity for a plasma and Δ is the thickness of the plasma sheath. Plasma is considered a very good conductor and the typical values of plasma resistivity are very small in magnitude when compared to external circuit parameters.

The initial plasma sheath resistance was calculated using the initial fill gas density and an assumed initial breakdown temperature. This resistance was kept constant through the simulation and has negligible effect on current history.

Before the plasma sheath begins to propagate down the anode, it must first detach itself from the surface of the insulator. Particle pressures resulting from the arc formation, anchor the sheath to the insulator until the applied electromagnetic force overcomes the ambient pressure. This radial lift-off cannot occur unless the sheath current reaches a particular value. One can describe the threshold condition as:

$$\frac{B_\theta^2}{2 \mu_o} = nkT . \tag{43}$$

this is the balance condition between the magnetic pressure of the sheath and the plasma pressure. The magnetic induction B can be described by a previous expression derived from Ampere's law for a straight current carrying conductor as in Equation (33). Equation (33) is substituted into the pressure balance (Equation 43), and solved for the current I. The result is the expression for calculating liftoff current.

$$I = \sqrt{\frac{8 \pi^2 r_a^2 \rho N_A kT}{\mu_o A}} , \tag{44}$$

Where kT is the plasma sheath temperature in joules, N_A is Avogadro's number, ρ is the initial fill gas density, A is the atomic mass of the fill gas and r_a is the anode radius.

In order to calculate a lift-off current, an initial sheath temperature must be assumed for determining the particle pressure. It is assumed that the sheath pressure remains constant during the rundown phase. Significant heating of the sheath is assumed to occur during the radial collapse of the sheath due to compressional heating, and not in the rundown phase. This lift-off current is denoted as I_{LO} and is responsible for a delay in the

initiation of plasma rundown. In order to account for this lift-off delay, the lift-off current was added to the Snowplow model previously derived. The resultant expression gives

$$\dot{z} = \frac{1}{2\,m} \int_0^t \frac{L(t)\left[I^2(t) - I_{LO}^2\right] dt}{z}, \tag{45}$$

for the modified snowplow velocity.

The previously derived plasma relations are directly coupled to the circuit parameters in the load branch representing the plasma sheath. These sets of coupled equations realistically model the current history and rundown velocity of the dense plasma focus device.

Simulation of the Livermore-I Experiment

Once the equations describing the plasma sheath properties were developed and implemented into the transient solver, the code was used to simulate the Livermore-I plasma focus experiment. The input parameters and electrode geometry of the Livermore-I device were inserted into the input deck of the code. Table 2 shows the input parameters for this validation test. The calculated results from the code were plotted and when possible, compared against the experimental values. The Livermore-I experiment measured the total external current of the equivalent circuit and an inferred leakage current. This leakage current has not been directly measured, but it is indicative of a current loss mechanism.

Utilizing the anode profile of the Livermore-I experiment (Figure 15), Figure 16 shows the results of the calculated external and leakage currents and contrasts them with the experimental results from Livermore-I experiment. There is good agreement between the calculated and experimental curves, although the code underpredicts external current at the start of the transient and overpredicts current at the end of the run. This is thought to be due to the distortion of the sheath at lift-off and at collapse. The profile of the plasma sheath would determine the flux area between conducting surfaces and thus the sheath inductance. Variations in the inductance would affect the current history of the sheath, and it would appear that assuming a sheath profile perpendicular to the anode is good for times between the lift-off phase and when the sheath collapses to the axis.

Table 2. Input Parameters for the Livermore-I Plasma Focus Experiment

Input Parameters	Livermore-I Experiment
Voltage (volts)	2.7×10^{4}
Initial Inductance (henries)	2.5×10^{-8}
External Resistance (ohms)	5.0×10^{-3}
Leak Resistance (ohms)	1.2×10^{-1}
External Capacitance (farads)	3.55×10^{-4}
Anode Radius (cm)	5.08
Cathode Radius (cm)	8.0
Anode Tip Radius (cm)	1.27
Length of Insulator z_{lo} (cm)	14.0
Initial Point of Anode Curvature (cm)	31.4
Tip of Anode z_{tip} (cm)	38.2
Fill Gas Density (g/cm^3)	2.2×10^{-7}
Atomic Weight of Fill Gas (amu)	1
Assumed Lift-off Temperature (eV)	5
Time Step (sec)	5.0×10^{-8}

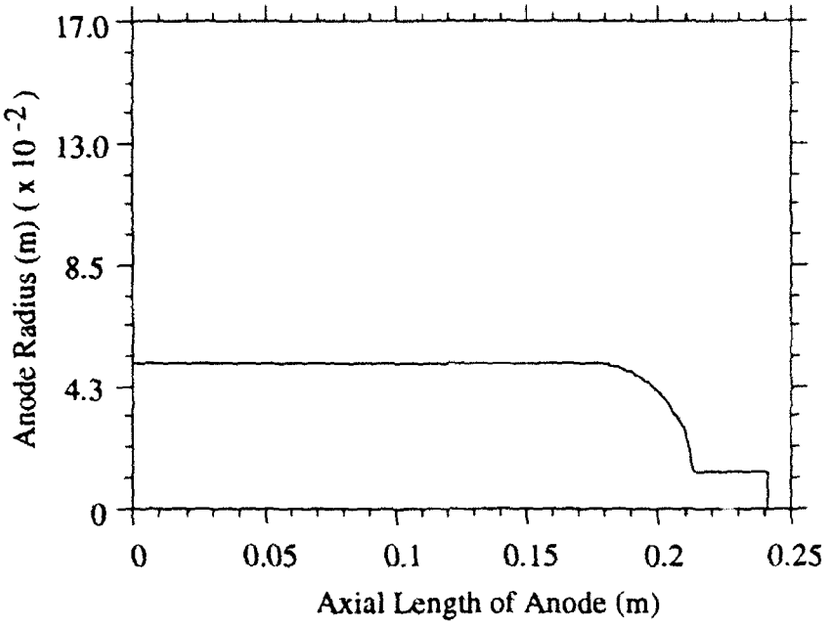

Figure 15
The Anode Profile of the Livermore-I Device

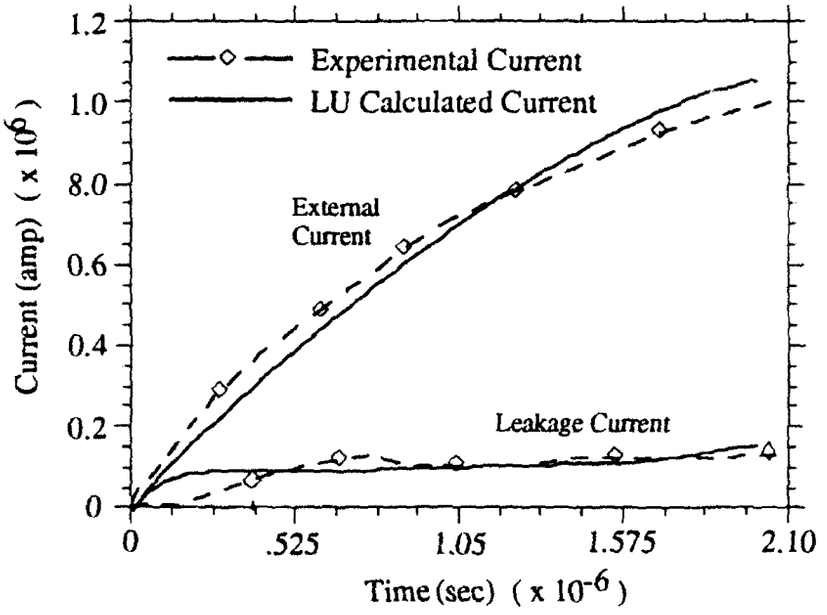

Figure 16
Experimental and Calculated Current
Histories for the Livermore-I Experiment

Figures 17 through 19 show the calculated values of plasma sheath inductance, axial rundown velocity, and the node voltage across the sheath and leakage components. Experimental results were not available for these plots due to the difficulty involved in measuring these quantities[21]. However, the calculated results represented the proper trend in behavior for the rundown phase of operation. The axial velocity in Figure 18 remains at zero until the sheath current reaches the lift-off value and begins to propagate down the anode. Axial velocity also displays a slowing down trend as the sheath hits the curved portion of the anode(see Figure 15), then it experiences an acceleration as the anode straightens out. This matches correctly with the inductance behavior at lift-off and at the end of rundown. The inductance remains constant before the sheath lifts off of the insulator and increases as the cross sectional flux area between the conductors increases. The voltage profile in Figure 19 also shows the voltage behavior expected during the transient. In the early stages of the transient, the gap voltage ramps up due to the effect of the fast rising current on the constant plasma sheath inductance. The voltage plateau in the middle of the transient is due to the rising inductance that occurs after the plasma sheath has started to propagate axially down the anode. At the end of the transient, the inductance increase because of the increase in cross sectional flux area that is due to the tapering anode

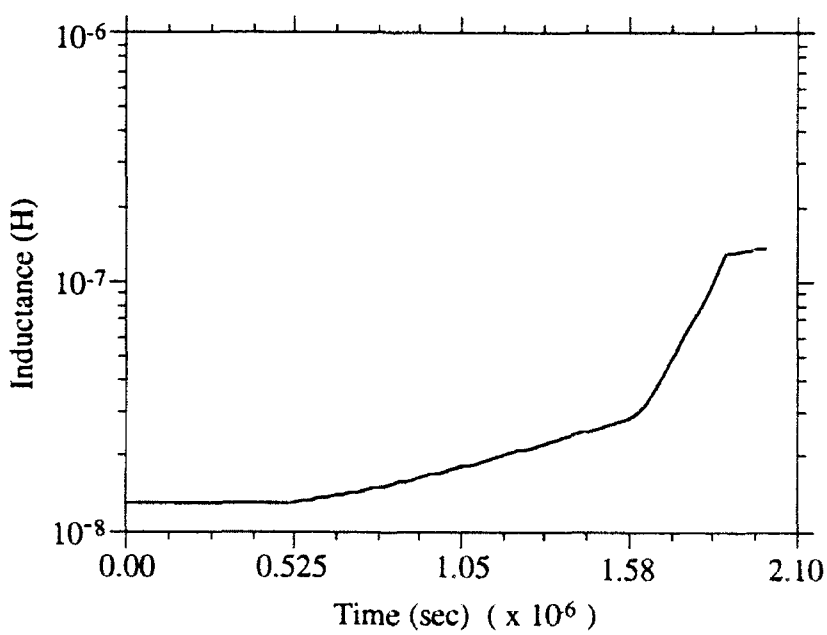

Figure 17
Calculated Plasma Sheath Inductance for the
Livermore-I Experiment

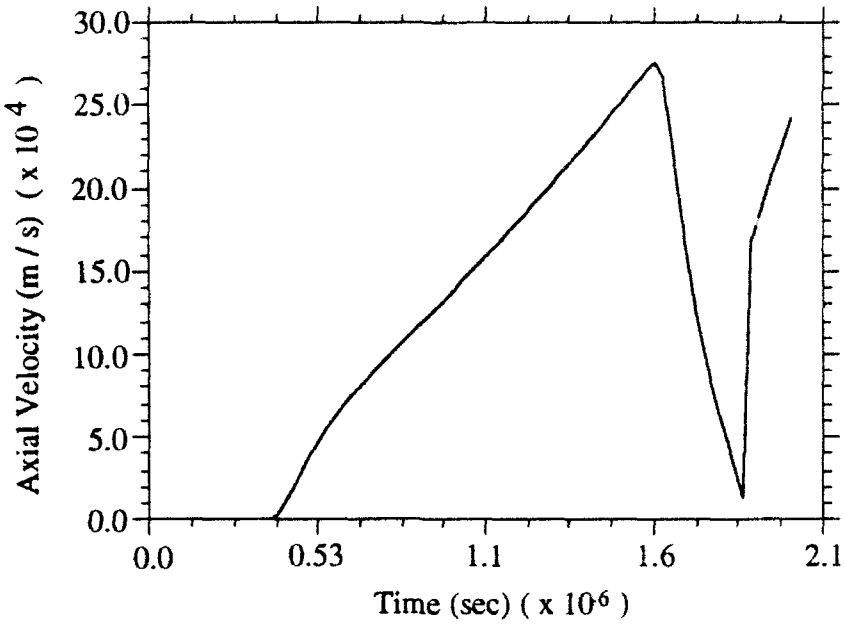

Figure 18
Calculated Axial Rundown Velocity for
the Livermore-I Experiment

tip. This last increase in inductance accounts for the voltage increase that occurs at the end of the transient.

The calculated results from the transient code were in good agreement with the experimental results and the general behavior that was expected. The differences in current history at the beginning and ending of the transient were due to the radial behavior of the sheath at liftoff and at the onset of sheath collapse. These are two-dimensional effects that cannot be easily accounted for using the one-dimensional snowplow model. The inductance, node voltage, and axial velocity behaved as expected and it should be noted that the snowplow model predicted a rundown velocity that did not exceed the implosion velocity limit of 3.5×10^5 m/s. This limit is based on the implosion velocity of an inertial confinement fusion target and is a good physical limit for the maximum velocity attainable for the plasma sheath.

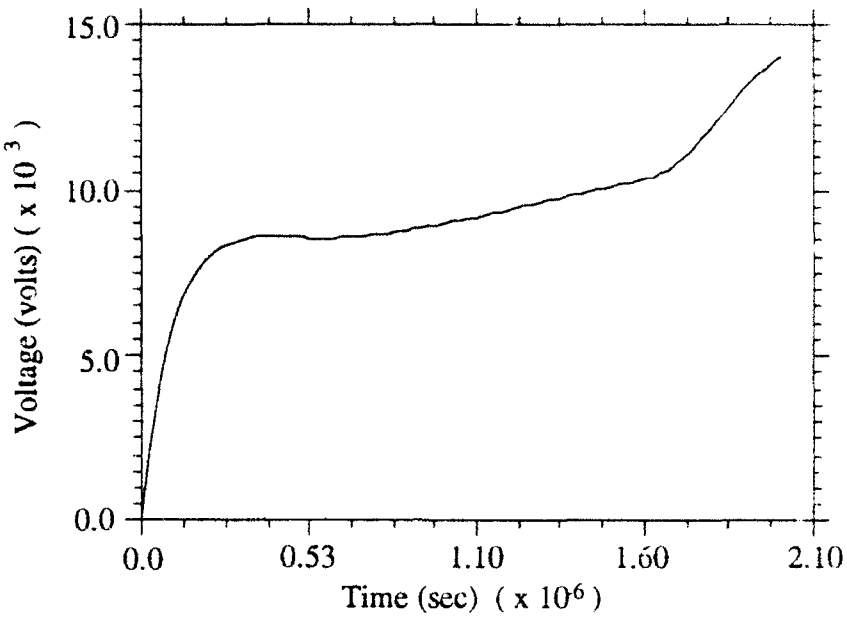

Figure 19
Calculated Gap Voltage Across the Plasma Sheath

PARAMETRIC STUDY OF THE DPF ELECTRODES

Introduction

Parametric testing of the effects of electrode configuration is addressed in this section. Initial studies on the application of the dense plasma focus as a space propulsion concept were done on the assumption that a device similar to the Livermore-I experiment could be made to produce the necessary current for fusion ignition. The purpose of this parametric study is to make a realistic assessment on this assumption that was made previously. In order to accomplish this objective, a variation of the radial dimensions of the anode will be implemented. All of the initial input parameters other than the radial dimensions will be kept constant and the effects of these electrode changes will be documented. If the radial variation does not produce the required ignition current, additional radial and axial variations will be implemented. Once the required ignition current is reached, the results from the end of rundown will be input into a code which calculates the performance of a DPF propulsion system. The system performance will be contrasted to previous system calculations that were carried out with assumed rundown values. Again, the goal of this work is to provide a realistic assessment of the parameter requirements that are needed to make the DPF device feasible as a space propulsion system.

Radial Variation of Anode

Plasma focus sheath current for the Livermore-I type device is sensitive to changes in the annular gap distance between cathode and anode. Reduction of this gap will lead to a reduced inductance which increases the magnitude of the plasma sheath current. The gap reduction will also reduce the volume of fill gas contained in the annulus. This means that less gas will be entrained in the sheath as it propagates down the device, which will limit the density in the pinch region. Ideally, the current and density at the end of the rundown phase should be optimized to present the best possible conditions prior to the pinch phase.

The radial parameter tests were conducted by increasing the anode radius in order to get a larger sheath current. The gap distance between the cathode and anode were reduced by half for each test case and the resulting currents were documented in Table 3.

Four different radial variations of the anode were used in these tests. The gap distances were reduced from the initial Livermore-I value of 0.0292 meter down to 0.00365 meter. Figure 20 shows the different profiles of the anode for these variations. Anode length and other plasma focus parameters were kept identical to the initial Livermore-I configuration. Figures 21 through 24 show the sheath currents, inductances, electrode gap voltages and rundown velocities of each test set. The maximum sheath current is reached at time t_{max} . It can be seen from the curves in Figure 21, that the maximum sheath current corresponding to the smallest gap length is only 1.527 MA. This is far below the required current needed to produce an adequate pinch temperature. Further reduction of the gap distance would result in an unacceptably low number density in the pinch.

Despite changes in the anode geometry, it is apparent that the DPF in the Livermore-I configuration cannot supply the magnitude of current needed for fusion ignition due to the large electrode gap. Reduction of the electrode gap distance will increase sheath current but also decrease total annular volume. The reduction in annular volume will mean that fewer fuel gas particles will be entrained into the pinch region after rundown. We can conclude that a Livermore-I type device is unsuited to the task of producing currents of 10 or 20 MA. This conclusion contrasts sharply to the previous assumption that a Livermore-I type device could produce this large magnitude of current.

Variations of Electrode Length and Charging Voltage

In order to facilitate the attainment of a 10-20 MA sheath current, device parameters other than the anode radius must be adjusted. The charging voltage of the capacitor bank will be increased in concert with the differing anode radii. The increases in charging voltage are conducted with the assumption that the initial external inductance and resistance remain at the same values. Lack of experimental information[22] on such high current circuits necessitates the need for this assumption. The initial charging voltage is increased for each test in increments of 27 kV, each new voltage is tested over three differing radial lengths(0.0508m, 0.0654m, and 0.0727m). Boosting the voltage increases the current in the sheath and thus the rundown velocity. This increase in axial velocity reduces the rundown time of the sheath. As a result, the sheath runs out of the device before peak current can be reached. In order to counteract this, the electrode length is accordingly increased so that the sheath runs out of the device when the peak current in the plasma arc is reached.

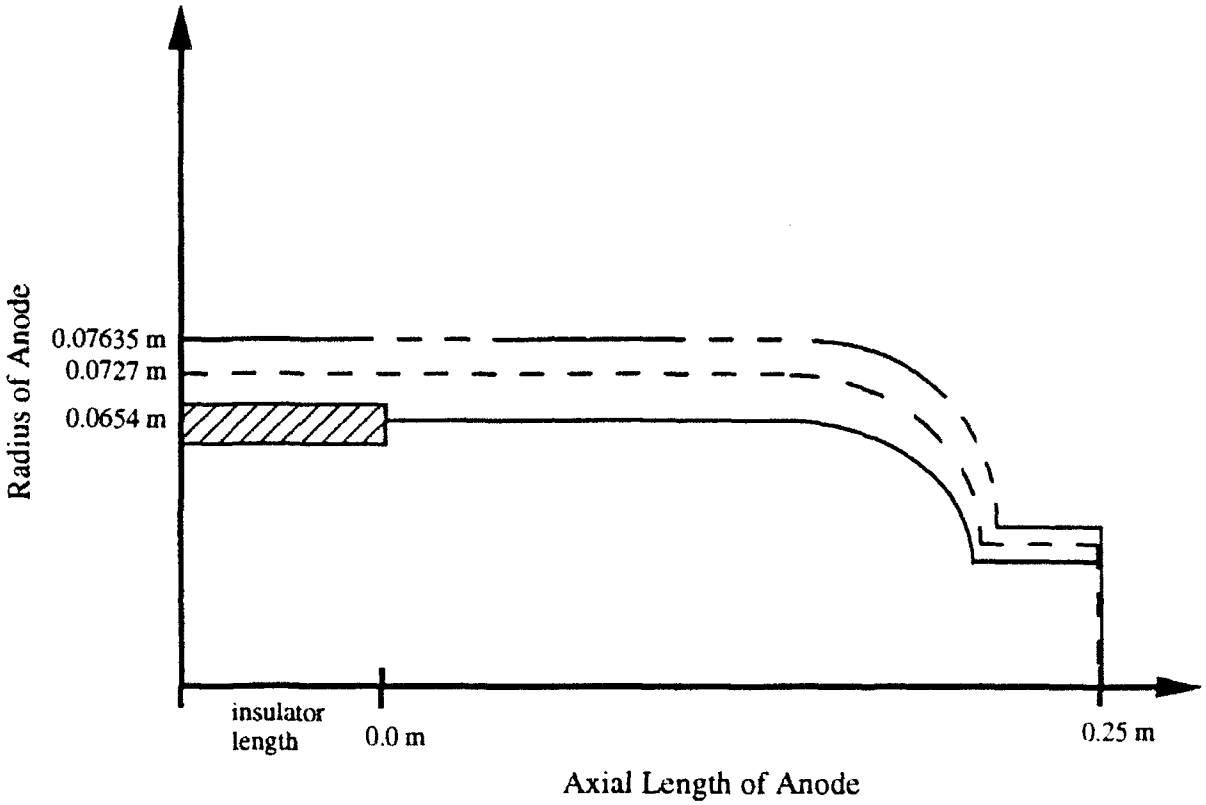

Figure 20
The Anode Variation Profiles

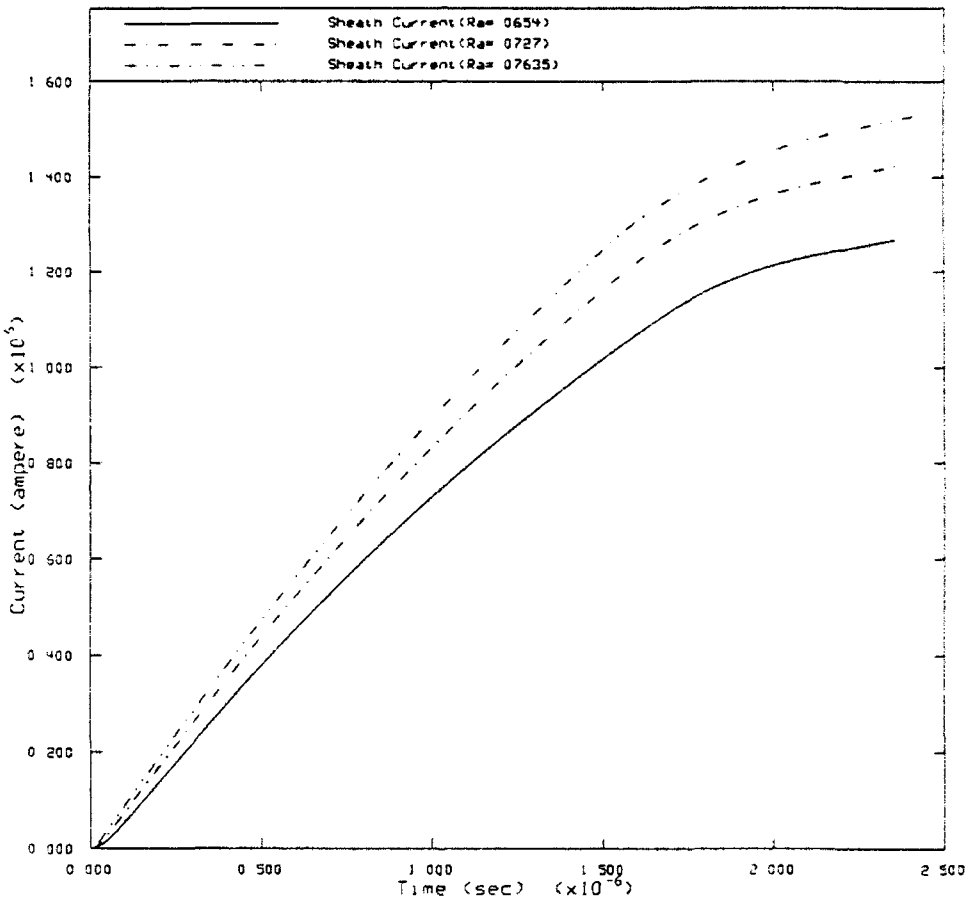

Figure 21
Sheath Current Histories for Anode Variation Tests

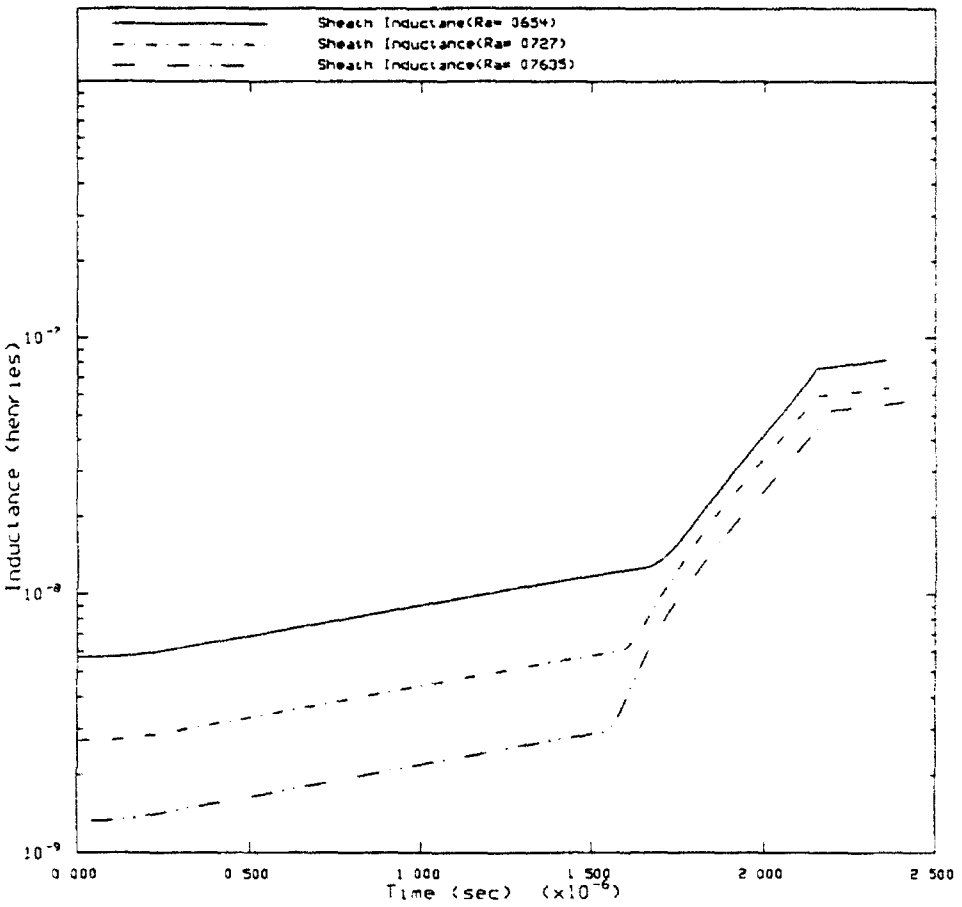

Figure 22
Inductance Curves for Anode Variation Tests

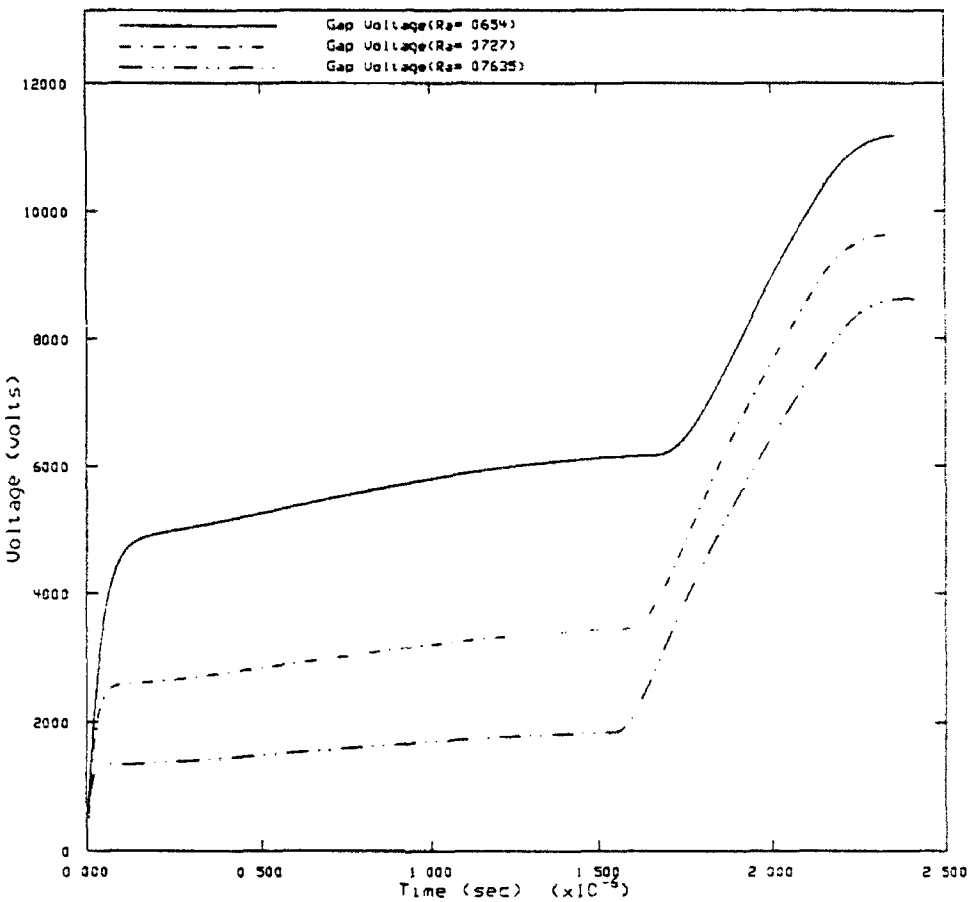

Figure 23
Anode/Cathode Gap Voltages for Anode Variation Tests

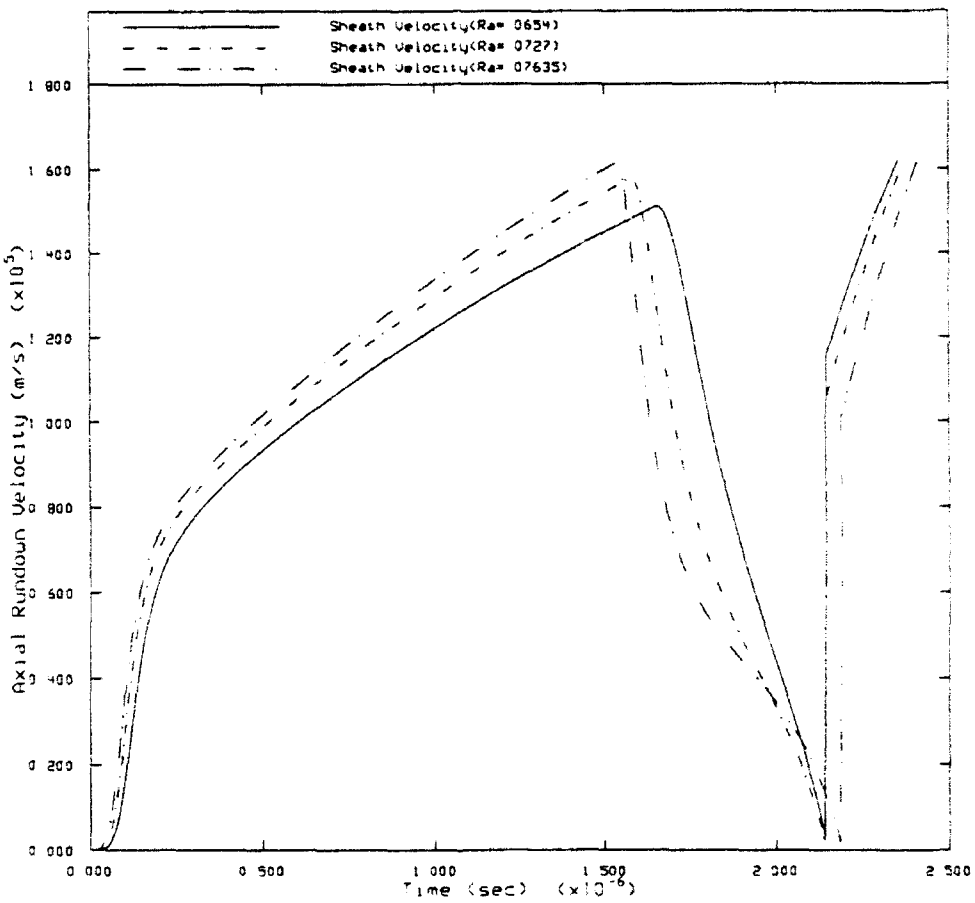

Figure 24
Axial Rundown Velocities for Anode Variation Tests

Sizing of the electrode length maximizes the geometry of the device for each new voltage, radius combination.

The voltage, and electrode variational tests were conducted until currents of 10,15, and 20 MA were obtained for each separate test combination. Table 3 shows the optimized voltage and geometry needed to obtain these necesssary currents.

Table 3. Optimized Parameters for High Current Delivery

Charging Voltage (kV)	Electrode Gap Distance (m)	Anode Radius (m)	Cathode Radius (m)	Electrode Length (m)	Maximum Current (MA)
162	0.0073	0.0727	0.08	1.177	10.07
189	0.0146	0.0654	0.08	1.402	10.09
243	0.0292	0.0508	0.08	2.152	10.03
243	0.0073	0.0727	0.08	1.222	15.07
270	0.0146	0.0654	0.08	1.902	15.08
378	0.0292	0.0508	0.08	1.952	15.04
*324	0.0073	0.0727	0.08	1.232	20.02
378	0.0146	0.0654	0.08	1.482	20.01
486	0.0292	0.0508	0.08	3.102	20.05
* Best Case					

It is desirable to minimize the voltage requirements as well as the geometrical dimensions of this device. For this reason,.the minimum voltage cases for the 10,15, and 20 MA range shall be used as the final voltage, geometry combinations. An assumption is made that the arc current will not saturate in the inter-electrode gap during operation. Another assumption made is that the electrode material can withstand the high temperature created by joule heating and the plasma arc. Each of the final chosen geometries have gap widths of 0.0073 meter, this allows the anode radius to be increased from the previous Livermore-I geometry. The new anode radius gives an increased electrode-arc interface area which results in a decreased current density. The decrease in effective current density is an added advantage for the chosen final geometries. The best case voltage-electrode combination is marked by an asterik in Table 3. This combination was chosen because it utilized the lowest charging voltage for the 20 MA cases. However, even the best case scenario utilizes an extremely high magnitude of input voltage which would require a Marx generator configuration for the input circuit. The 20 MA case is considered to be optimal for the DPF in the space propulsion application since the high current will provide higher plasma temperatures and enhanced reaction rates.

DENSE PLASMA FOCUS PROPULSION SYSTEM

Introduction

The use of the dense plasma focus as a viable propulsion concept requires that the system design not exceed practical standards for operation. The parametric study conducted in this work is a facet of DPF system design that was not rigorously explored previously by Choi and Leakeas[1]. The transient code calculations obtained in this work will be fed into the DPF system code [1]. The basic system design and requirements will be kept identical to the previously tested model, the only exception being the elimination of the assumption that a Livermore I type device could be used to generate the necessary current. The system code[1] will be rerun for the modified electrode geometries and charging voltages that were obtained from the parametric study in the previous chapter. The following subsections contain basic descriptions of the guiding principles used in the design of the DPF system code.

Rocket Dynamics

The performance characteristics of a rocket propulsion system can be judged using several important parameters which describe the power and efficiency of a system. One of the most vital parameters that describes rocket performance is specific impulse or I_{sp}. Specific impulse is defined as the amount of momentum gained per weight of fuel burned, and is given by the expression

$$I_{sp} = \frac{v_{ex}}{g}, \tag{46}$$

where v_{ex} is the exhaust velocity, and g is the gravitational constant of earth. The specific impulse uses the gravitational constant of earth instead of the local gravitation because it is a unif' d reference value for all types of propulsion devices. If one were to use the local gravitational constant in deep space, the gravity would be very minute and result in unreasonably high values of specific impulse. Therefore, it is expedient to normalize the

weight of fuel to the gravitational constant of the point of origin. Specific impulse is measured in units of seconds and is a good measure of the efficiency of a rocket. Thrust is another important performance parameter of a rocket system. The expression for thrust is given by the following expression

$$F_{thrust} = \dot{m}_{propellant}\, v_{ex} + A_{ex}\,(p_{ex} - p_{amb}) \tag{47}$$

where F is expressed in units of Newtons. The second term on the right of the equation represents the pressure force due to the differential pressure between the exhaust stream and the ambient pressure. This term is taken to be negligible in comparison to the primary force contributed by the rocket exhaust flow. The exhaust power of a rocket can be expressed in terms of thrust and specific impulse and is given by

$$P = \frac{1}{2} F\, v_{ex} = \frac{1}{2} g\, F\, I_{sp}\,. \tag{48}$$

This relation implies that for a fixed power, any increase in specific impulse will demand a similar decrease in thrust. In order to optimize a propulsion system, both of these parameters must be maximized. The last parameter necessary for defining performance is the burnout velocity of the vehicle or Δv. The Δv is derived from the equation of motion in free space for a rocket and is given by

$$\Delta v = v_{ex} \ln \frac{m_o}{m}\,, \tag{49}$$

where Δv is the velocity increment, m_o is the initial mass of the entire vehicle including fuel and payload, and m is the final mass of the vehicle without fuel. These parameters will play a key role in the understanding of the effectiveness of the DPF propulsion system.

Fusion Principles

The Dense Plasma Focus thruster relies on the generation of fusion power to provide vehicle thrust. Fusion is a thermonuclear reaction involving the fusing of ions, and is capable of generating large amounts of energy per unit volume. In order for fusion to occur, the ions must be forced together in order to overcome the Coulomb repulsive force that naturally repels particles with like charges. To accomplish this, a collection of high

temperature charged particles, also known as a plasma, must be confined, compressed and heated.

Fusion reactions depend largely on the plasma temperature, density, and confinement time. An expression for fusion power density is

$$P_F = n_1 \, n_2 \langle \sigma \, v \rangle \, W_o \, , \tag{50}$$

where n_1 and n_2 are the number densities of the non-equal reacting species, $\langle \sigma \, v \rangle$ is the reaction rate of the plasma, and W_0 is the energy liberated per reaction. The reaction rate parameter is a temperature dependent quantity which measures how quickly a reaction takes place at a given temperature. In order to calculate the total energy yield from a constant volume, simply multiply the power density by the volume of plasma and by the time over which the reaction extends.

Since these parameters are dependent on the choice of fusion fuel used, it is advantageous to select an optimal fuel for a specific application. For the case of the DPF thruster, we would like a fuel that fulfills certain criteria:

1. Provides a high energy output per reaction.
2. Maximizes the reaction rate parameter at "low" operating temperatures (keV range).
3. Suppresses neutron production since neutrons cannot be directed with a magnetic field.

Several fuel choices were considered as possible candidates for DPF fuel, these fuels are listed below.

$$D^+ + T^+ \rightarrow {}^4He^{++} \, (3.5MeV) + n \, (14.1MeV) \, , \tag{51}$$

$$\begin{aligned} D^+ + D^+ &\rightarrow T^+ \, (1.01MeV) + p \, (3.02MeV) \quad (50\%) \, , \\ &\rightarrow {}^4He^{++} \, (.82MeV) + n \, (2.45MeV) \quad (50\%) \, , \end{aligned} \tag{52}$$

$$D^+ + He^{3+} \rightarrow {}^4He^{++} \, (3.6MeV) + p \, (14.7MeV) \, . \tag{53}$$

The first reaction listed is a deuterium-tritium reaction, second is the DDn and DDp reaction, and lastly the deuterium-helium-3 reaction. The D-T reaction has the highest reaction rate at low temperature among three reactions, but 80% of the reaction energy is

carried away by the neutron. This is considered detrimental to the production of thrust, since the neutrons will fly in any direction and cannot be channeled by a magnetic field. The D-D reaction is split into two sub-reactions(DDn,DDp), each reaction having an equal probability of occurring. This reaction is also not desirable since there is a 50% probability of producing a neutron. This leaves D-^{3}He as the remaining candidate for the "low" temperature fuels. The D-^{3}He reaction produces the highest amount of energy per reaction (18.3MeV) and does not produce neutrons in its primary reaction. The reaction rate for a D-^{3}He reaction is also comparable to the D-T reaction rate at similar temperatures (keV range). Although D-^{3}He does not produce any neutrons, secondary neutron production in a D-^{3}He fuel is possible from background D-D reactions. The initial DPF system study by Choi and Leakeas [1], considered other possible advanced fuels such as proton-Lithium-6 and proton-Boron-11, but these fuels require ignition temperatures beyond reasonable limits (past 100 keV) and were discarded as possible choices.

Brief Description of DPF Propulsion System Code

The DPF system code (not to be confused with the transient code developed in this work) calculates the output power of the pinch and the resulting system performance of a DPF propulsion system. Many input parameters were assumed during the initial DPF study conducted previously[1]. The rundown calculations in the system code were discarded and replaced by the circuit transient code. This was done in order to provide a more realistic assessment of the design requirements of the DPF. However, the pinch phase calculations and system calculations are unchanged from the previous system code.

The following model provided a basis for the parameter calculations in the pinch region. The pinch was modeled as a cylindrical region of assumed radius and length that contained a certain fraction of sheath plasma. In order to determine the temperature inside the pinch region, a balance between magnetic pressure and plasma pressure was assumed.

$$n_p \, kT = \frac{B_\theta^2}{2 \, \mu_o} \, . \tag{54}$$

The azimuthal magnetic induction at the surface of the pinch volume is B_θ, μ_o is the permeability of free space, n_p is the pinch number density and kT is the product of Boltzmann's constant and the plasma temperature in degrees. The pinch number density n_p was assumed to be a fraction(f) of the initial gas density present in the annular region. This trapping fraction was chosen in order to provide a match with experimental values from

Livermore-I data ($n_p \sim 10^{26}/m^3$). Expressing n_p in terms of the electrode dimensions and initial fill gas density gives

$$n_p = \frac{f\,\rho_i\, l_a \left(r_c^2 - r_a^2\right)}{l_p\, r_p^2\, m_p}, \tag{55}$$

where l_a and l_p are the anode and pinch lengths, respectively, r_c, r_a and r_p are the radius of the cathode, anode and pinch, and m_p is the average mass of particles in the pinch. Utilizing Ampere's Law and integrating around the cylindrical surface of the pinch region gives an expression for the azimuthal magnetic induction B_θ (as equation 33)

$$B_\theta = \frac{\mu_o\, I}{2\,\pi\, r_p}. \tag{56}$$

By combining Equations (54) through (56), a final equation relating plasma temperature to current is obtained.

$$kT = \frac{\mu_o\, I^2\, m_p\, l_p}{8\,\pi^2\, f\,\rho_i\, l_a \left(r_c^2 - r_a^2\right)}. \tag{57}$$

The pinch analysis model assumes that this scaling holds regardless of input current magnitude.

The system code relied on the pinch parameters as an input for calculating the resultant fusion power. All of the performance parameters of the system are calculated around this energy yield. The DPF system itself consists of the dense plasma focus device, storage tanks for fuel and coolant, capacitor and charging circuit mechanisms and a magnetic nozzle. This standard configuration of the DPF system is displayed in Figure 25. The hydrogen tank supplies the necessary cryogenic needed to cool the walls of the cathode and the combustion chamber. This hydrogen can also be injected into the exhaust flow of the rocket to increase the resultant thrust. The capacitor banks are used to provide the discharge current necessary for operation and the turbine-generator is used to re-energize the banks after each discharge pulse. The turbine is driven by the cryogenic coolant after it has cooled the electrode and combustion chamber walls. The magnetic nozzle channels the exhaust flow of particles out of the combustion chamber[21]. The primary purpose of the magnetic nozzle is to prevent the fusion products from impacting

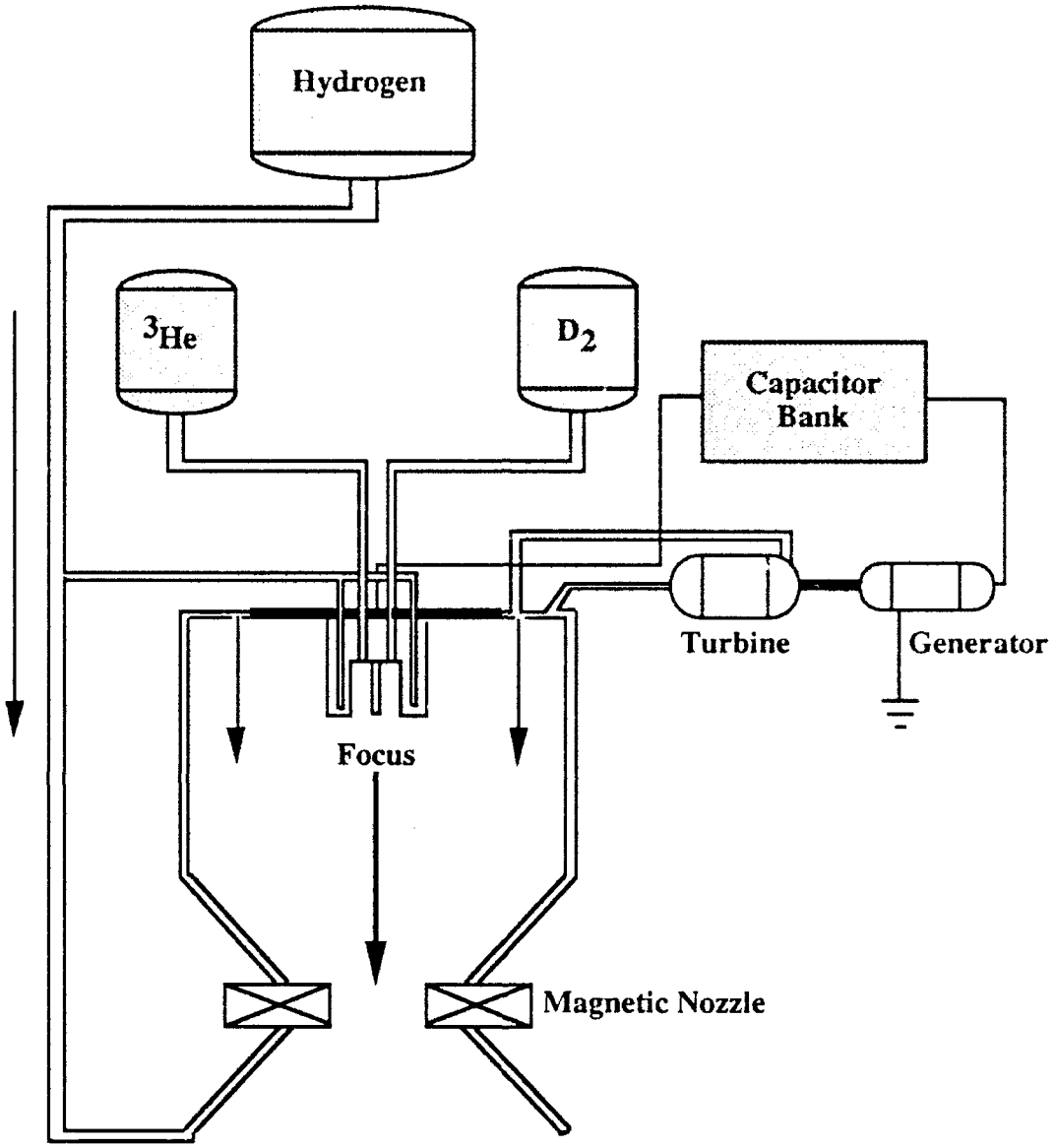

Figure 25
System Diagram for Dense Plasma Focus Thruster

with the wall material as well as generating and accelerated exhaust flow. For the continuous and impulsive modes of firing, the fusion products are diluted with the added hydrogen inflow which attenuates the charged particle temperature.
However, it is still desirable to keep the high energy flow away from the walls which will degrade the structural integrity of the combustion chamber.

An important factor for judging the performance of the DPF propulsion system is the total system mass. If this mass is too high, thrust-weight ratios are reduced, thereby cutting performance. Capacitor mass is a dominant component of the overall system mass and any reduction of this is highly desirable. Current technology allows a specific energy of about 0.2 kJ/kg for modern capacitors. In order to fulfill the requirements for the previous system model, capacitor masses on the order of 40,000 kg would be needed. To offset this problem, a further assumption was made that capacitors with specific energies of 2 kJ/kg could be obtained[1]. This would reduce the capacitor mass considerably and allow greater thrust-to-weight ratios. The system capacitor masses were previously calculated using an I^2 scaling law which relates the ratio of capacitor masses to a ratio of squared currents. The scaling law is derived by equating the ratio of capacitor masses to the ratio of energy expended in the operation of the device

$$\frac{M}{M_o} = \frac{W}{W_o} \tag{58}$$

The terms M_o and W_o are the capacitor mass and expended energy of a base case experiment while M and W are the new device values. The expended energy in the dense plasma focus can be expressed as the product of the magnetic force driving the sheath and the sheath displacement

$$W = \frac{B_\theta^2 \, \pi \left(r_c^2 - r_a^2\right)}{2 \, \mu_o} \cdot z \, , \tag{59}$$

where $$B_\theta = \frac{\mu_o \, I}{2 \, \pi \, r_p} \, ,$$

and r_p is the radius of the pinch region. Substituting B_θ and Equation (59) into (58) yields the scaling expression for capacitor mass.

$$M = \frac{I^2 \left(r_c^2 - r_a^2\right) z}{I_o^2 \left(r_c^2 - r_{ao}^2\right) z_o} M_o . \tag{60}$$

The previous DPF system study [1] assumed that the Livermore-I base case configuration would not have to be changed in order to attain the current necessary for operation. This assumption eliminated the geometrical dependence in the scaling law since both the base case and new configuration had identical dimensions. However, this study will utilize the geometrical dependence in the scaling law since the test case geometries differ from the Livermore-I base case geometry.

Another important factor that influences performance is the mode of operation of the system. Choi and Leakeas [1] considered three different modes of operation: 1) operation of the DPF as a closed system with no addition of hydrogen into the exhaust stream, 2) continuous firing with addition of hydrogen, 3) firing for short periods of time with large exhaust of hydrogen. The third mode was found to be the most advantageous since the large exhausts of hydrogen increased the exhaust mass flow rate and maximized thrust-to-weight ratio.

Performance Results with Modified Electrode Configurations

The new electrode configurations developed in Chapter 3 were tested on the DPF system code and contrasted with the results from the previous system study [1]. The tests were run for differing values of Δv using the enhanced electrode configurations. Plots were obtained for the specific impulse (I_{sp}) and thrust-to-weight ratio for each Δv requirement. High Δv requirements are necesssary in order to shorten trip time for longer range missions. The reduced trip time will minimize the vehicle occupants exposure to zero gravity and cosmic radiation. The mode of operation used in these test scenarios is the impulsive firing mode. It is one of the three operational modes previously mentioned, and it involves pulsing the thruster while exhausting large amounts of hydrogen into the exhaust flow. The advantages of this mode of operation is that it greatly reduces system mass due to the exhausting of massive amounts of hydrogen, this in turn increases the thrust-to-weight ratio significantly. The increased thrust-to-weight ratio allows the vehicle to accelerate rapidly until the fuel is exhausted.

The enhanced electrode configurations take advantage of the capacitor mass scaling law shown previously. The I^2 scaling with geometrical dependence predicts smaller capacitor masses than the previous I^2 scaling without geometrical dependence. The result is that the capacitor mass needed for the enhanced configurations is smaller than that for a

Livermore-I type geometry. A nominal base case was chosen in the previous DPF system study. This base case was for a plasma sheath operating current of 20 MA and a Δv requirement of 10 km/s. Table 4 shows the comparison between the base case outputs for the assumed Livermore-I configuration and the enhanced 20MA electrode configuration of this study.

Figures 26 through 31 show the plots for specific impulse and thrust-to-weight ratios for different Δv requirements. For Δv=5km/s (Figure 26), the specific impulse of the Livermore-I geometry electrodes and the enhanced electrodes showed little difference. The best case appears to be for the 20MA enhanced electrode configuration. The 20MA current provided a better fusion burn in the pinch which resulted in a higher exhaust velocity over the varying range of propellant mass flow rates. The propellant mass flow rate is the mass flow rate of hydrogen that is injected into the combustion chamber. This injection of hydrogen will increase the thrust of the device by increasing the mass expelled from the exhaust of the vehicle. However, if the mass flow rate increases for a fixed current, the exhaust velocity decreases due to the collisional transfer of energy between the the charged particle fusion products and the injected hydrogen. The resultant trend is the degradation of specific impulse for increasing hydrogen mass flow rates. Figure 27 shows the thrust-to-weight ratio for the Δv=5km/s case. The thrust-to-weight ratio of the enhanced configuration shows a marked improvement over the previously assumed Livermore I geometry. This plot shows the trend of thrust-to-weight ratio increasing as the propellant mass flow increases. Again, the best case appears to occur for the 20MA enhanced electrode configuration.

The other test cases for Δv=20 and 40km/s show basically the same trend as the Δv=5km/s case. The enhanced electrode configuration operating at 20MA seems to provide the optimal case for each Δv requirement. For increasing Δv requirements the thrust-to-weight ratio curve tends to flatten out or decrease for increasing propellant mass flow rates. This is due to the extra propellant mass that must be carried in order to reach the required Δv. The increase in propellant mass will decrease the thrust-to-weight ratio attainable by the system. Inevitably, we come to the same conclusion as the previous study, that the DPF system thruster is most efficient for low Δv requirement applications.

Table 4. Propulsion Parameters for Base Case
(Δv=10km/s, I=20MA)

			Livermore I Electrodes	Enhanced Electrodes
Rundown Velocity	v_{run}	(m/s)	3.35×10^6	3.5×10^5
Deuterium Burnup Fraction	f_D		0.699	0.694
Helium-3 Burnup Fraction	f_{He}		0.442	0.433
D-^{3}He Fusion Power	P_{DHe}	(MW)	2743.854	2910.19
DDn Fusion Power	P_{DDn}	(MW)	18.65955	20.41
DDp Fusion Power	P_{DDp}	(MW)	83.55009	91.79
Total Fusion Power	P_F	(MW)	2846.066	3022.40
Power to Focus	P_{in}	(MW)	5.4	64.80
Bremsstrahlung Loss	P_B	(MW)	15.79	26.75
Cyclotron Loss	P_C	(MW)	81.49	118.6098
Total Power Loss	P_L	(MW)	97.2943	145.3646
Power Increase	ΔP	(MW)	2743.363	2812.235
Total Mass Flow	M_T	(kg/s)	31.00	31.233
Propellant Thrust	F_P	(N)	4.73×10^5	4.84×10^5
Total Burn Time	t_b	(s)	3479.949	3328.988
Payload Mass	M_L	(kg)	1×10^5	1×10^5
Propellant Mass	M_p	(kg)	2.12×10^5	2.046×10^5
Propulsion System Mass	M_{sys}	(kg)	3.18×10^4	3.06×10^4
Fuel Mass	M_F	(kg)	0.7018	0.59705
Fuel System Mass	M_{Fsys}	(kg)	0.0702	0.0597
Capacitor Mass	M_C	(kg)	17231.29	15324.15
Shield Mass	M_{sh}	(kg)	8272.426	8272.031
Magnet Mass	M_B	(kg)	67.55	67.55
Total Mass	M_{Tot}	(kg)	3.69×10^5	3.59×10^5
Total Thrust	F	(N)	4.73×10^5	4.84×10^5
Thrust-to-Weight	F/W		0.131	0.137
Specific Impulse	I_{sp}	(s)	1583.344	1607.442

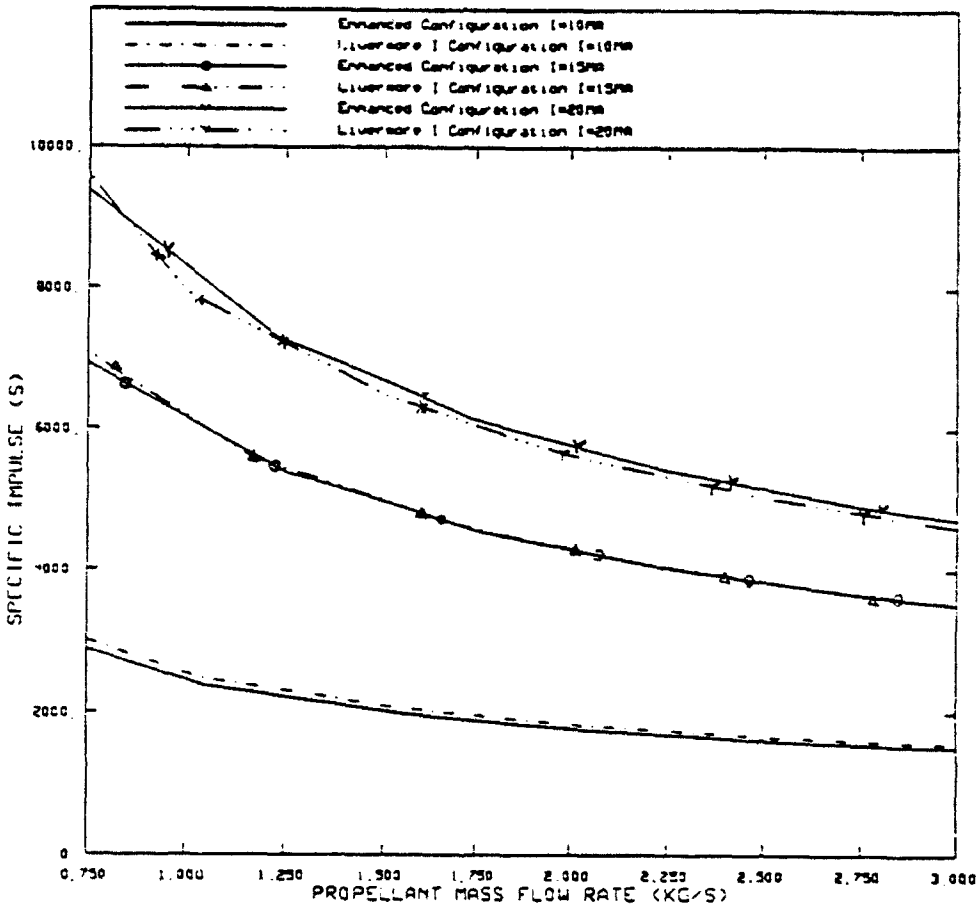

Figure 26
Specific Impulse vs. Propellant Mass Flow Rate
(Δv=5km/s)

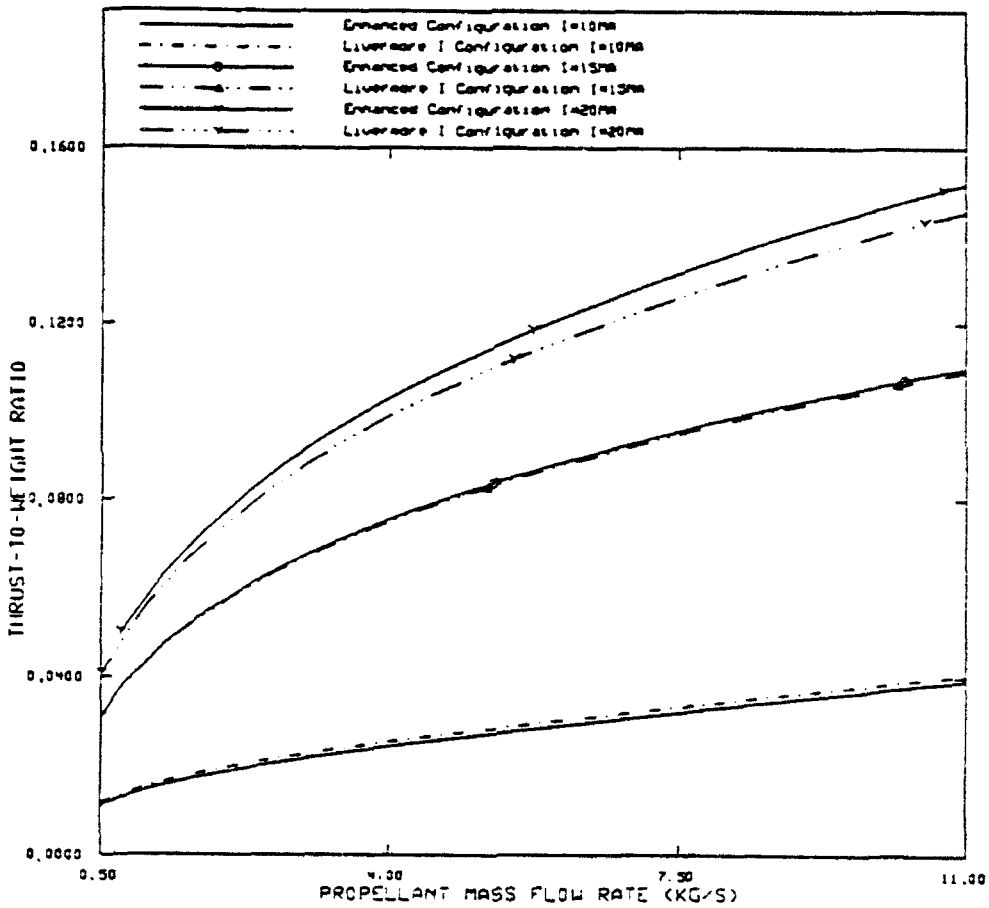

Figure 27
Thrust-to-Weight Ratio vs. Propellant Mass Flow Rate
(Δv=5km/s)

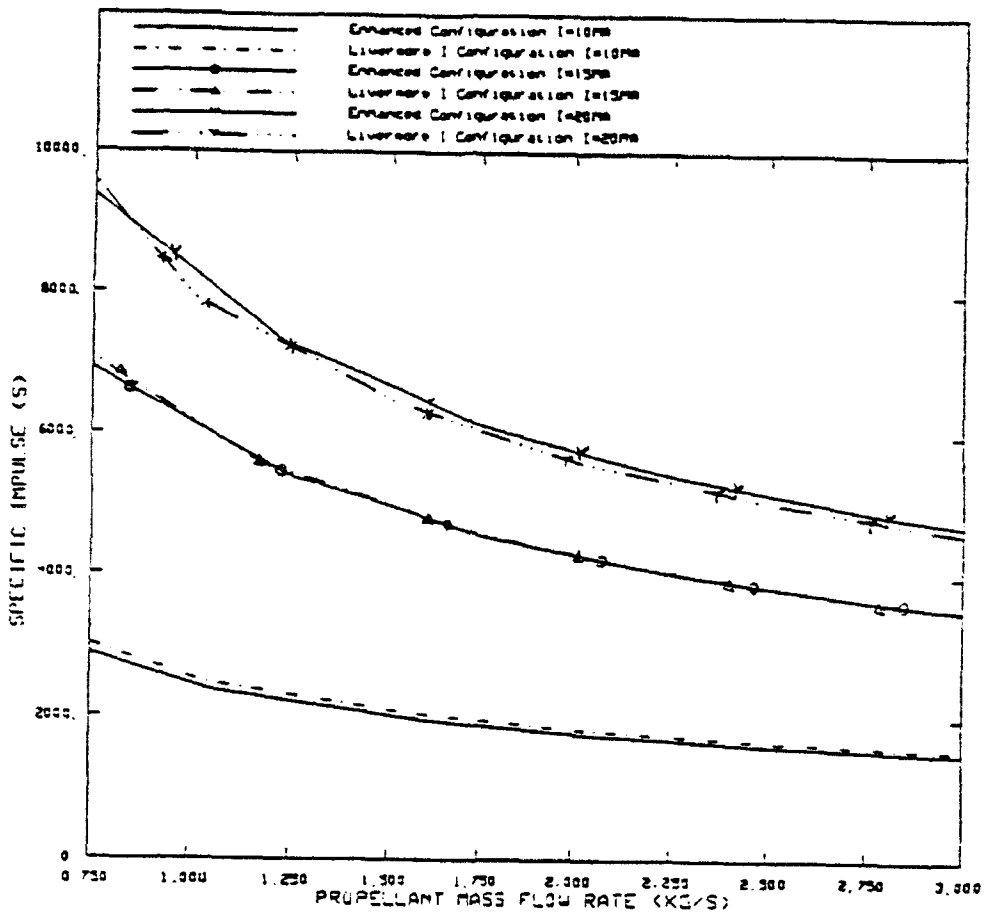

Figure 28
Specific Impulse vs. Propellant Mass Flow Rate
(Δv=20km/s)

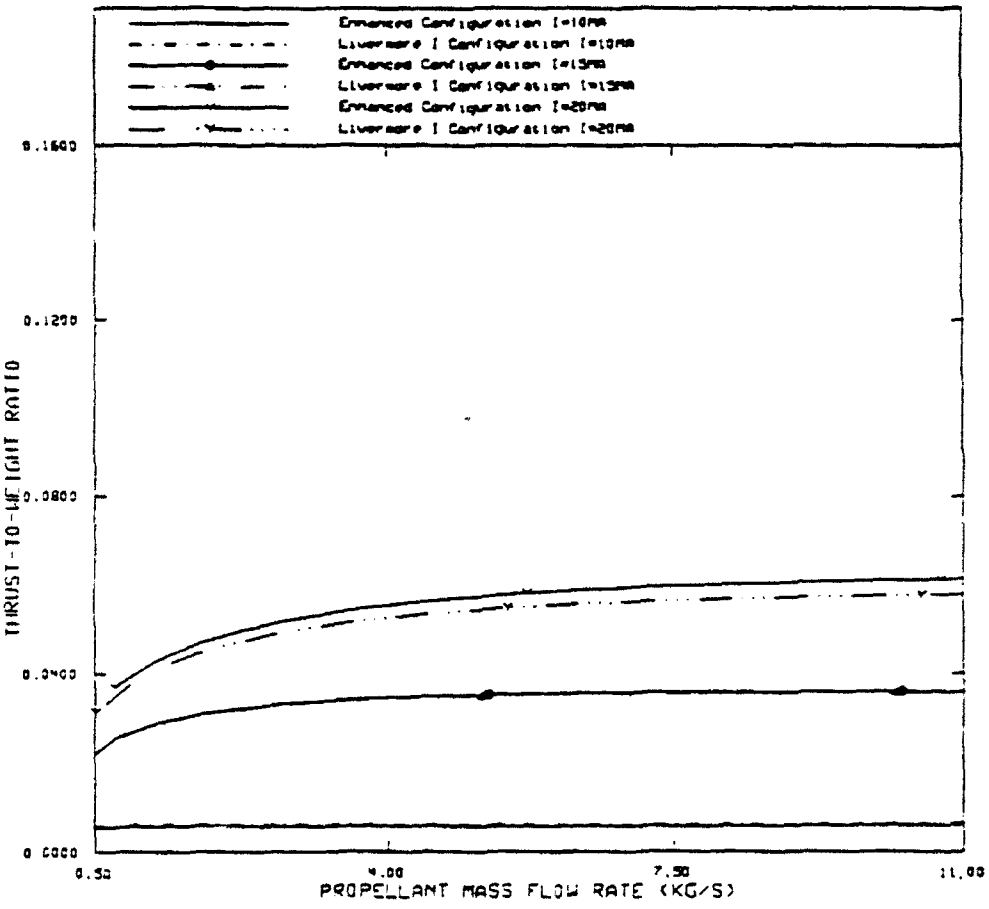

Figure 29
Thrust-to-Weight Ratio vs. Propellant Mass Flow Rate
(Δv=20km/s)

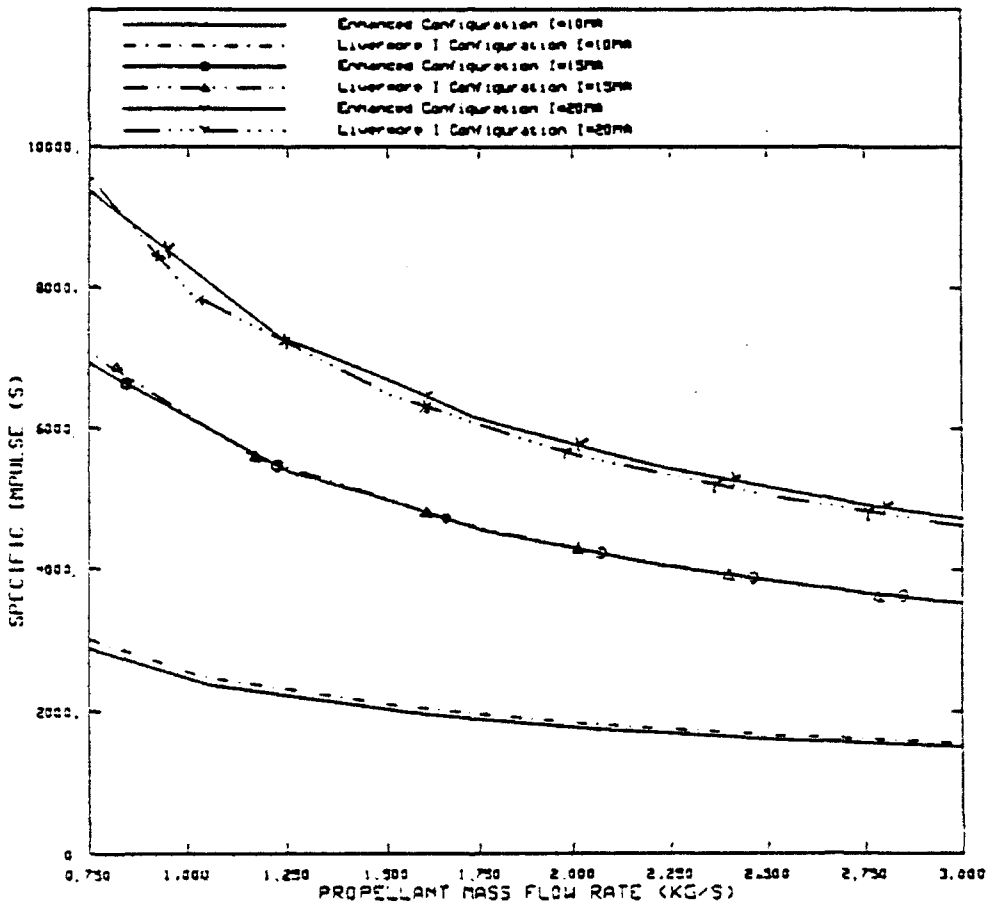

Figure 30
Specific Impulse vs. Propellant Mass Flow Rate
(Δv=40km/s)

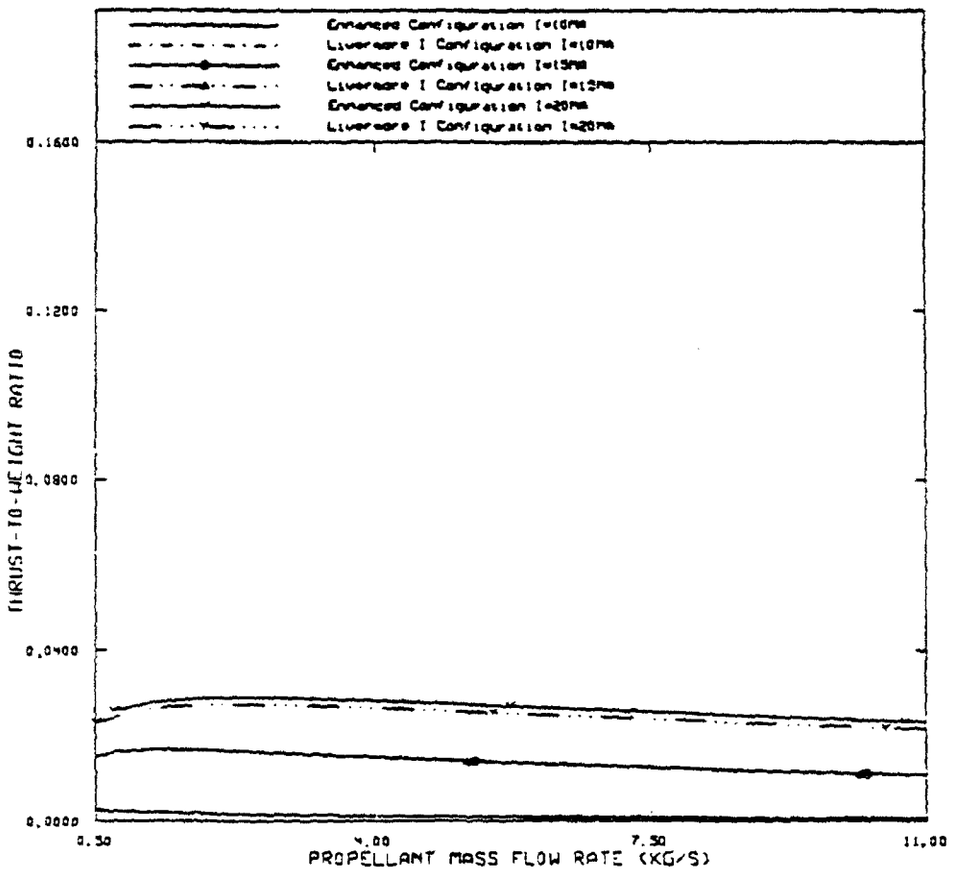

Figure 31
Thrust-to-Weight Ratio vs. Propellant Mass Flow Rate
(Δv=40km/s)

CONCLUSIONS AND RECOMMENDATIONS

An equivalent circuit representation of the dense plasma focus device was developed for use in a 1-D transient code which solved for the sheath dynamics during the rundown phase as well as the current history of the device. A leakage current component was inserted into the equivalent circuit to account for sheath current losses during the operation of the plasma focus. The leakage component was modeled as a constant resistance which shunted part of the external current away from the plasma sheath. The parameter values of the sheath were modeled as time dependent variables to account for the changing behavior of the arc during rundown. The dynamic nature of the sheath parameters made it necessary to remodel the circuit after updating the sheath inductance for each time step. Relations for the plasma sheath parameters were developed as well as a snowplow model for predicting the plasma sheath dynamics during rundown. These relations were inserted into the transient code and another test case was run using the Livermore-I plasma focus experiment for comparison.

The transient code used to calculate the current history for a given electrode geometry utilized an equivalent circuit representation of the DPF coupled with plasma relations for the sheath. This scheme solved the system of coupled circuit equations numerically using LU decomposition. The transient code was tested on a trial circuit with static resistance and reactance. These results compared very well to results calculated analytically and with the SPICE circuit modeling program. The error between the transient code calculated solutions and the analytical and SPICE solutions were generally on the order of 0.1 percent. The accuracy of the transient solver was validated for these series of static tests. The calculated results using the transient code predicted an external current history that was in good agreement with the experimental results. The calculated leakage current was also in good agreement with the experimental data obtained from the Livermore I experimental report. This experimental leakage component is an inferred value that could not be directly measured in the Livermore I experiment. The presence of the leakage current is needed in this equivalent circuit model to account for a current loss mechanism which degrades the current delivered to the plasma sheath. This leakage component is

assumed to be a leakage current over the insulator, but further experimentation is needed to substantiate this assumption.

After the static circuit validation tests were conducted, the crowbar branch of the circuit was switched in to determine its effect on the load current history. The results of this test exhibited a positive effect on the reduction of current damping in the load. The degree of reduction of the current damping effect depends heavily on the choice of crowbar inductance and resistance values. Theoretically, it is possible to greatly reduce the damping effect after peak current has been reached by reducing the crowbar inductance. However, there exists a practical limit as to how small an inductance can realistically be achievable for the crowbar branch.

The Livermore-I geometry was taken and modified in order to provide the very high current that was needed to heat the pinch. Various radial and axial anode variations were tested in order to determine the effect on current history. It was discovered that the Livermore-I experimental configuration would not provide the necessary current required to produce fusion ignition. As a result, the charging voltage had to be increased in order to provide a greater current delivery capability. The dimensions of the electrodes were varied for each increased value of charging voltage. These data were recorded and the optimal configurations were chosen for future testing. These configurations were chosen for minimal charging voltage requirements and minimized electrode dimensions. One enhanced electrode and charging voltage combination was chosen for each operating current requirement (10, 15, and 20MA). Each of these combinations were run on the transient code and the results were input into a DPF system code which calculated the performance of the thruster. For the best case scenario (lowest charging voltage 324 kV, highest sheath current 20 MA) the capacitor energy discharge curve was plotted (Figure A.17). For this case, it can be seen that approximately 2/3 of the initial energy contained in the capacitor is discharged in the rundown phase. A fraction of this quantity is deposited into the plasma when the pinch is formed, but a more detailed modeling of the pinch region is needed to determine this quantity.

The goal of this study was to determine the effects of changing electrode geometry on current history and plasma focus performance in the 10-20 MA range. It was found that the electrodes did not have to undergo drastic changes in configuration to achieve these high currents, but the charging voltage had to be increased to a level which is beyond what is currently achievable. The SHIVA experiment conducted at Kirtland Air Force Base claims a load current of approximately 9 MA at a charging voltage of 125 kV[10]. This provides a baseline as to the current state of high current pulse power technology. The

DPF system would need at least a 25% higher charging voltage and a discharge circuit that could handle the high current effects. If such a circuit could be designed and implemented, perhaps experimentation of the dense plasma focus in this current range could be conducted.

The effective result of the new enhanced electrode configurations is a decrease in the necessary amount of capacitor mass. This allows the thrust-to-weight ratio to be increased significantly from previous calculations. Another effect of the enhanced electrode design is an increase in fusion power provided by the device. A longer annular region allows more fill gas to be entrained during rundown. This increases the amount of gas entrained in the high temperature pinch region, which results in a greater amount of fusion fuel being burned. The thrust-to-weight ratios are maximized for short mission Δv requirements. This increase in thrust-to-weight ratio will decrease trip time of the mission vehicle and its occupants. Specific impulse for the enhanced electrode configuration differs little from the Livermore-I values, though for the 20MA case, the enhanced configuration is superior to the Livermore-I configuration.

Tests utilizing different anode tip geometries were also run using the transient modeling code. The three different anode tip geometries that were tested provided a basis for observing the effects of changing anode tip configurations. Equilateral, cylindrical, and extended triangular anode tips were tested for the resulting current histories in the MA range. Illustrations of these tip geometries are in Appendix A along with the resulting current histories and performance plots. The equilateral and cylindrical tips proved to be nearly identical in performance to the Livermore-I sloped anode tip, while the extended triangular tip appeared to provide degraded performance characteristics. The lack of current capacity of the extended triangular tip appears to be due to the increased plasma impedance caused by an elongation of the plasma sheath as it travels towards the anode tip. In contrast with this, the equilateral and cylindrical tips would not experience the same effect due to the shorter lengths of the anode for these geometries. One must note that these conclusions are only valid when analyzing the current carrying histories of the different geometries. Perhaps the extended tip geometry would be more favorable to pinch formation than either the equilateral or cylindrical tips.

The dense plasma focus device has the possibility of becoming a desirable space propulsion concept. If the current and capacitor scaling laws hold, and if tougher higher temperature conductors can be developed, the DPF can provide system performance that will exceed other alternative concepts. Questions about the scaling laws and the physics of

the plasma pinch phase must be studied further before the DPF can be considered as a plausible fusion energy source.

The results of this study provided a more realistic view of the electrode and input requirements needed to produce very high currents during rundown. These modifications produced a more optimistic view of DPF thruster performance for different Δv requirements. The significant reduction in capacitor mass is a result of the geometrical dependence of the capacitor mass scaling law. This mass reduction plays a key role in the boosting of the system thrust-to-weight ratio. Further experimentation is needed to substantiate the assumptions that the sheath current will not saturate in the 10-20 MA range.

LIST OF REFERENCES

[1] Choi, C.K., Leakeas, C.L., "Parametric Studies of the Dense Plasma Focus for Fusion Propulsion using D-^{3}He", Fusion Technology, 20, p. 735-740 (1991).

[2] Dolan, T.J., Fusion Research Experiments, Volume II, Pergamon Press, N.Y., 1982, p. 313.

[3] Bussard, R.W., DeLauer, R.D., Nuclear Rocket Propulsion, McGraw Hill, N.Y., 1958.

[4] Stuhlinger, E., Ion Propulsion for Space Flight, McGraw Hill, N.Y., 1964.

[5] Penner, S.S.(Editor), Advanced Propulsion Techniques, Pergamon Press, N.Y., 1961.

[6] Choi, C.K., "Engineering Considerations for the Self-Energizing MPD-Type Fusion Plasma Thruster", Phillips Laboratory, PL-TR-91-3087, 1992.

[7] Haloulakos, V.E., and Borque, R.F., "Fusion Propulsion Study", McDonnell Douglas Corporation, Huntington Beach, CA, AL-TR-89-005 (July 1989).

[8] Eltgroth, P.G., "Comparison of Plasma Focus Calculations", Physics of Fluids , v. 14, pp. 1911 - 1924, September 1982.

[9] Herold, H., Jerzykiewicz, A., Sadowski, S., and Schmidt, H., "Comparative Analysis of Large Plasma Focus Experiments Performed at IPF, Stuttgart, and at IPJ, Swierk", Nuclear Fusion , 29 , (1989).

[10] Degnan, J.H., Baker, W.L., Hackett, K.E., et al, "Experimental Results from SHIVA Star Vacuum Inductive Store/Plasma Flow Switch Driven Implosions", IEEE Transactions on Plasma Science, v. PS-15, no. 6, pp. 760 - 771, December 1987.

[11] Imshennik, V.S., Filippov, N.V., Filippova, T.I., "Similarity Theory and Increased Neutron Yield in a Plasma Focus", Nuclear Fusion , 13 , (1973), pp. 929 - 934.

[12] Oppenlander, T., Pross, G., Decker, G., and Trunk, M., "The Plasma Focus Current in the Compression Phase", Plasma Physics , v. 19, pp. 1075 - 1083, 1977.

[13] Trunk, M., "Numerical Parameter Studies for the Dense Plasma Focus", Plasma Physics , v. 17, pp. 237 - 248, 1975.

[14] Feugeas, J.N., "The Influence of the Insulator Surface in the Plasma Focus Behavior", Journal of Applied Physics , v. 66, pp. 3467 - 3471, October 1989.

[15] Dietz, D., "Coaxial Plasma Accelerator in the Snowplow Mode: Analytical Solution in the Weak Coupling Limit", Journal of Applied Physics , v. 62, pp. 2669 - 2674, October 1987.

[16] Kondoh, Y., Hirano, K., "Numerical Study of an Ion Acceleration in a Z-Pinch Type Plasma Focus", Physics of Fluids , v. 21, pp. 1617 - 1622, September 1978.

[17] Maxon, S., Eddleman, J., "Two-Dimensional Magnetohydrodynamic Calculations of the Plasma Focus", Physics of Fluids , v. 21, pp. 1856 - 1865, September 1978.

[18] Thompson, C.A., "A Study of Numerical Integration Techniques for use in the Companion Circuit Method of Transient Circuit Analysis", Master's Thesis, Department of Electrical Engineering, Purdue University, 1992.

[19] Vladimirescu, A., Newton, A.R., et al, "SPICE Version 2G User's Guide", Department of Electrical Engineering and Computer Sciences, University of California, Berkeley, 1981.

[20] Jahn, R.G., Physics of Electric Propulsion , McGraw Hill, N.Y., 1968.

[21] Pickles, W., (Lawrence Livermore), Personal Correspondence, March 1992.

[22] Degnan, J.H., (Kirtland Air Force Base, NM), Personal Correspondence, February, 1992.

[23] Gerwin, R.A., Marklin, G.J., Sgro, A.G., and Glasser, A.H., "Characterization of Plasma Flow through Magnetic Nozzles", AL-TR-89-092, Astronautics Laboratory (AFSC), Edwards AFB, CA., February 1990.

[24] Potter, D.E., "Numerical Studies of the Plasma Focus", Physics of Fluids, v. 14, pp. 1911 - 1924, 1971.

[25] Dolan, T.J., Fusion Research Principles, Volume I, Pergamon Press, N.Y., 1982, p. 54 - 56.

[26] Sutton, G.P., Rocket Propulsion Elements , McGraw Hill, 3rd Edition.

[27] Howatson, A.M., An Introduction to Gas Discharges , Pergamon Press, N.Y., 1965.

[28] Llewellyn-Jones, F., The Glow Discharge, Methuen & Co. Ltd., London, 1966.

[29] Eltgroth, P.G., (Lawrence Livermore), Personal Correspondence, February 1992.

[30] Hirano, K., Yamamoto, T., Yokoyama, M., Yamamoto, Y., et al, "Investigation of Plasma Dynamics and Emissions in a Dense Plasma Focus", Proceedings - International Conference on Plasma Physics and Controlled Nuclear Fusion, v. 2, pp. 583 - 592, November 1986.

[31] Czelaj, S., Denus, S., Kasperczuk, A., et al, "Investigation of Collapse, Pinch Dynamics and Fast Particle Emission in a Plasma Focus Discharge", Proceedings - International Conference on Plasma Physics and Controlled Nuclear Fusion, v. 2, pp. 593 - 601, November 1986.

[32] Jerzykiewicz, A., Brandt, S., Kociecka, K., et al, "Plasma Focus Research at the Institute for Nuclear Studies, Swierk", Proceedings - International Conference on Plasma Physics and Controlled Nuclear Fusion, v. 2, pp. 737 - 741, October 1988.

[33] Wiesel, W.E., Spaceflight Dynamics, McGraw Hill, N.Y., 1989.

[34] Price, D.W., Baker, W.L., Beason, J.D., Degnan, J.H., et al, "Enhanced Load Current Delivery from the SHIVA Star Vacuum Inductive Store/Plasma Flow Switch", IEEE Transactions on Plasma Science, v. 16, no. 4, pp. 423 - 427, August 1988.

[35] Hoffman, J.D., "Numerical Methods for Engineers and Scientists", Class Notes, Department of Mechanical Engineering, Purdue University, 1990.

APPENDIX A

Various Electrode Configurations and Associated Performance Parameters, Figures A.2 through A.4 which were illustrated earlier in the main text are are shown here in repetition. This is done in order to compare them with the different anode geometries presented in this Appendix.

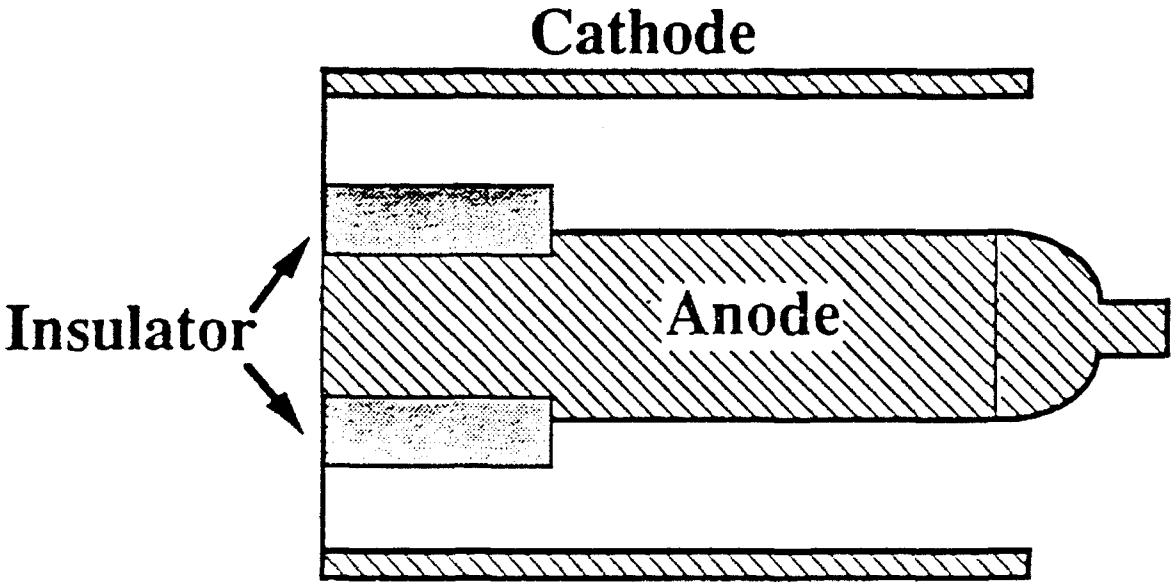

Figure A.1
Livermore-I Plasma Focus Electrode Geometry

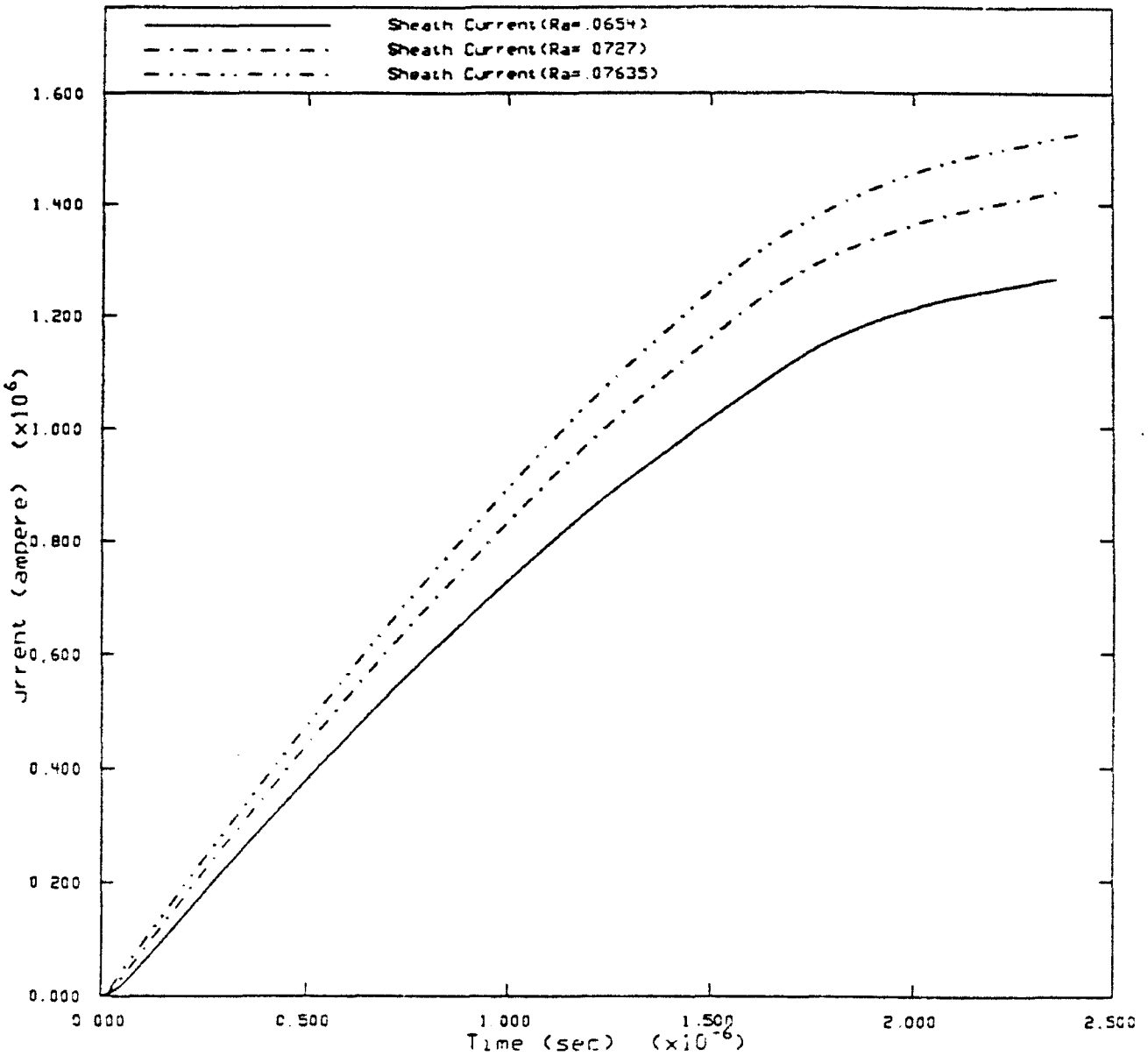

Figure A.2
Sheath Current Histories for Anode Variation Tests
(Same as Figure 21)

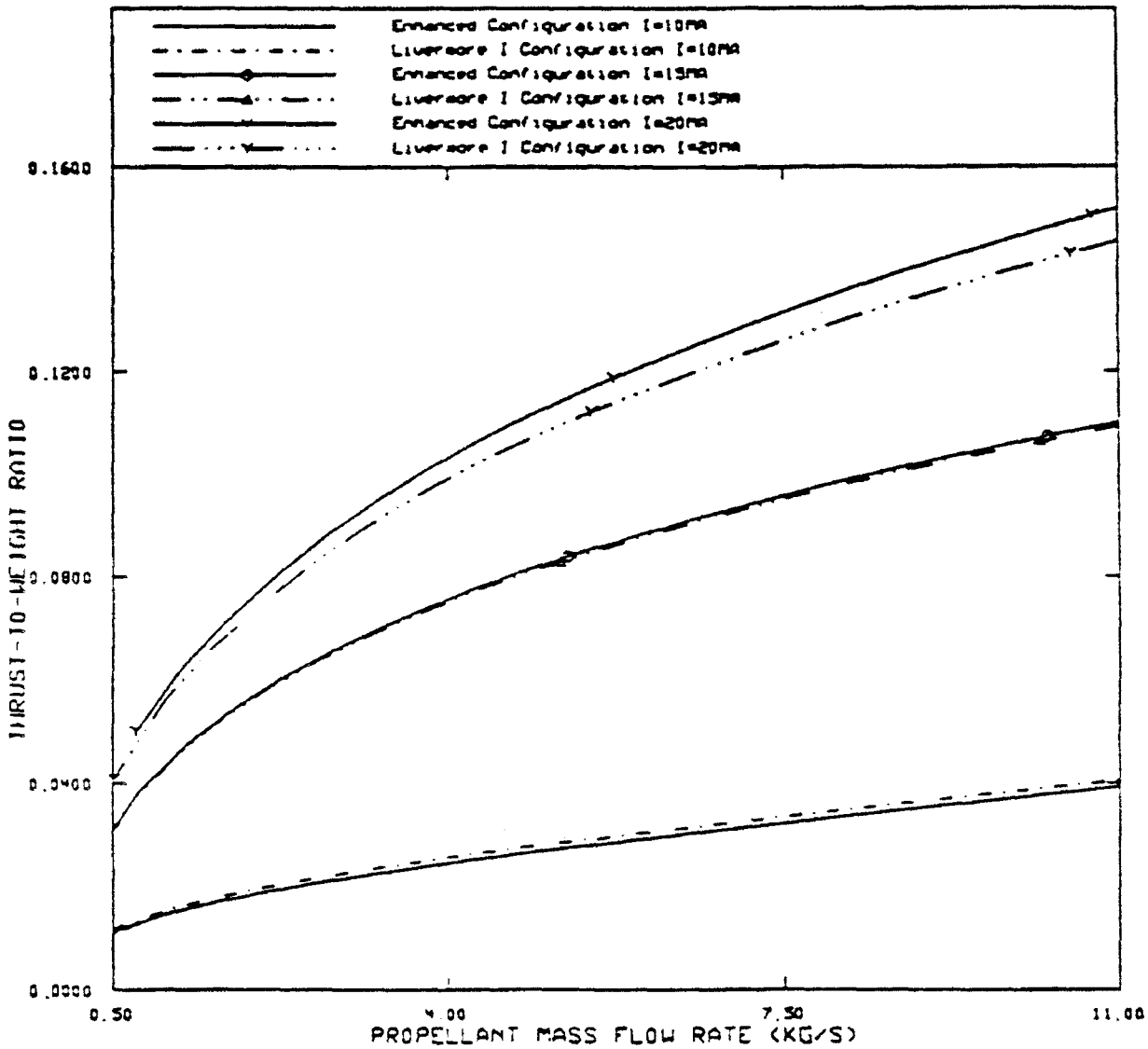

Figure A.3
Thrust-to-Weight Ratios for Enhanced and
Livermore-I Electrodes (Δv=5km/s) (Same as Figure 27)

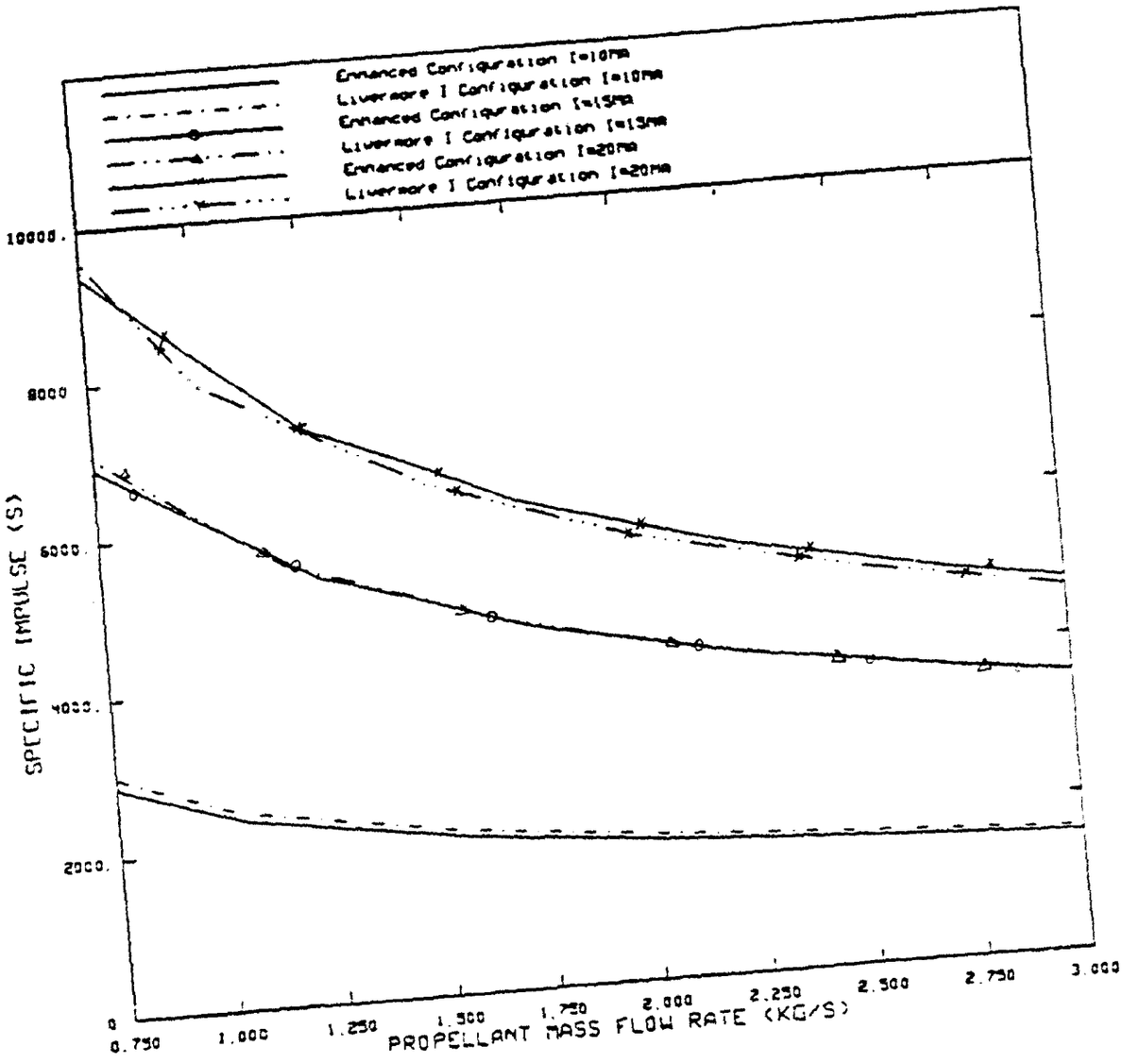

Figure A.4
Specific Impulse for Enhanced and
Livermore-I Electrodes (Δv=5km/s) (Same as Figure 26)

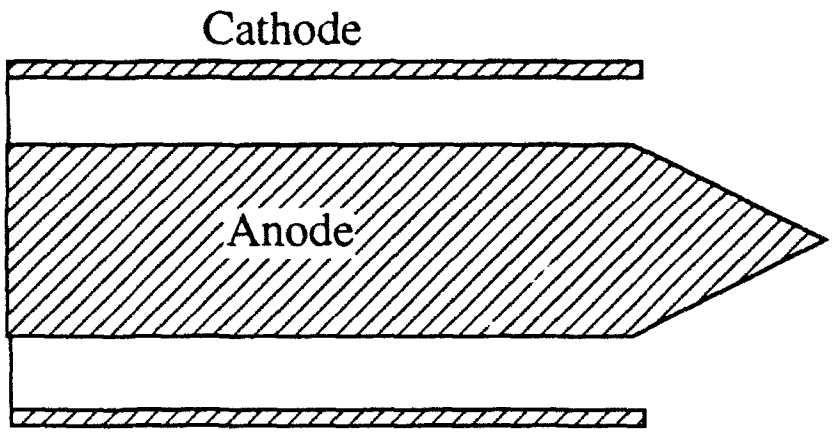

Anode with Equilateral Tip

Figure A.5
Equilateral Anode Tip

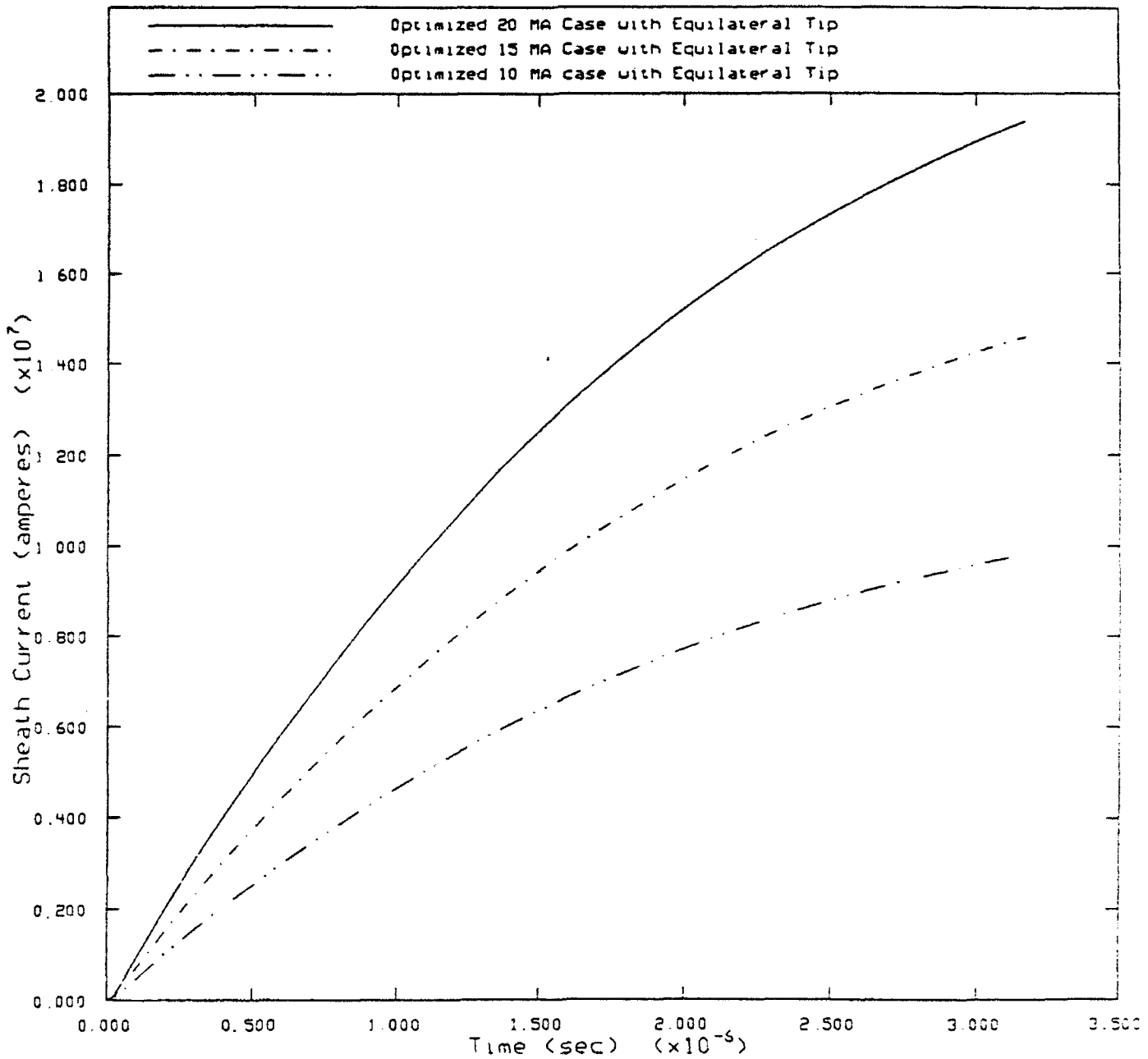

Figure A.6
Optimized Current Histories for Equilateral Anode Tip

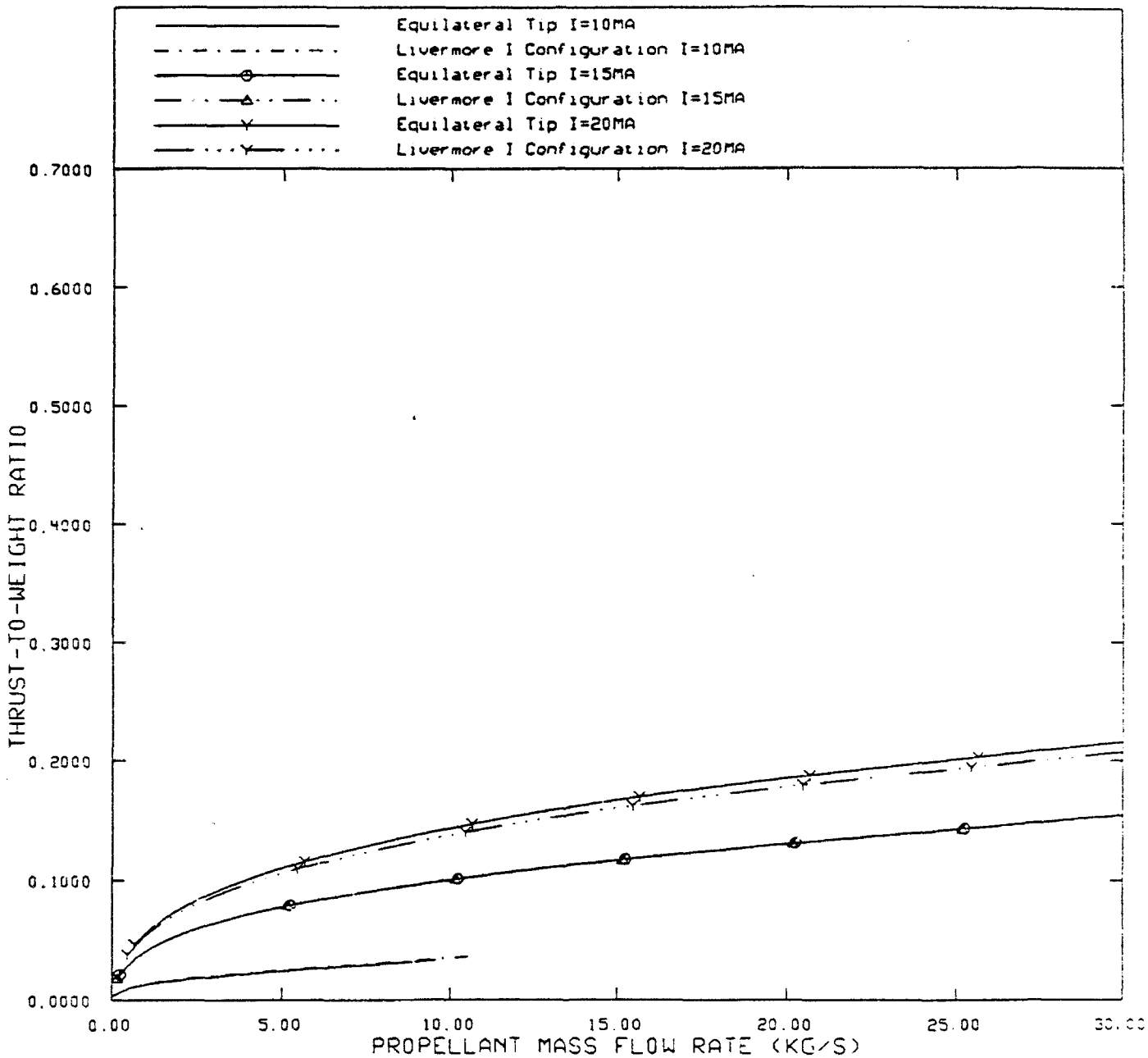

Figure A.7
Thrust-to-Weight Ratios for Equilateral Anode Tip
and Livermore-I Electrode (Δv=5km/s)

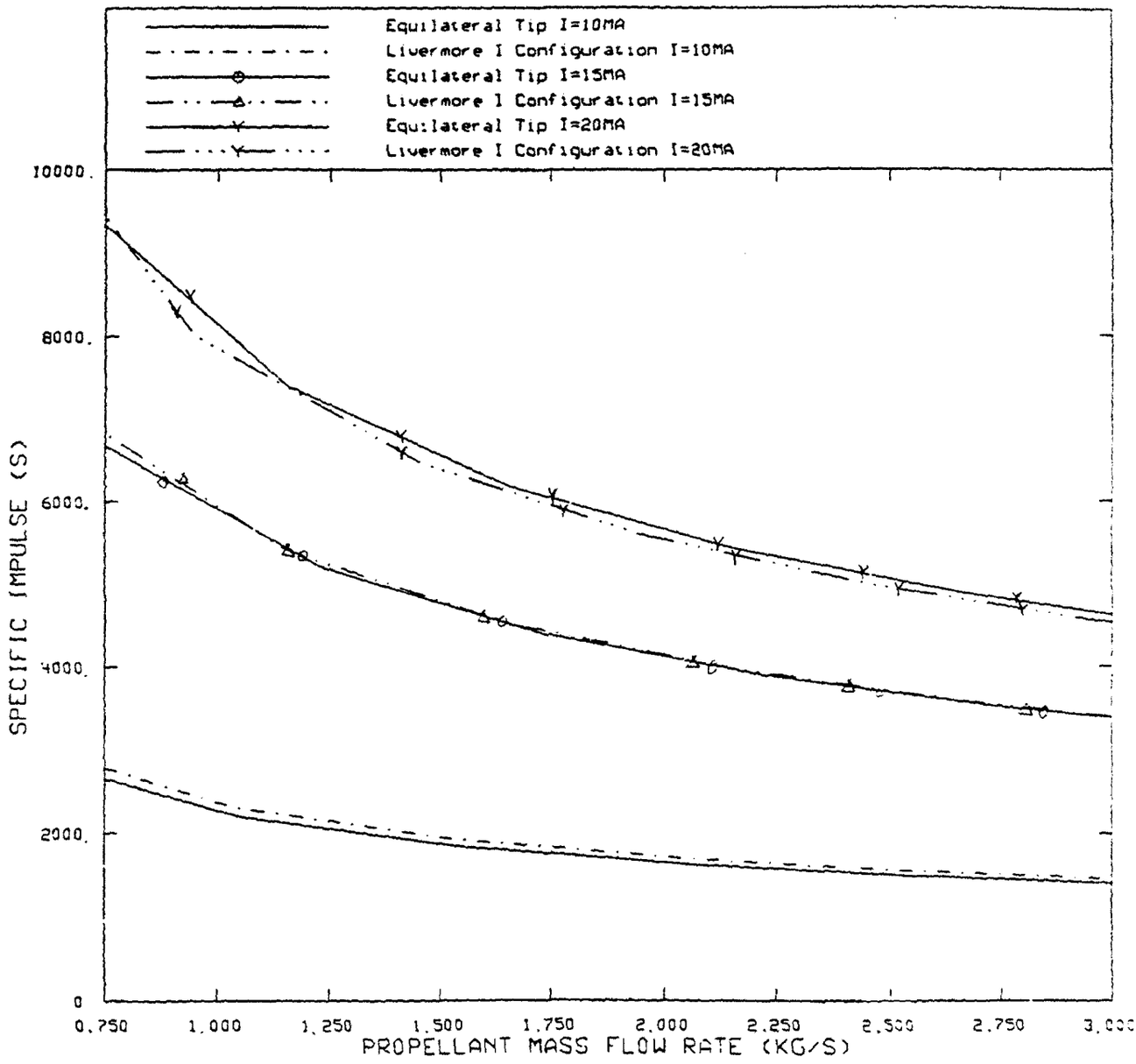

Figure A.8
Specific Impulse for Equilateral Anode Tip
and Livermore-I Electrode (Δv=5km/s)

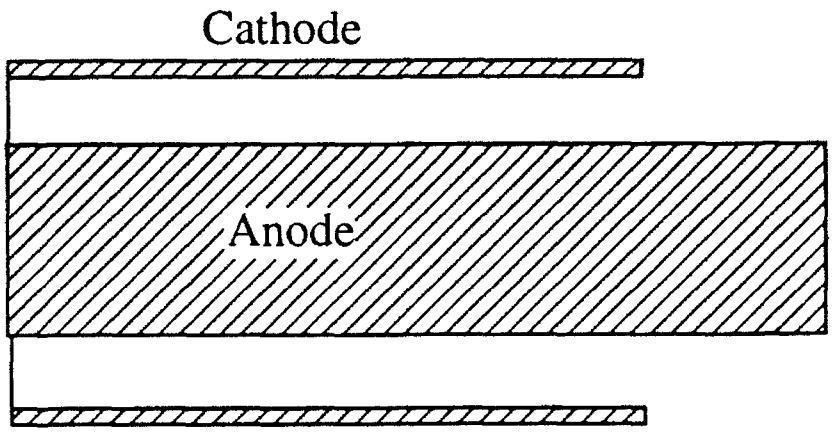

Anode with Cylindrical Tip

Figure A.9
Cylindrical Anode Tip

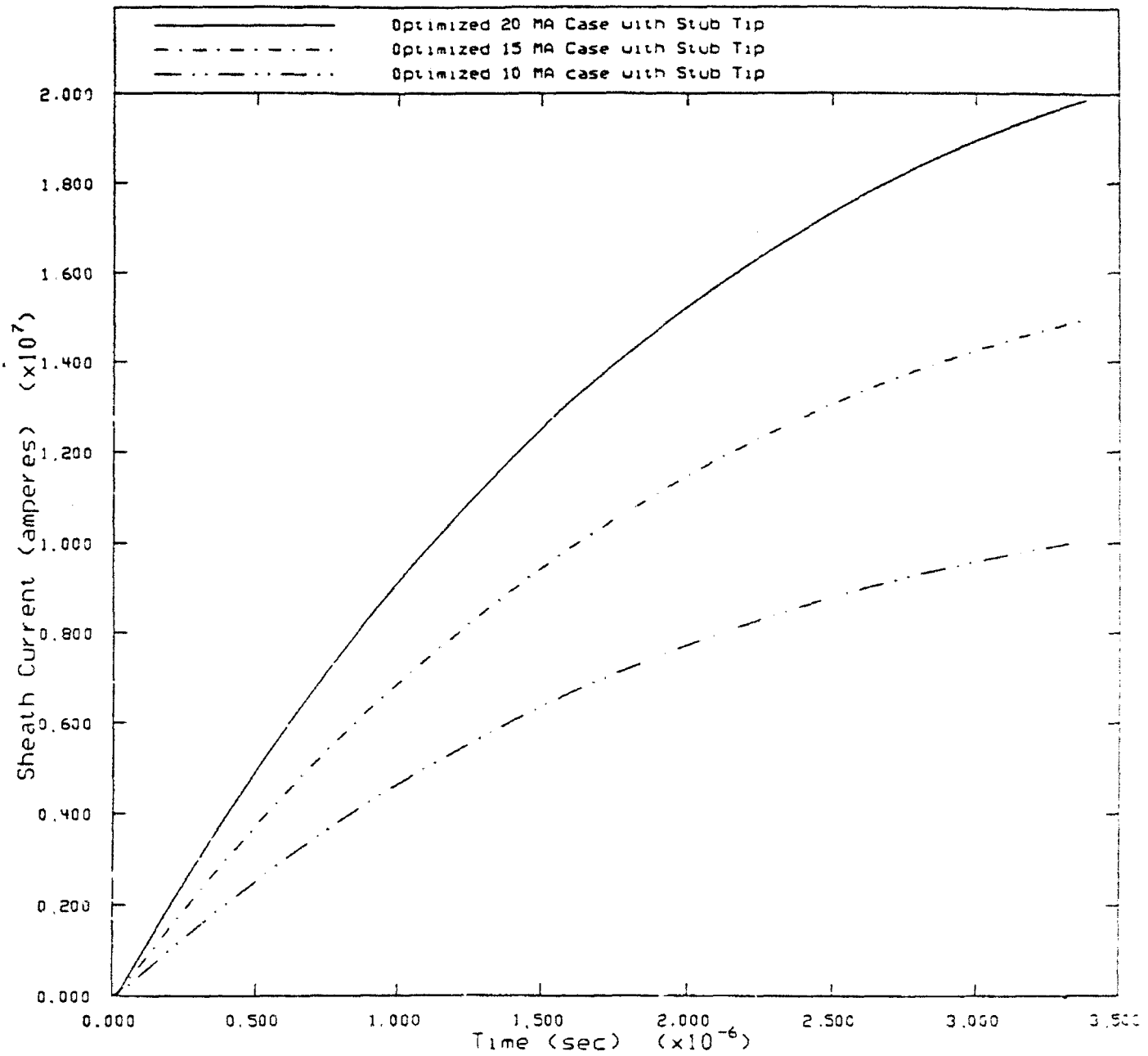

Figure A.10
Optimized Current Histories for Cylindrical Anode Tip

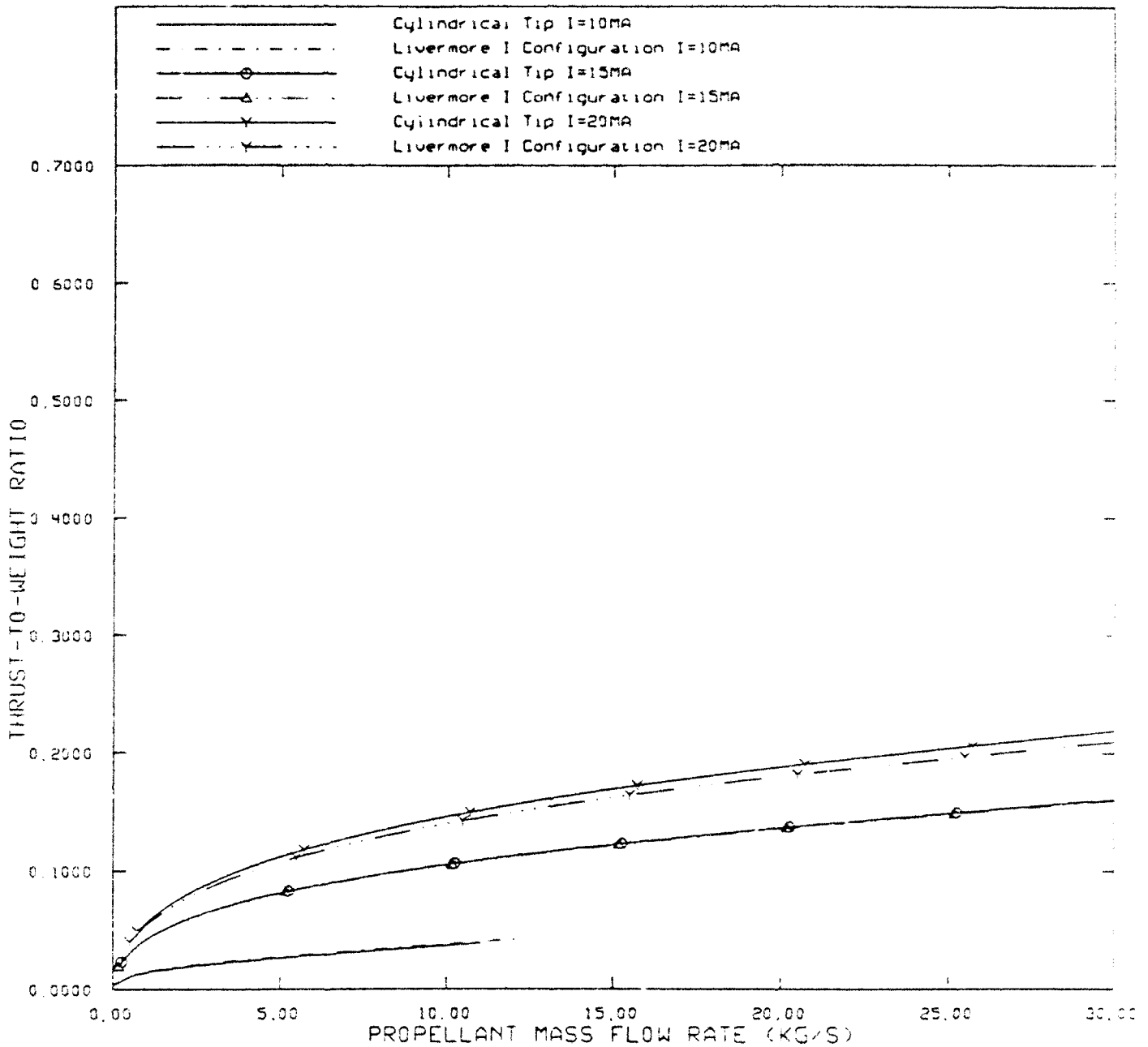

Figure A.11
Thrust-to-Weight Ratios for Cylindrical Anode Tip
and Livermore-I Electrode (Δv=5km/s)

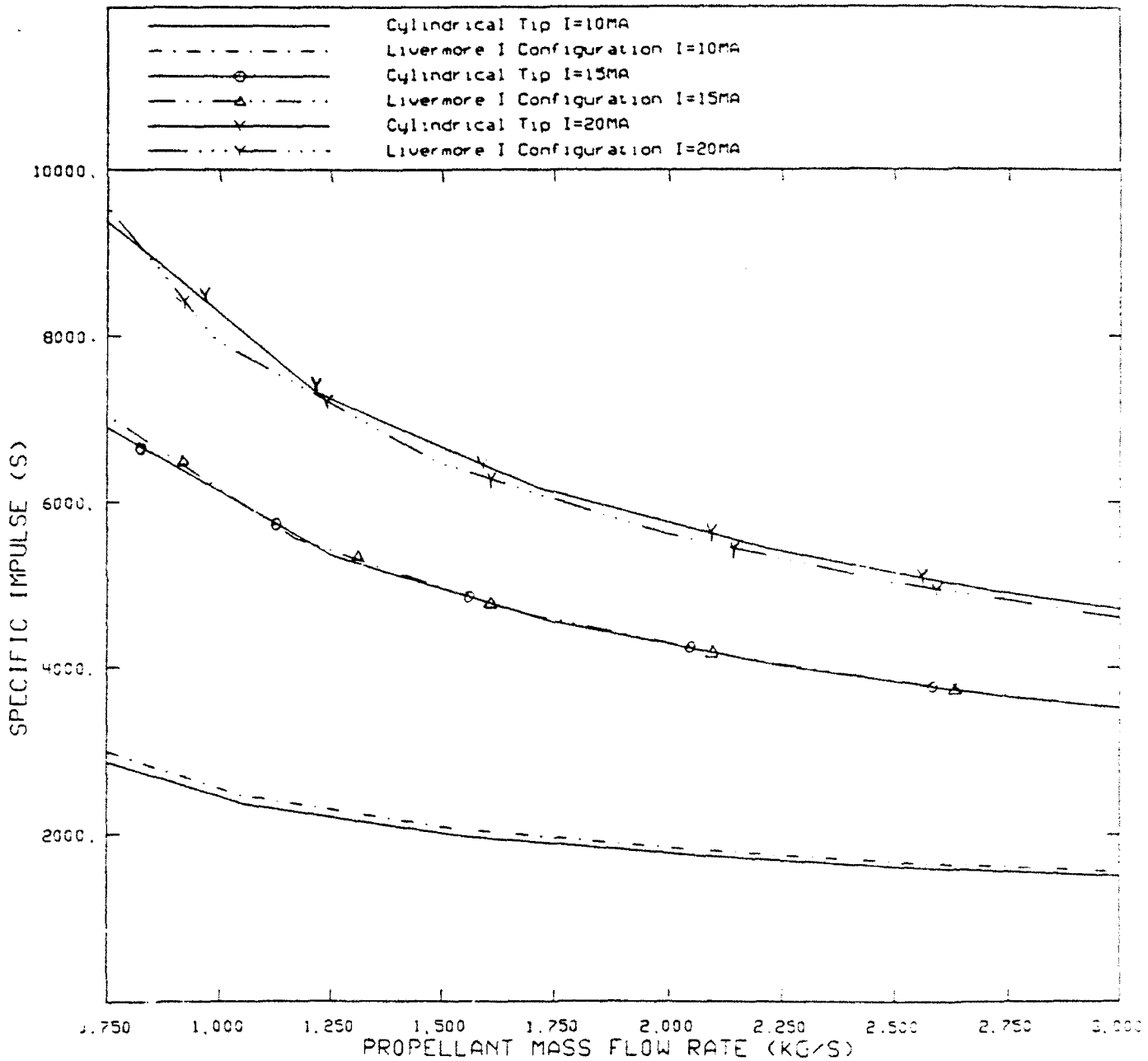

Figure A.12
Specific Impulse for Cylindrical Anode Tip
and Livermore-I Electrode (Δv=5km/s)

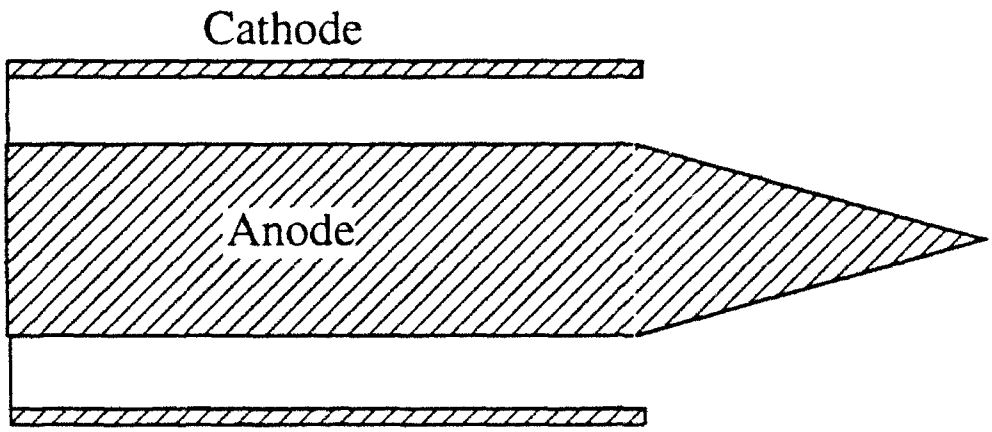

Anode with Extended Triangular Tip

Figure A.13
Extended Triangular Anode Tip

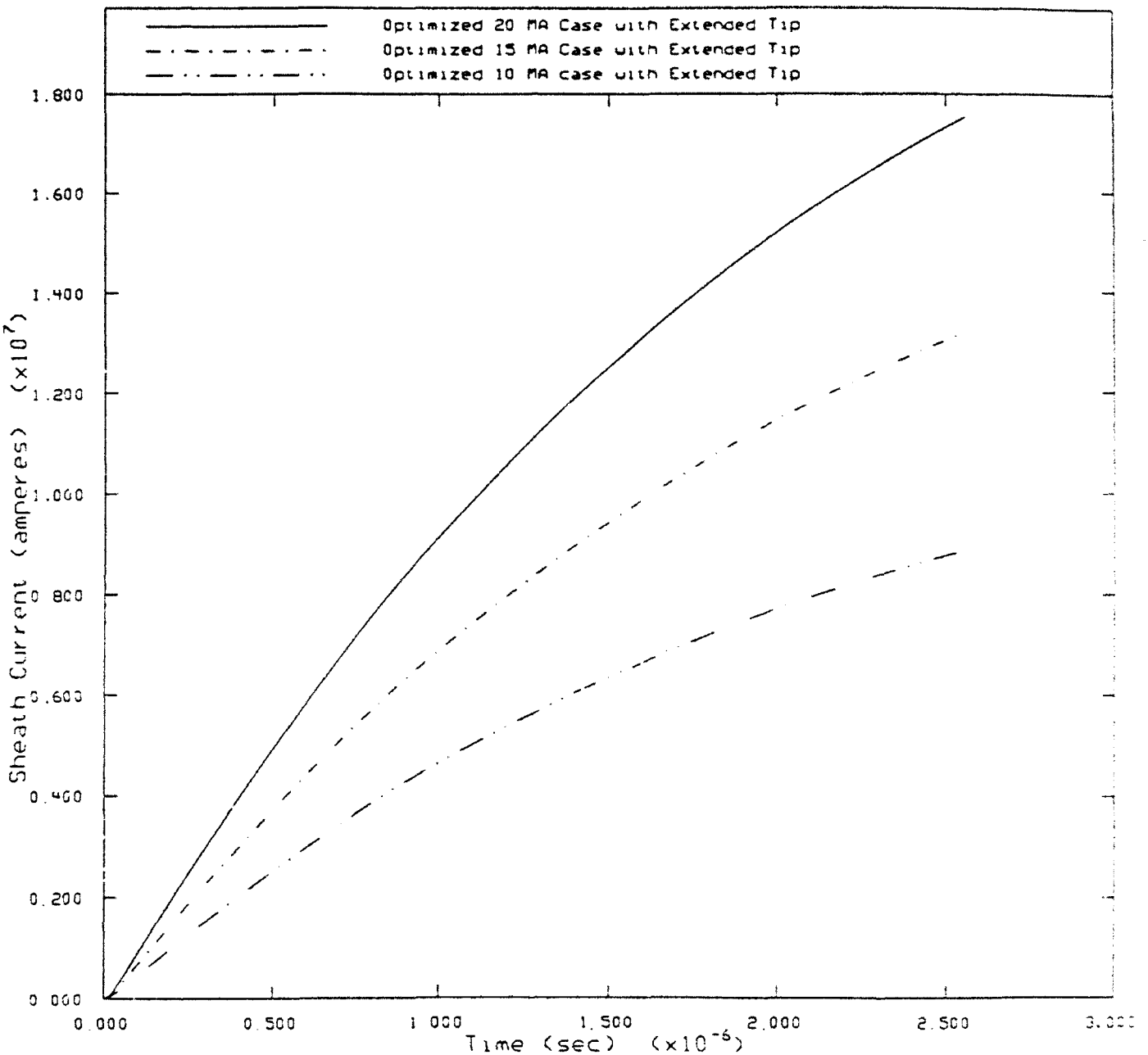

Figure A.14
Optimized Current Histories for Extended Triangular Tip Anode

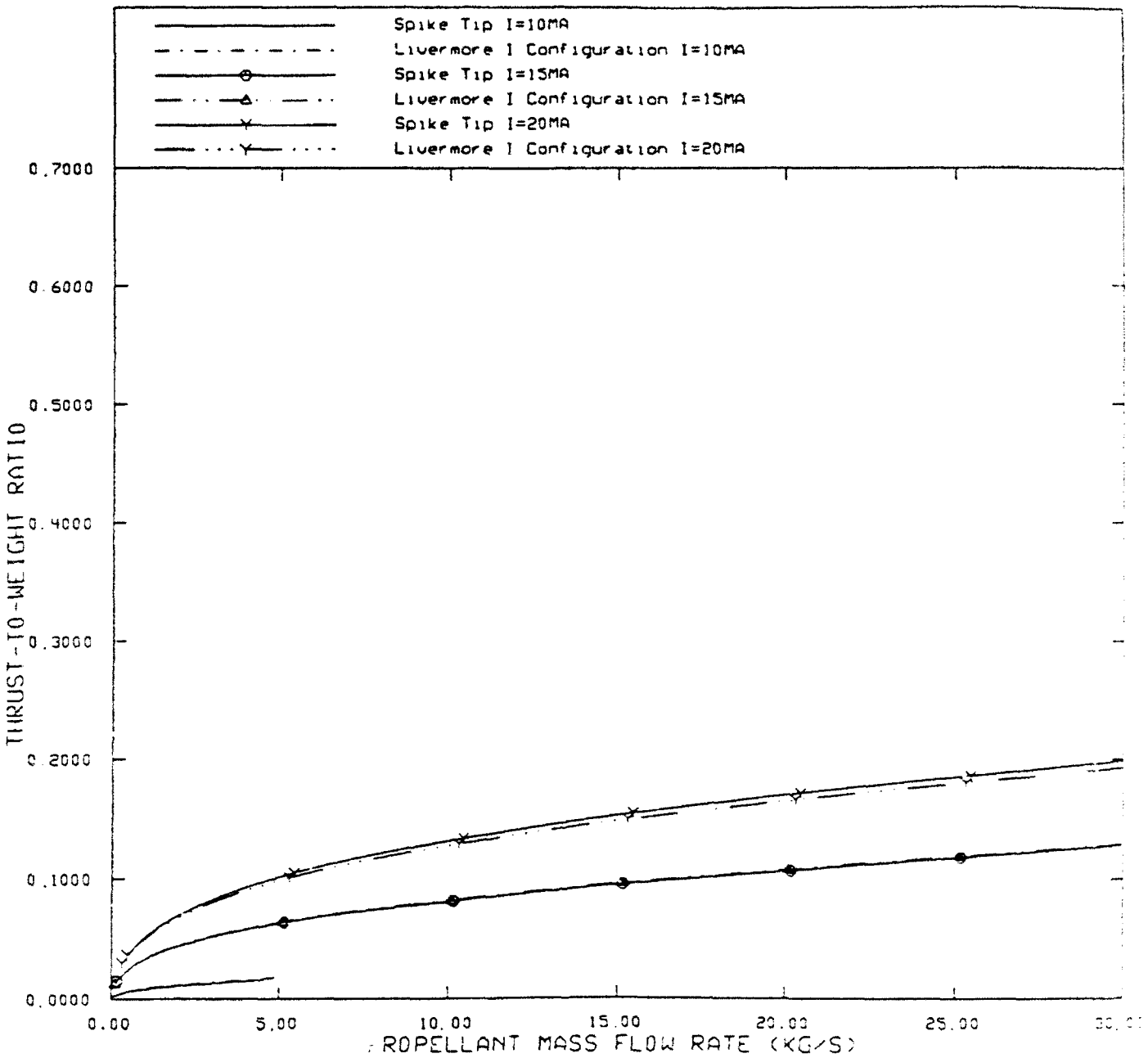

Figure A.15
Thrust-to-Weight Ratios for Extended Triangular Anode
and Livermore-I Electrode (Δv=5km/s)

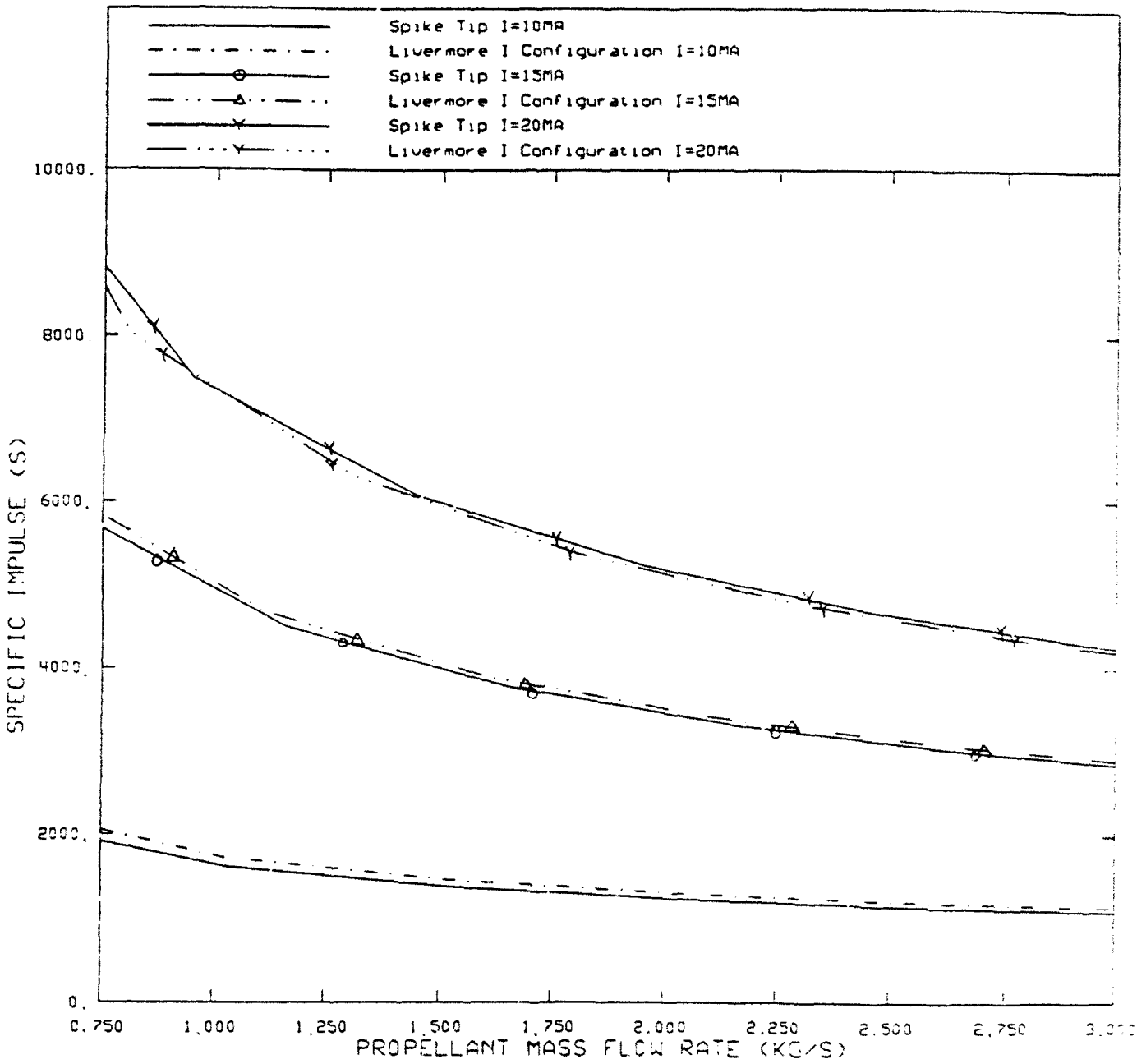

Figure A.16
Specific Impulse for Extended Triangular Anode Tip
and Livermore-I Electrode (Δv=5km/s)

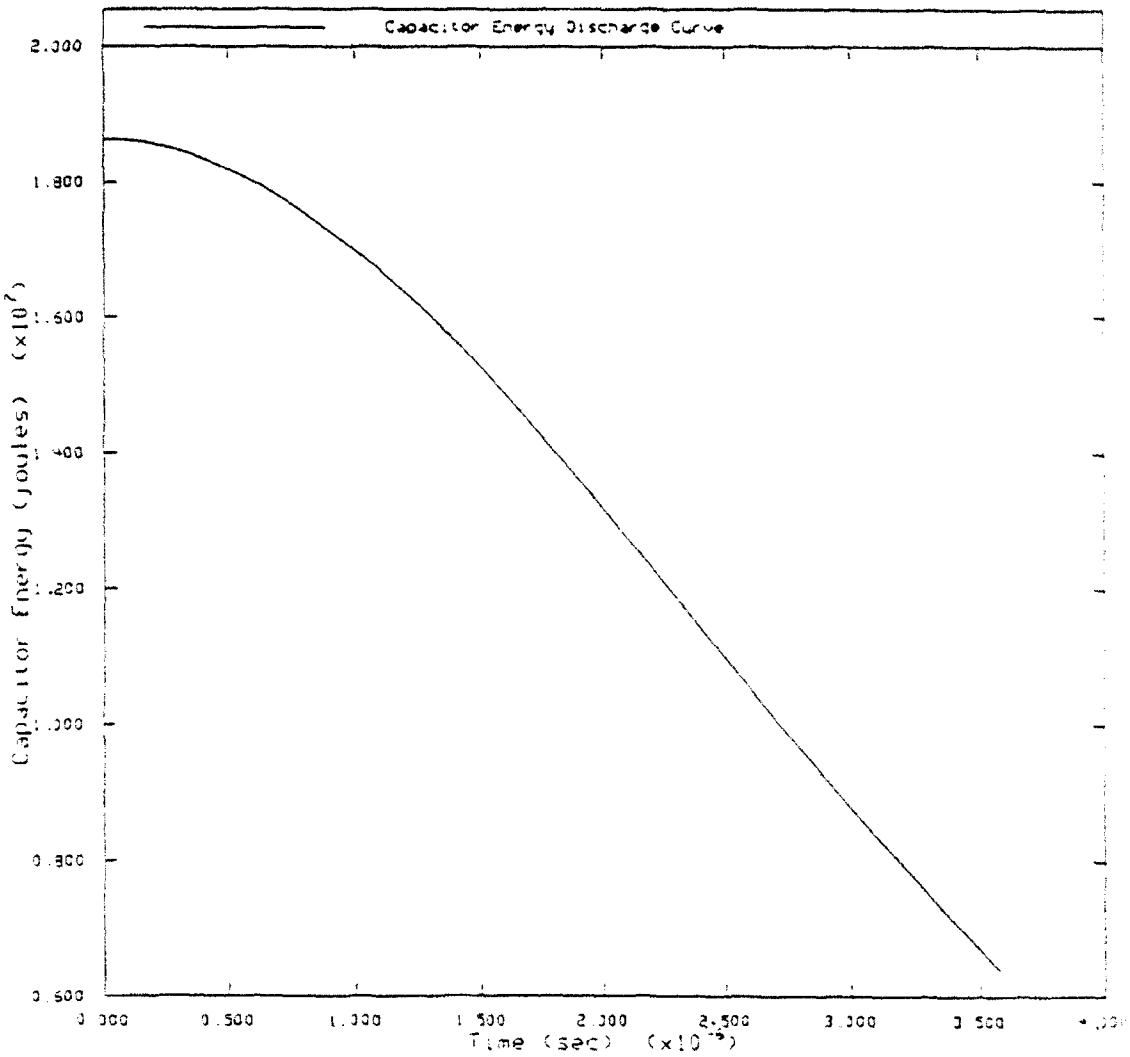

Figure A.17
Capacitor Energy Discharge Curve

APPENDIX B

A listing of the program used to calculate the current history and sheath parameters for the rundown phase of plasma focus operation is included in the following pages. The code TRAN.f is written in FORTRAN 77 and utilizes a transient circuit solver to calculate the voltage and current histories for the equivalent circuit. The plasma circuit parameters are calculated using suitable physical models in the subroutine SOLVE. While the rundown velocity is calculated using the snowplow model.

Operating Instructions for Using the Transient Code TRAN.f

1. Compile TRAN.f using command "f77 TRAN.f"
2. Change input parameters in input deck TRAN.in
3. Execute program by simply typing "a.out", program will automatically read input data and output data into files:
   - i) IEX.OUT - This file contains the external circuit current.
   - ii) IPLAS.OUT - This file contains the plasma sheath current.
   - iii) IND.OUT - This file contains the plasma sheath inductance history.
   - iv) VOLT.OUT - This file contains the node voltage over the plasma sheath.
   - v) VRUN.OUT - This file contains the rundown velocity for the plasma sheath.

```
c*************************************************************************
c*      Program TRAN.F
c*      Programmer: Glen T. Nakafuji
c*      Purpose:
c*      1. Calculate current and voltage responses for equivalent circuit representation of
c*         the dense plasma focus device.
c*      2. Calculate dynamic circuit parameter values for plasma sheath during the rundown
c*         phase of operation.
c*      3. Calculates rundown velocity of propagating plasma sheath
c*      Models:
c*      1. Companion circuit model used to represent reactive elements in equivalent circuit
c*      2. Snowplow model used to calculate rundown velocity of a totally absorbing arc
c*         sheet as it propagates down the annular region.
c*      3. Dynamic models for sheath inductance, sheath resistance
c*************************************************************************

      program TRAN

      dimension RI(20),Iin(20),LI(20),Vin(20)
      dimension Y(20,20),I(20),V(20),Rad(4),ZA(2)
      double precision RI,Iin,LI,Vin,Y,I,ZA
      double precision V,h,c,time,z,Rad,dz,tau
      double precision pi,rhoi,mu,imass
      PARAMETER (pi=3.14159265,mu=1.256637E-6,vmax=3.5E5)
      COMMON / /rhoi,imass
      integer flag,D,iter

c***** Closes old output file
      open (unit = 30,file = 'scurr.out',status = 'unknown')
      close (30,status = 'delete')
      open (unit = 40,file = 'lcurr.out',status = 'unknown')
      close (40,status = 'delete')
      open (unit = 50,file = 'volt.out',status = 'unknown')
      close (50,status = 'delete')
      open (unit = 70,file = 'vrun.out',status = 'unknown')
      close (70,status = 'delete')
      open (unit = 90,file = 'ind.out',status = 'unknown')
      close (90,status = 'delete')
      open (unit = 100,file = 'N.out',status = 'unknown')
      close (100,status = 'delete')
      open (unit = 200,file = 'convert.out',status = 'unknown')
      close (200,status = 'delete')
c***** Open TEMPORARY input file
      open (unit = 20,file = 'v4.in',status = 'old')
c***** Open TEMPORARY output file
      open (unit = 30,file = 'scurr.out',status = 'new')
      open (unit = 40,file = 'lcurr.out',status = 'new')
      open (unit = 50,file = 'volt.out',status = 'new')
      open (unit = 70,file = 'vrun.out',status = 'new')
      open (unit = 90,file = 'ind.out',status = 'new')
      open (unit = 100,file = 'N.out',status = 'new')
```

```
      open (unit = 200,file = 'convert.out',status = 'new')
c***** Set flag=3 for Imax check prior to main problem
      flag=3
c***** Set iteration counter to zero
      iter = 0
c***** Set time constant tau
      tau = 0.0
c***** Read input data from deck
      call INPUT(RI,Iin,LI,Vin,h,c,Rad,dz,ZA)


c***** Initialize time and displacement
      call INIT1(time,z,I,Y,V,dz)
      write (6,900) time,z,flag
10    flag = 3

c***** Initialize conductance matrices  Y1 and Y2 and I
      call INIT2(RI,h,c,Vin,Iin,LI,Y,I,flag,D)
c***** Solve I = YV system
      call LU(D,Y,I,V,time,h)
c*******Write data
      write(30,1000) time,V(7)
      write(40,1000) time,(V(1)*RI(3))
      write(50,1000) time,V(1)
      write(90,1000) time,LI(3)
c****** INPUT check mode only
c     call CHECK(V,flag,time,tau)
c**********************************
      call SOLVE(I,V,time,RI,LI,h,z,ZA,Rad,flag,Iin,Vin,dz)
c***** Update screen every n iterations
c     write (6,1000) time,z
c***** Advance iteration counter by 1
      iter = iter + 1
c***** Check if endtime reached
      if (z.GE.ZA(1)) then
      call VOL(ZA,Rad,V,iter)
      write(6,*) iter
      stop
      endif
c***** Clear Arrays before next pass
      call ZERO(I,V,Y,D)
      goto 10

800   format('dimension =',I2)
900   format('time =',E13.7E2,'position =',E13.7E2,3x,I4)
1000  format(E13.7E2,3x,E13.7E2)
      stop
      end


c*****************************************************************
c     subroutine INPUT
```

```
c       Purpose: Initializes parameter arrays with initial values
c*****************************************************************
        subroutine INPUT(RI,Iin,LI,Vin,h,c,Rad,dz,ZA)
        dimension RI(20),Iin(20),LI(20),Rad(4)
        dimension Vin(20),ZA(2)
        double precision h,c,ZA,RI,Iin,LI,Rad,dz
        double precision r1,r2,r3,Vin,pi,mu,vmax,rhoi,imass,area
        PARAMETER (pi=3.14159265,mu=1.256637E-6,vmax=3.5E5)
        COMMON / /rhoi,imass
        real div

c****   reads parameters from input deck
c****   read in 1/ro (initial conductance)
        read (20,*)
        read (20,*) r1
        RI(1) = 1./r1
c****   read in 1/rcr (initial crowbar conductance)
        read (20,*)
        read (20,*) r2
        RI(2) = 1./r2
c****   read in 1/rl (leakage conductance)
        read (20,*)
        read (20,*) r3
        RI(3) = 1./r3
c****   read in Lo (initial circuit inductance)
        read (20,*)
        read (20,*) LI(1)
c****   read in Lc (crowbar inductance)
        read (20,*)
        read (20,*) LI(2)
c****   read in initial capacitor voltage
        read (20,*)
        read (20,*) Vin(3)
c****   read in cathode radius
        read (20,*)
        read (20,*) Rad(1)
c****   read in anode radius
        read (20,*)
        read (20,*) Rad(2)
c****   read in boss radius
        read (20,*)
        read (20,*) Rad(3)
c****   read in time step
        read (20,*)
        read (20,*) h
c****   read in capacitance value
        read (20,*)
        read (20,*) c
c****   read in anode length
        read (20,*)
        read (20,*) ZA(1)
c****   read in curve in length
```

```
      read (20,*)
      read (20,*) ZA(2)
c****  read in sheath thickness
      read (20,*)
      read (20,*) dz
c****  read in coefficient for limiting leakage current
      read (20,*)
      read (20,*) RI(20)
c***  read in initial fill gas density
      read(20,*)
      read(20,*) rhoi
c****  calculate initial sheath inductance
      div = Rad(1)/Rad(2)
      LI(3) = (2.E-7)*ALOG(div)*(dz + 1.*.14)
c****  set for now initial plasma resistance
      RI(4) = 1./1.E-14
      area= pi*((Rad(1)**2) - (Rad(2)**2))
      imass = rhoi*dz*area

      return
      end

c*******************************************************************
c*     Subroutine INIT1
c*     Purpose: initialize time, displacement and arrays
c*******************************************************************
      subroutine INIT1(time,z,I,Y,V,dz)
      dimension I(20),Y(20,20),V(20)
      double precision I,Y,V,time,z,dz
      integer j,k

c*****  Initialize displacement to 1st thickness of sheath
      z = dz
c*****  Zero out arrays and variables
      time = 0.0
      do 10 j = 1,20
        I(j) = 0.0
        V(j) = 0.0
       do 5 k = 1,20
        Y(j,k) = 0.0
5      continue
10    continue

      return
      end

c*******************************************************************
c*     Subroutine INIT2
c*     Purpose: Initialize conductance matrices and select which
c*     circuit to implement based on the flags that are set.
c*
c*******************************************************************
```

```
      subroutine INIT2(RI,h,c,Vin,Iin,LI,Y,I,flag,D)
        dimension RI(20),Vin(20),Iin(20),LI(20)
        dimension Y(20,20),I(20),Y1(20,20),Y2(20,20)

        double precision RI,Vin,Iin,LI,Y,I,h,c
        integer flag,D,j,k

        if (flag.NE.2) then
c****** Initialize elements of 7x7 matrix for circuit w/o crowbar
        Y1(1,1) = RI(1) + RI(3)
        Y1(1,2) = -RI(1)
        Y1(1,7) = 1.
        Y1(2,1) = -RI(1)
        Y1(2,2) = RI(1)
        Y1(2,6) = -1.
        Y1(3,5) = 1.
        Y1(3,6) = 1.
        Y1(4,4) = RI(4)
        Y1(4,7) = -1.
        Y1(5,3) = (2*c)/h
        Y1(5,5) = -1.
        Y1(6,2) = -h/(2*LI(1))
        Y1(6,3) = h/(2*LI(1))
        Y1(6,6) = -1.
        Y1(7,1) = h/(2*LI(3))
        Y1(7,4) = -h/(2*LI(3))
        Y1(7,7) = -1.
c***** Initialize and update solution vector I
        I(5) = Iin(1) + ((2*c)/h)*Vin(3)
        c1 = -h/(2*LI(1))
        I(6) = c1*(Vin(3) - Vin(2)) - Iin(2)
        c2 = -h/(2*LI(3))
        I(7) = c2*(Vin(1) - Vin(4)) - Iin(4)
        D = 7
c***** Write Y1 into general Y conductance matrix
        do 200 j = 1,D
          do 200 k = 1,D
          Y(j,k) = Y1(j,k)
200     continue

        endif

        if (flag.EQ.2) then
c***** Initialize Y2 matrix if flag = 2
        Y2(1,1) = RI(1) + RI(3)
        Y2(1,2) = -RI(1)
        Y2(1,8) = 1.
        Y2(1,9) = 1.
        Y2(2,1) = -RI(1)
        Y2(2,2) = RI(1)
```

```
      Y2(2,7) = -1.
      Y2(7,6) = 1.
      Y2(7,7) = 1.
      Y2(4,4) = RI(4)
      Y2(4,9) = -1.
      Y2(5,5) = RI(2)
      Y2(5,8) = -1.
      Y2(6,3) = (2*c)/h
      Y2(6,6) = -1.
      Y2(3,2) = -h/(2*LI(1))
      Y2(3,3) = h/(2*LI(1))
      Y2(3,7) = -1.
      Y2(8,1) = h/(2*LI(2))
      Y2(8,5) = -h/(2*LI(2))
      Y2(8,8) = -1.
      Y2(9,1) = h/(2*LI(3))
      Y2(9,4) = -h/(2*LI(3))
      Y2(9,9) = -1.
c***** Initialize I vector for Y2 system
      I(6) = Iin(1) + ((2*c)/h)*Vin(3)
      c1 = -h/(2*LI(1))
      I(3) = c1*(Vin(3) - Vin(2)) - Iin(2)
      c3 = -h/(2*LI(2))
      I(8) = c3*(Vin(1) - Vin(5)) - Iin(3)
      c2 = -h/(2*LI(3))
      I(9) = c2*(Vin(1) - Vin(4)) - Iin(4)
      D = 9
c***** Write Y2 into general Y conductance matrix
      do 300 j = 1,D
        do 300 k = 1,D
        Y(j,k) = Y2(j,k)
300   continue

      endif


      return
      end

c*****************************************************************
c*    Subroutine LU
c*    Purpose: Solves I=YV system using LU decomposition and also
c*    advances time step
c*****************************************************************


      subroutine LU(row,A,B,X,time,h)
     dimension L(20,20),U(20,20),B(20),A(20,20)
    dimension BP(20),X(20)
     double precision L,U,B,A,BP,X,time,h
    integer row,col
    col=row+1
```

```
      return
      end
c***********************************************************************
c*      Subroutine forward
c*      Purpose: Part of subroutine LU to solve system
c***********************************************************************

      subroutine forward(row,L,BP,B)
      dimension L(20,20),BP(20),B(20)
      double precision L,BP,B
      integer i,j,row

      BP(1)=B(1)/L(1,1)
      do 200 i=2,row
        temp=0.0
        do 100 j=1,i-1
          temp=temp+L(i,j)*BP(j)
100       continue
        BP(i)=(B(i)-temp)/L(i,i)
200     continue

      return
      end
c***********************************************************************
c*      Subroutine back
c*      Purpose: Part of subroutine LU to solve system
c***********************************************************************
      subroutine back(row,U,X,BP)
      dimension U(20,20),X(20),BP(20)
      double precision U,X,BP,sum
      integer i,j,row

      X(row)=BP(row)/U(row,row)
      do 200 i = row-1,1,-1
       sum=0.0
        do 180 j=i+1,row
         sum = sum+U(i,j)*X(j)
180       continue
      X(i)=(BP(i)-sum)/U(i,i)
200     continue

      return
      end
c***********************************************************************
c*      Subroutine pivot
c*      Purpose: Part of subroutine LU to solve system
c***********************************************************************
      subroutine pivot(row,A,B)
      dimension A(20,20),B(20)
      double precision A,B,check,sub,sub1,temp
      integer row
```

```
1     temp=0.0
     sub=0.0
     sub1=0.0

        check = A(row,row)
         if (check.EQ.0) then
                do 5 i = 1,row
                sub = A(1,i)
                A(1,i) = A(row,i)
                A(row,i) = sub
5               continue
         sub1 = B(1)
         B(1) = B(row)
         B(row) = sub1
         endif

        do 20 i = 1,row-1
         check = A(i,i)
                if (check.EQ.0) then
                  do 10 j = 1,row
                  sub = A(i+1,j)
                  A(i+1,j) = A(i,j)
                  A(i,j) = sub
10                continue
                sub1 = B(i)
                B(i) = B(i+1)
                B(i+1) = sub1
                endif
20      continue

c*****        check diagonal elements for zeros
              do 30 i = 1,row
                  temp = A(i,i)
c*****        if zero go back to beginning and swap rows
                if (temp.EQ.0) then
                   goto 1
                   endif
30              continue

         return
           end

c*****************************************************************
c*      Subroutine ZERO
c*      Purpose: Zero out general matrix and vectors before next
c*      iteration
c*****************************************************************
        subroutine ZERO(I,V,Y,D)
        dimension V(20),I(20),Y(20,20)
        double precision V,I,Y
        integer D
```

```
      do 20 j=1,D
       do 10 k=1,D
       Y(j,k) = 0.0
10     continue
      I(j)=0.0
      V(j)=0.0
20    continue

      return
      end

c*****************************************************************
c*    Subroutine CHECK
c*    Purpose: Checks if current of initial circuit (7x7) is
c*    at Imax, if it is, switch in 9x9 by setting flag to 2
c*    otherwise keep flag at 1 or 3
c*****************************************************************
      subroutine CHECK(V,flag,time,tau)
      dimension V(20)
      double precision V,time,tau,temp,max,tmax
      integer flag

c****** If flag=3 program in Imax check mode
      if (flag.EQ.3) then
c****** If current value of Ipf is greater than previous max, store
              temp = ABS(V(7))
               if (temp.GT.max) then
               max = temp
               tmax = time
               endif
c***** Otherwise, check for end of discharge, if at end set flag to 1
                      if (time.GE.tau) then
                      flag = 1
                      time = 0.0
                      write (6,1000) max,tmax
                      endif
      endif

c*****If flag=1 program starts problem with 7x7 system
      if (flag.EQ.1) then
c*****Check if time > tmax, if it is then switch circuit by flag = 2
              if (time.GT.tmax) then
              flag = 2
              endif
      endif

1000  format('max current of',f13.7,'occurs at t = ',f15.8)
      return
      end
c*****************************************************************
c*    Subroutine SOLVE
c*    Purpose: Solve for sheath parameters and calculate current
```

```
c*      displacement, and replace new values into init vectors
c*****************************************************************

        subroutine SOLVE(I,V,time,RI,LI,h,z,ZA,Rad,flag,Iin,Vin,dz)
        dimension I(20),V(20),RI(20),LI(20),Rad(4)
        dimension Iin(20),Vin(20),ZA(2)
        double precision I,V,RI,LI,Rad,time,h,z
        double precision vrun,Iin,Vin,denom,pi,mu,vmax
        double precision imass,rhoi,area,Inew
        double precision Rlo,dz
        double precision Ilift,ZA,r,vcorr,delta
        double precision intold, intsum, intnew
        PARAMETER (pi=3.14159265,mu=1.256637E-6,vmax=3.5E5)
        COMMON / /rhoi,imass
        integer flag

c****   Set initial leakage conductance
        Rlo = RI(3)
c****   Replace old currents and voltages with new values
        do 10 j=1,4
         Vin(j) = V(j)
10      continue
         Iin(1) = V(5)
         Iin(2) = V(6)
         Iin(4) = V(7)
        Inew = V(7)

c********Don't need 9x9
c       if (flag.EQ.2) then
c       do 20 j=1,5
c        Vin(j) = V(j)
c20     continue
c        Iin(1) = V(6)
c        Iin(2) = V(7)
c        Iin(3) = V(8)
c        Iin(4) = V(9)
c       Inew = V(9)
c       endif


c*******Calculate rundown velocity
c*****************************************************************
c*****  with Liftoff current calculation
        vrun = 0.0
c****   Adjusted current for liftoff
        Ilift = (Inew**2) - (4144.82852**2)

c*****  Call radius and velocity correction routine
        call CORRECT(Rad,ZA,r,vcorr,z)

c*****************************************************************
```

```
c****** Snowplow model using trapezoidal approximation
c********Calculate LI**2 integral using Trapezoidal approx.
      if (Ilift.GT.0.0) then
        intnew = (LI(3)*(Ilift))/z
        delta = .5*h*(intold + intnew)
        intsum = intsum + delta
        intold = intnew
        area = pi*(Rad(1)**2 - r**2)
        denom = 2*(imass+(rhoi*area*z))
        vrun = (vcorr/denom)*intsum
      endif
c*****************************************************************
c*****************************************************************
c****** Limit sheath velocity to implosion velocity
      if (vrun.GT.vmax) then
      vrun = vmax
      endif
c*******Calculate new position
      z = z + vrun*h
c***  Write rundown velocity to output
      write (70,1000) time,vrun
c****** Calculate new sheath inductance
      div = Rad(1)/r
      LI(3) = (2E-7)*ALOG(div)*(z + 1.*.14)
c*****************************************************************
1000  format(E13.7E2,4x,E13.7E2)
      return
      end

c*****************************************************************
c*    Subroutine CORRECT
c*    Purpose: Correct velocity and radius for sloped anode section
c*
c*****************************************************************
      subroutine CORRECT(Rad,ZA,r,vcorr,z)
      dimension Rad(4),ZA(2)
      double precision Rad,ZA,r,vcorr,z,rboss,ztip,zcheck
      double precision r1,r2,zrad,drdz,zcv,top,bottom,ra
      ztip = ZA(1)
      zcv = ZA(2)
      rboss = Rad(3)
      ra = Rad(2)
      zcheck = ztip - zcv
        if (zcheck.LT.0.0) then
        write(6,*) ('Electrode Geometry Invalid')
        stop
        endif
      zrad = zcv + ra - rboss
c****  If anode hasn't started curving in keep factors constant
      vcorr = 1.0
      r = ra
c****  If anode has started curving in, calculate velocity and
```

```
c****  radius adjustment
        if (z.GE.zcv) then
              if (z.GE.zrad) then
              r = rboss
              vcorr = 1.0
              goto 10
              endif
        top = -z + zcv
      bottom = SQRT(((ra - rboss)**2) - ((z - zcv)**2))
        drdz = top/bottom
c****   correction coefficient for axial velocity component
        vcorr = 1./SQRT(1+drdz**2)
        r1 = (ra - rboss)**2
        r2 = (z - zcv)**2
c***    correction for radial length component
        r = rboss + SQRT(r1 - r2)
        endif
10      continue
        return
        end
c*********************************************************************
**
c       subroutine VOL
c*      Purpose: Calculates volume of annular region in modified geometry and writes
c*               pertinent endtime values to output file "convert.out"
c*********************************************************************
**
        subroutine VOL(ZA,Rad,V,iter)
        dimension ZA(2),Rad(4),V(20)
        double precision ZA,Rad,area1,area2,volume,zins,pi,totlen
        double precision V,N
        integer iter
        PARAMETER (pi=3.14159265,mu=1.256637E-6,vmax=3.5E5)
        area1 = pi*(Rad(1)**2 - Rad(2)**2)
        area2 = pi*(Rad(1)**2 - Rad(3)**2)
c***** Insulator length
        zins = .14
c***** Total length of anode for Livermore I assumption
        totlen = .382
c***** Compute Volume of Annulus
        volume = area1*ZA(2)
        write (200,*) ('Volume is:')
        write (200,1000) volume
c***** Write final current of sheath
        write (200,*) ('Final current in sheath is:')
        write (200,1000) V(7)
c***** Write number of iterations
        write (200,*) ('Total number of iterations is:')
        write (200,2000) iter
1000    format (E13.8E2)
2000    format (I5)
        return
```